

# University of St Andrews

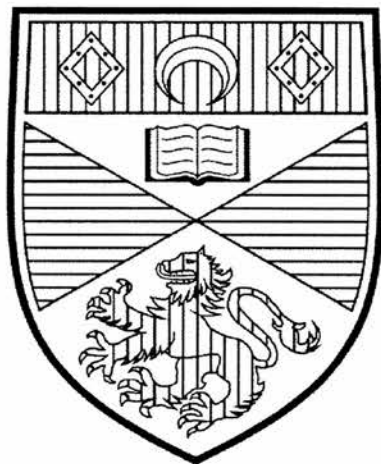


Full metadata for this thesis is available in  
St Andrews Research Repository  
at:

<http://research-repository.st-andrews.ac.uk/>

This thesis is protected by original copyright

**Re-crystallisation Studies of Amorphous  $\text{Ni}_{33}\text{Zr}_{67}$  &  
 $\text{Dy}_7\text{Fe}_3$  Alloys**



**A thesis submitted for the degree of  
Master of Philosophy**

**By**

**Talal Yousef**

**May 2000**



I, Talal Yousef, hereby certify that this thesis, which is approximately 18,000 words in length, has been written by me, that it is the record of work carried out by me and that it has not been submitted in any previous application for a higher degree.

Date 31.05.00 signature of candidate..

I was admitted as a research student in 10/98 and as a candidate for the degree of MPhil in.....; the higher study for which this is a record was carried out in the University of St. Andrews between 1998 and 2000.

Date.....signature of candidate.....

I hereby certify that the candidate has fulfilled the conditions of Resolution and Regulations appropriate for the degree of MPhil in the University of St. Andrews and that the candidate is qualified to submit this thesis in application for that degree.

Date.....signature of supervisor.....

I hereby certify that the candidate has fulfilled the conditions of Resolution and Regulations appropriate for the degree of MPhil in the University of St. Andrews and that the candidate is qualified to submit this thesis in application for that degree.

Date.....signature of supervisor.....

In submitting this thesis to the University of St. Andrews I understand that I am giving permission for it to be made available for use in accordance with the regulations of the University Library for the time being in force, subject to any copyright vested in the work not being affected thereby. I also understand that the title and abstract will be published, and that a copy of the work may be made and supplied to any bona fide library or research worker.

Date.....signature of candidate.....

## ABSTRACT

In this thesis crystallisation of amorphous  $\text{Ni}_{33}\text{Zr}_{67}$  and  $\text{Dy}_7\text{Fe}_3$  has been studied using, *in situ* kinetic neutron diffraction and Differential Scanning Calorimetry (DSC) techniques. DSC measurements were used primarily to get an initial estimation of crystallisation temperatures and the behaviour of phase formation or transformation.

For  $\alpha$ -  $\text{Ni}_{33}\text{Zr}_{67}$ , it was found that only one phase formed at  $\sim 392$  °C at heating rate 10 °C/min. The same behaviour was observed by neutron diffraction measurement at a heating rate of 1 °C/min and the phase formed at  $\sim 345$  °C, and it was found to be the well known tetragonal compound,  $\text{NiZr}_2$ , space group  $I4/mcm$  (#140) with the unit cell dimensions,  $a=6.5082(5)$  Å &  $c=5.2951(8)$  Å. The crystallisation was completely polymorphic.

For  $\alpha$ -  $\text{Dy}_7\text{Fe}_3$  from the DSC measurement, again at a heating rate of 10 °C/min, it was found that the sample goes through two phase formations at temperatures of  $\sim 280$  °C and  $\sim 386$  °C. There was a feeble indication of the possibility of unstable third intermediate phase existence at  $\sim 314$  °C. The neutron diffraction measurement with a heating rate of 0.67 °C/min showed a consecutive formation of two phases at  $\sim 256$  °C and  $\sim 337$  °C. The first phase was found to be the hexagonal elemental Dy, space group  $P6_3/mmc$  (#194), with the unit cell dimensions,  $a=3.60(6)$  Å and  $c=5.696(1)$  Å. The second phase was found to be the cubic C15 Laves phase,  $\text{DyFe}_2$ , space group  $Fd\bar{3}m$  (#227), with the unit cell dimension,  $a=7.375(2)$  Å. The possible third intermediate phase was not observed in the diffraction data.

## **ACKNOWLEDGEMENT**

I would like to thank my supervisors, Prof. Bob Cywinski and Dr Sue Kilcoyne, for their help and support.

I would also like to thank my supportive colleagues, and the magnetism and superconductivity group at our school.

I would also like to thank the University of Aleppo for the sponsorship of my study at the University of St. Andrews.

I would also like to thank the University of St. Andrews for giving me the opportunity to study here.

Finally, I would like to thank my wife, my family and Prof. Hussein Iskef back in Syria, the people whom to I will remain indebted all my life.

*To my wife.*

# CONTENTS

## 1. Introduction

## 2. Sample Preparation

### 2.1 Introduction

### 2.2 Definition of Amorphous

### 2.3 Techniques For Producing Amorphous Metallic Alloys

### 2.4 Sample Preparation

#### 2.4.1 Arc Furnace

#### 2.4.2 Melt Spinner

### 2.5 Choice of Material

### 2.6 Verification of Sample Amorphicity

## 3. Crystallisation of $\alpha$ -Ni<sub>33</sub>Zr<sub>67</sub>

### 3.1 Introduction

### 3.2 Results

#### 3.2.1 DSC

#### 3.2.2 Neutron Diffraction on POLARIS

### 3.3 Discussion

## 4. Crystallisation of $\alpha$ -Dy<sub>7</sub>Fe<sub>3</sub>

### 4.1 Introduction

### 4.2 Results

#### 4.2.1 DSC

#### 4.2.2 Neutron Diffraction on POLARIS

#### 4.3 Discussion

### 5. **Summary, Conclusions and Future Work**

#### 5.1 Summary and Conclusion

#### 5.2 Future Work

## **Appendix**

### **A. Experimental Techniques**

#### A.1 Introduction

#### A.2 Neutron Diffraction

##### A.2.1 The Pulsed Neutron Source "ISIS"

##### A.2.2 The Neutron Powder Diffractometer "POLARIS"

#### A.3 Crystal Structure Determination from Neutron Diffraction

##### A.3.1 Principle of Structure Determination

##### A.3.2 Crystal Structure Investigation by Neutrons

###### A.3.2.1 Bragg's Law

###### A.3.2.2 Diffracted Intensity

#### A.4 Rietveld Refinement

##### A.4.1 Rietveld Method For a Single Wavelength Neutron Powder Diffraction

##### A.4.2 Principle of Fitting Diffraction Pattern

###### A.4.2.1 Least-Squares Refinement

###### A.4.2.2 Least-Squares Parameters

##### A.4.3 Rietveld Method for Time of Flight Neutron Powder Diffraction

#### A.5 Thermal Analysis (Calorimetry)

##### A.5.1 The Differential Scanning Calorimeter DSC7

## **References**

# CHAPTER I

## INTRODUCTION

Rare-earth transition-metal (RE-TM) compounds are very important both from a fundamental and a technological point of view, and there is an increasing demand of RE-TM alloys in modern technology. These compounds exhibit exceedingly interesting electronic and magnetic features, because of the open 4f-shell of the rare-earth ions that maintains their localisation in all material states [w1]. For instance the most fundamental aspects of spin fluctuations, moment formation and magnetic order can be probed by varying magnetic exchange, anisotropy, conduction electron density and local environment and all of these are offered by these compounds [1]. In addition, these materials are well used in today's industry to make hard magnets, improved magnetic data storage devices and giant magneto-resistive media (see for example refs. [1, 2]).

There is a constant need to discover new materials, whose properties can be tailored to meet the demands of modern technology. This need drives us to search in the structural and magnetic phase diagrams for a suitable material. However, when one looks in the structural phase diagrams of binary rare-earth transition-metal systems published in international tables, it is found that most of these systems are well studied and the most main phases are identified and one will arrive to the conclusion that only minor adjustments to the phase diagram need to be obtained. No completely new binary RE-TM phases have been discovered for a long period of time. One of the shortcomings of standard methods of determining equilibrium phase diagrams is that it is done under conditions, which are far from equilibrium: *i.e.* annealing binary

mixtures at specific temperatures for determined periods of time, and subsequently quenching at very high cooling rates in the hope of maintaining the phases in the proportions which have been formed at those annealing temperatures [3].

The limitations imposed by these techniques can be overcome by the use of new techniques - *e.g. in situ* kinetic neutron powder diffraction - which enables researchers to observe the whole process of the phases formation and transformation from their beginning through any intermediate phases which might form through to the final phase. It also offers the possibility of identification these new phases. This new method has been in use for the last few years. For example: In recent studies using kinetic neutron diffraction techniques, new phases have been found such as the inter-metallic compound FeY, (see figure 1.1), which is only stable over a temperature range of 40° C or at room temperature when it coexists with pure Y [4]. Similar new binary magnetic and crystallographic phases have been observed in re-crystallisation of other binary systems such as Er-Fe (see figure 1.2) and Y-Co [5].

The technique of kinetic neutron diffraction exploits the characteristics of the most powerful neutron sources, for example, D20 steady state neutron diffractometer at ILL [w2] and pulsed neutron powder diffractometer (POLARIS) at ISIS [6,7]. Researchers can carry out kinetic neutron diffraction in real time on phase transformation and reaction, and compare the results to those from complementary techniques such as Differential Thermal Analysis DTA and Differential Scanning Calorimetry DSC.

In this thesis I will describe the crystallisation of amorphous  $\text{Ni}_{33}\text{Zr}_{67}$  and  $\text{Dy}_7\text{Fe}_3$  alloys using kinetic neutron diffraction and DSC. The binary amorphous rare-earth transition-metal alloys at eutectic compositions are annealed at constant low heating rates and at the same time neutron diffraction data are collected at fixed time intervals.

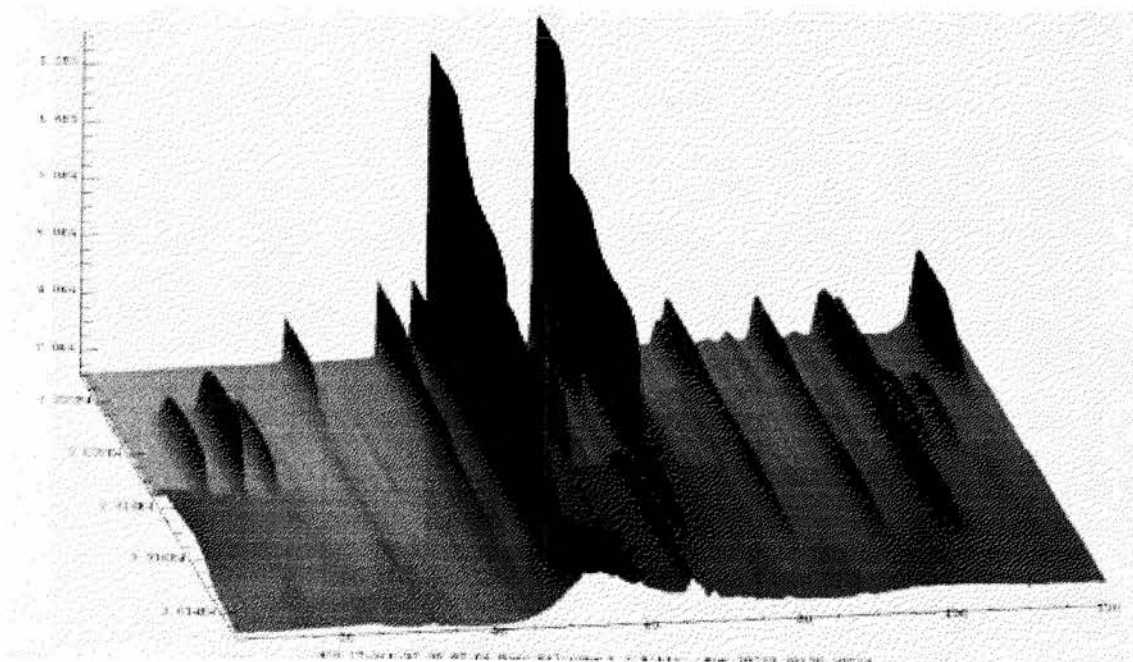


Figure 1.1 Neutron thermogram of crystallisation of  $\alpha\text{-Y}_7\text{Fe}_3$  taken at D20 at ILL. The annealing temperature ramps steadily from 250 °C to 550 °C. Note the appearance of the new intermediate Y-Fe phase between 400 °C and 450 °C. The final phase is Y and  $\text{YFe}_2$ .

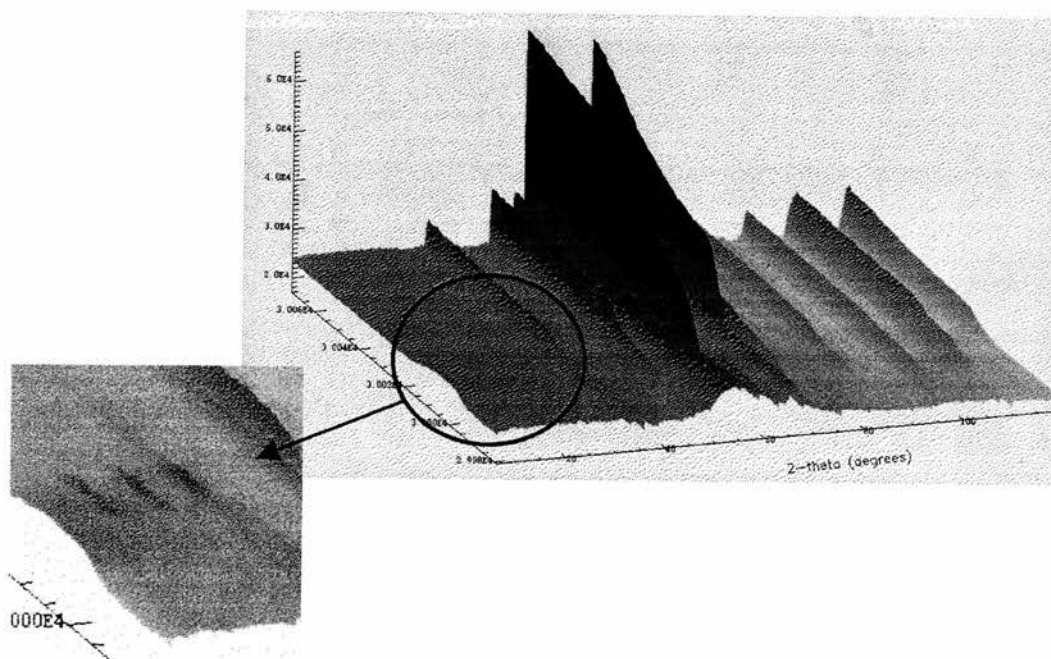


Figure 1.2 Neutron thermogram of crystallisation of  $\alpha\text{-Er}_7\text{Fe}_3$  taken at D20 at ILL at similar heating conditions as for  $\alpha\text{-Y}_7\text{Fe}_3$ . The inset shows the presence of the new intermediate Er-Fe phase.

Figures reproduced from the talk "**Thermographic studies of novel routes to new compounds**" presented at the International Workshop on Powder Diffraction, Grenoble, France, March 1999, with permission from S H Kilcoyne.

These diffraction patterns are then analysed using CCSL suites of Rietveld refinement programs [8]. For DSC measurements, amorphous rare-earth transition metal alloys are also annealed at constant heat rates and the curves of heat flow rates vs. temperature are observed and exothermic or endothermic areas are identified and a lot of information can be obtained such as the temperatures at which phases form, heats of transitions, specific heats, kinetic parameters (such as activation energies and pre-exponential factor) and rates of re-crystallisation [9-11]. The crystallisation studies offer elaborate knowledge about the stability and the structure of the glass precursors and about the crystalline metallurgical phase diagrams.

Crystallisation process can be separated into three groups:

1. Polymorphic crystallisation leading to only one crystal phase possessing the same composition as the amorphous alloy (*e.g.* see crystallisation of  $\alpha$ -Ni<sub>33</sub>Zr<sub>67</sub> in Chapter III), where there is no gradient of concentration along with the amorphous/crystal interface and crystallisation progresses by a single leap across the interface;
2. Primary crystallisation where the crystalline phase has a different composition from the amorphous alloy, leading to a gradient of concentration across the crystallisation face (*e.g.* see the first phase of the crystallisation of  $\alpha$ -Dy<sub>7</sub>Fe<sub>3</sub> in Chapter IV); and
3. Eutectic crystallisation leading to complementary growth of two or more crystalline phases (*e.g.* see the second phase of the crystallisation of  $\alpha$ -Dy<sub>7</sub>Fe<sub>3</sub> in Chapter IV). The overall composition across the interface remains the same. The progress of the crystallisation is done by diffusive interaction parallel to the crystallisation interface.

The preparation of my samples is presented in chapter II.. The results of my experiments and their discussions are given in chapter III for the Ni-Zr system and in chapter IV for the Dy-Fe system. The results of this work are summarised and general conclusions are drawn in chapter V. Finally, an elaborate description of the involved experimental techniques is presented in the Appendix.

## CHAPTER II

### SAMPLE PREPARATION

#### 2.1 INTRODUCTION

This chapter will deal with the preparation of the amorphous samples I have studied. I will explain what is meant by amorphous and mention the many methods of preparing amorphous materials. Then, I will briefly describe each technique and discuss the technique I used, melt spinning in detail. Finally, I will show how the materials were chosen, and how the amorphicity of the final samples were checked.

#### 2.2 DEFINITION OF AMORPHOUS

Solid materials are in one of two forms, either crystalline or amorphous. When a material is in crystal form, its atoms are arranged periodically, *i.e.* the atoms are repeated in the same pattern or "unit cell" over and over as demonstrated in figure 2.1. However, in amorphous materials no such periodicity exists but short range order does exist, namely the bonds existing between nearest neighbour atoms are at fixed angles. However, second and higher nearest neighbours are at random angles as illustrated in figure 2.2.

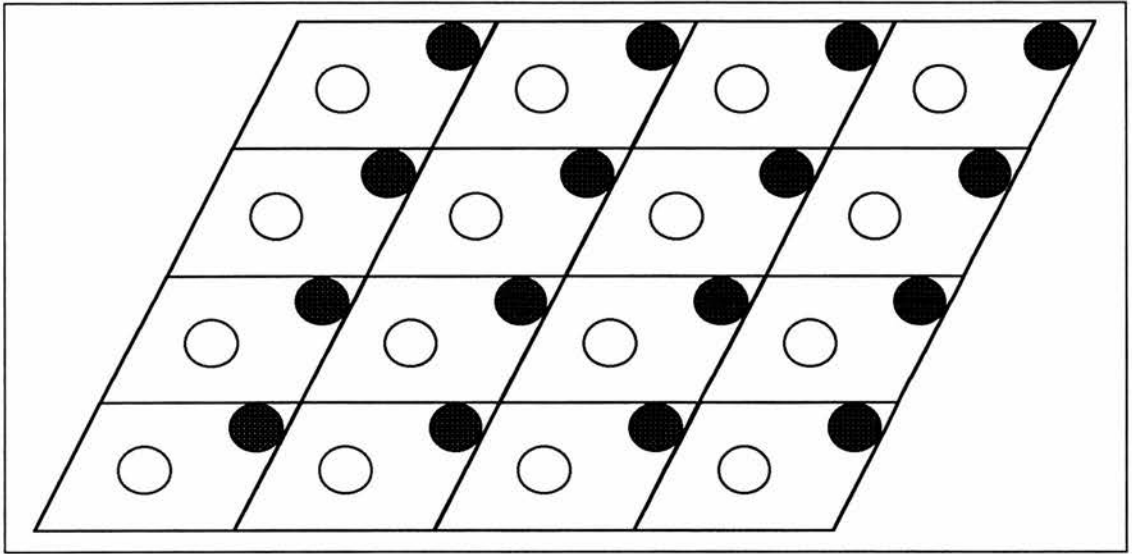


*Figure 2.1 Two-dimensional representation of a crystal lattice.*

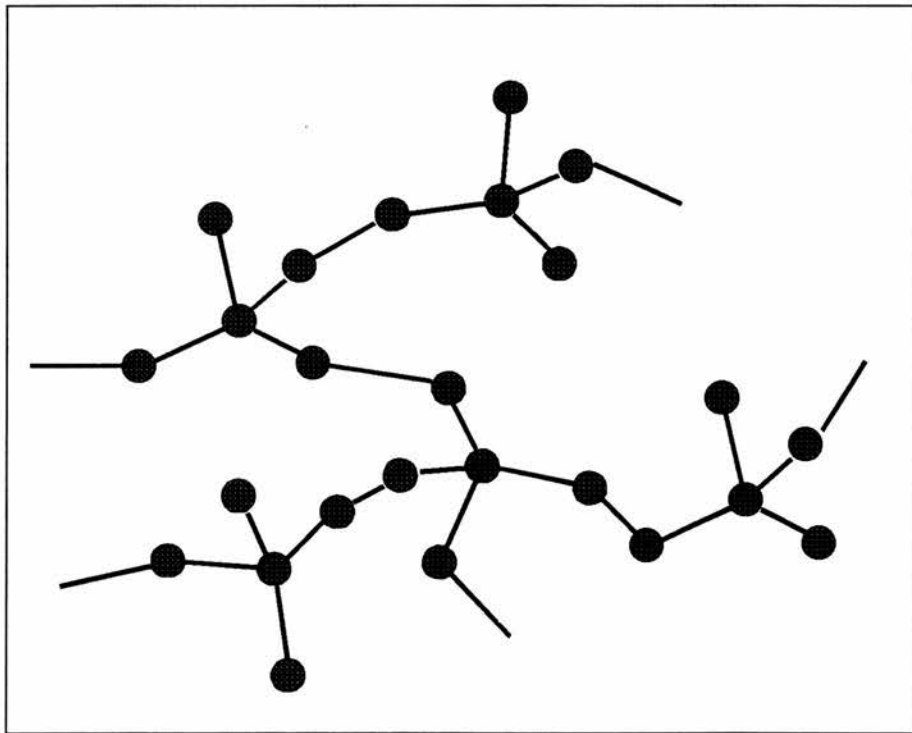


*Figure 2.2 A representation of atomic aggregation in an amorphous material showing short range order.*

## 2.3 TECHNIQUES FOR PRODUCING AMORPHOUS METALLIC ALLOYS

There are many ways to produce amorphous solids from the vapour, liquid or solid phase of a material. In this section a brief description of each of these techniques will be given and a more detailed description on the technique I used, melt spinning, will be given in section 2.4.2.

**Thermal evaporation:** In thermal evaporation the starting alloy is vaporised and collected on a cold substrate. The atoms are positioned randomly and form an amorphous thin film.

**Sputtering:** In the sputtering technique the starting material is bombarded by energetic ions either from an ion gun or from low-pressure plasma. The atoms of the material will be plucked out one by one by the striking ions and deposited onto a cold substrate, giving rise to an amorphous material.

**Liquid quenching:** When a liquid melt is solidified very rapidly, atoms may not have enough time to be arranged into an ordered structure resulting in an amorphous material. The minimal cooling rate to suppress crystallisation differs for different compounds, but it is usually of the order of  $10^6 \text{ KS}^{-1}$ .

There are many known techniques to perform this process such as "splat cooling" where a droplet of a molten material is accelerated by a shock wave to splat violently on a cold metal surface forming an amorphous solid. Another technique is called "hammer-and-anvil" where a melted droplet is quenched by hammering it against a

cold metal. Finally the melt spinning technique, wherein the molten material is quenched by pushing it onto a rapidly spinning wheel.

## **2.4 SAMPLE PREPARATION**

All the samples described in this thesis were made at School of Physics at University of St. Andrews. My samples were prepared in two stages. First, The constituent elements were melt together by using the argon arc furnace resulting in polycrystalline ingots. Then, the polycrystalline ingots by using the melt spinner were transformed into thin amorphous ribbons.

A detailed description of these two techniques are given in the following two sections.

### **2.4.1 ARC FURNACE**

To make an alloy, stoichiometric amounts of the constituent elements are placed together in water-cooled copper hearth argon-arc furnace. A picture of this furnace is shown in figure 2.3. The chamber of the furnace is then closed and evacuated to  $\sim 8 \cdot 10^{-2}$  Torr\*, then filled with argon gas to the pressure of 5"Hg\*. This processes is repeated several times to ensure an active-gas free environment. Then the final argon gas pressure is set to 23"Hg\*. A very high temperature (The maximum temperature can be obtained is  $\sim 3500$  °C) argon arc is obtained by applying a very high voltage (The maximum electrical current can be obtained is 400 A) between the electrode bar and the copper hearth. First, a titanium getter is melted to absorb any remaining impurity gases and then it is allowed to cool down and solidify, and its colour is checked. If there is a colour change it would mean that there were reactive gases in the

---

\* Different pressure units appeared in the text as read from different pressure gauges.

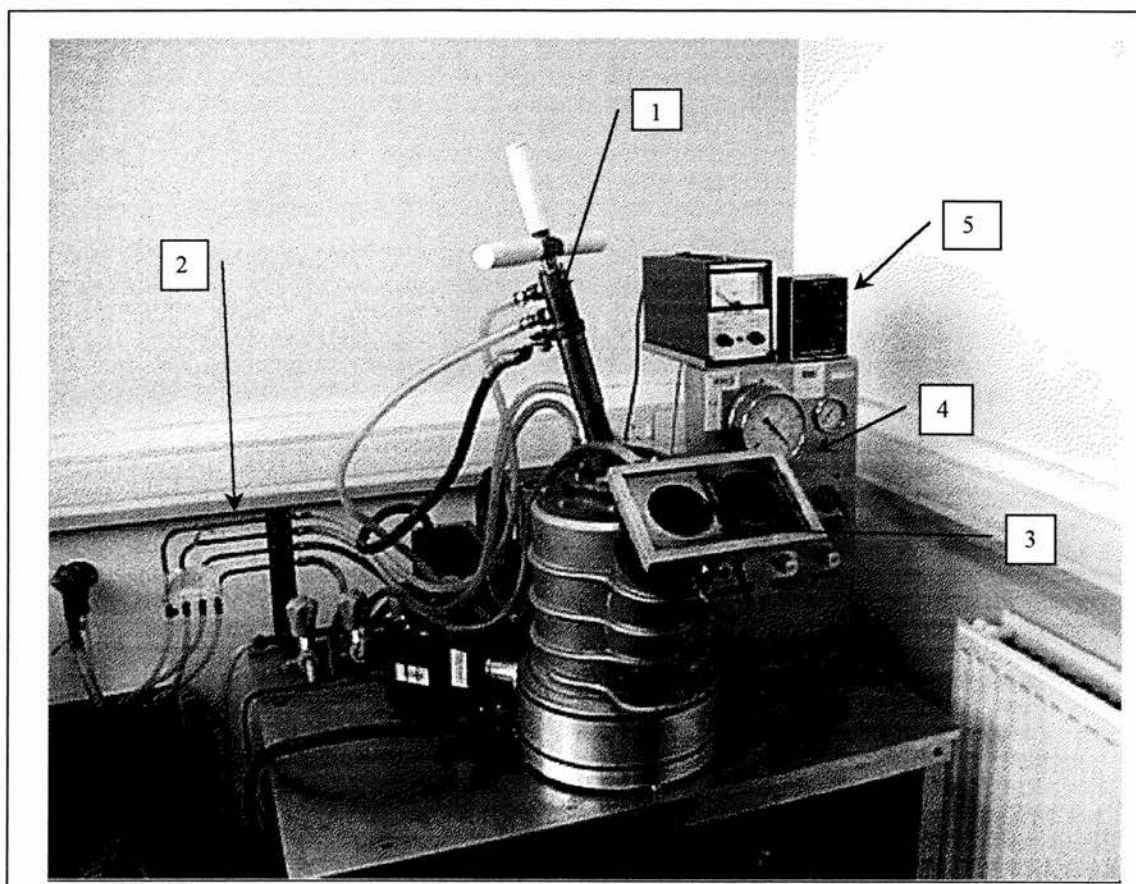


*Figure 2.3 A picture of the arc furnace we used to make the polycrystalline alloys. One can see the melting anode stick (1) at the top of the apparatus, cooling water pipes(2), sample viewing window (3) with its light protective glass slide aside, on the right pressure control unit (4) and on the top right, current control (5).*

chamber, and the sample preparation would be halted and repeated from the beginning. If there is no colour change the sample preparation is continued and the arc is formed again but this time to melt the sample. Once the sample is melted it is allowed to cool and solidify. The sample is re-melted several times (usually 4 to 5 times) to ensure its homogeneity

#### **2.4.2 MELT SPINNER:**

A picture of the melt spinner is shown in figure 2.4, with a close up of the wheel shown in figure 2.5 and illustrated diagrammatically in figure 2.6. The main components are-

- a) A quartz tube placed inside an RF coil.
- b) A copper-made spin wheel which is around 1.4 cm in width and 12 cm in radius.
- c) A Collection box.

First the sample ingot is cut into small pieces and then (~0.6-1.3 gr) of the material is placed inside the quartz tube. The tube is mounted inside the coil and above the rapidly spinning wheel. After assuring an inert atmosphere in the collection box by continually passing argon gas through, a high frequency (RF) current is passed through the coil to melt the sample. Once the sample is molten (which will usually takes few seconds), it is pushed by argon gas (usually of the pressure of 8 lbf/in<sup>2</sup>) through an orifice (~1mm in diameter) at the bottom of the quartz tube onto the spinning copper wheel. The spinning wheel, which is usually set to the speed of 74 m.s<sup>-1</sup>, quenches the sample rapidly at a rate of ~10<sup>6</sup> K.s<sup>-1</sup> and throws the amorphous ribbons into the collection box as shown in figure 2.5.

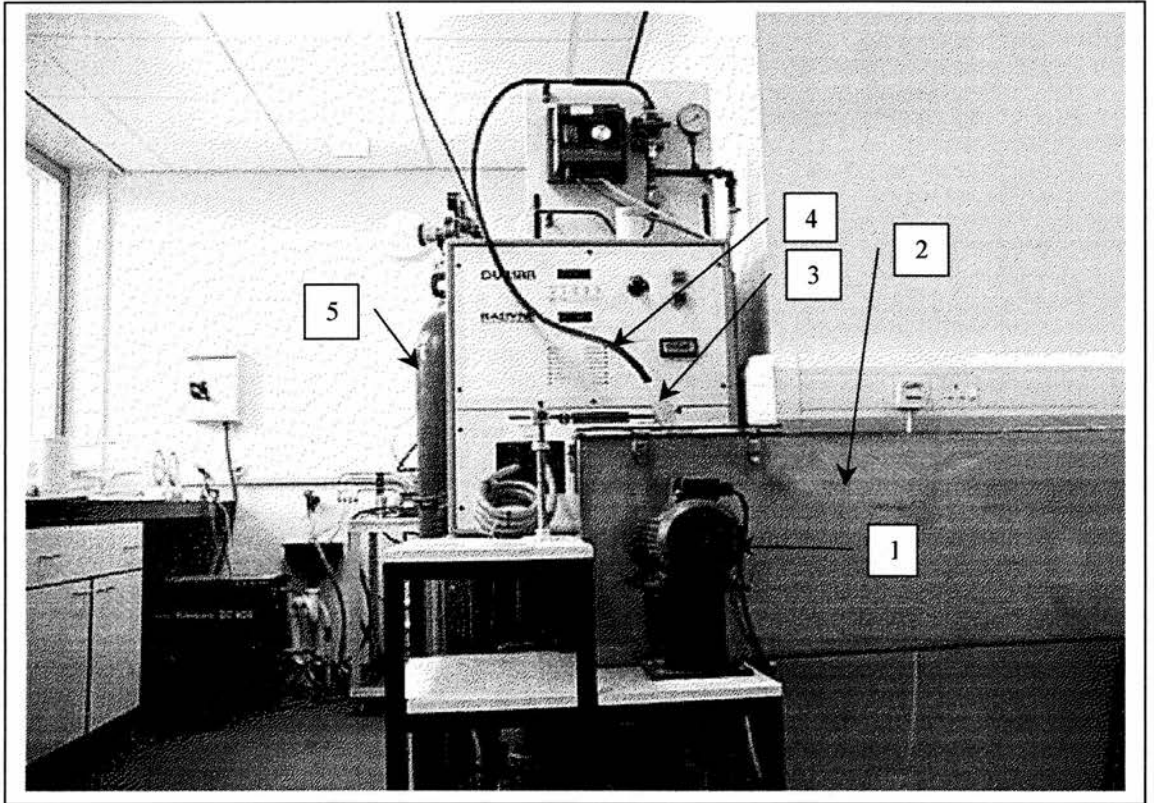


*Figure 2.4 The melt-spinner. At the front one can see the motor (1) and the ribbon collection box (2). Above is mounted the quartz tube (3) connected with a pipe (4) to argon gas supply (5).*

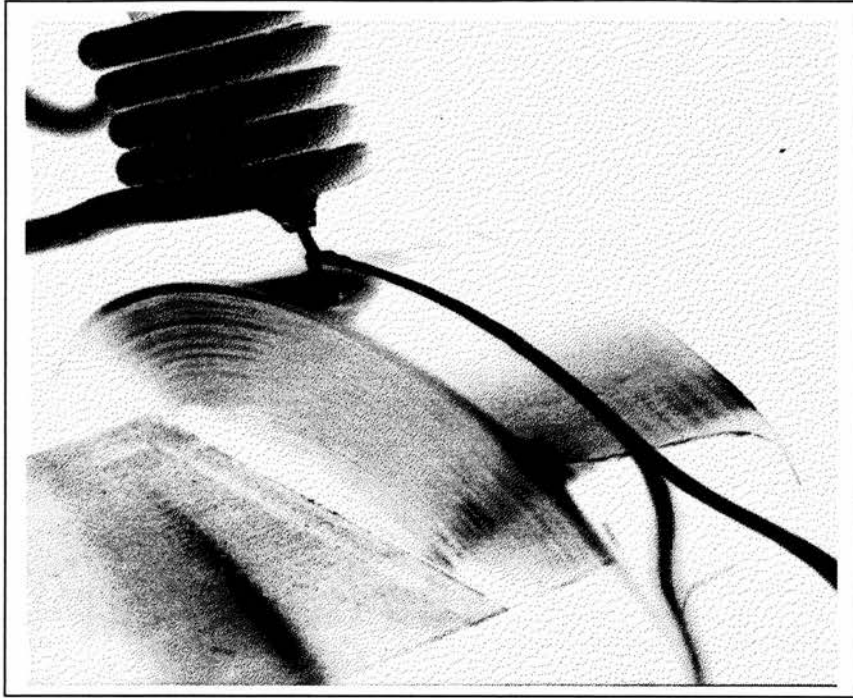


*Figure 2.5 Spin-wheel and melting coil producing an amorphous ribbon from the molten sample blown down from the holding quartz tube.*

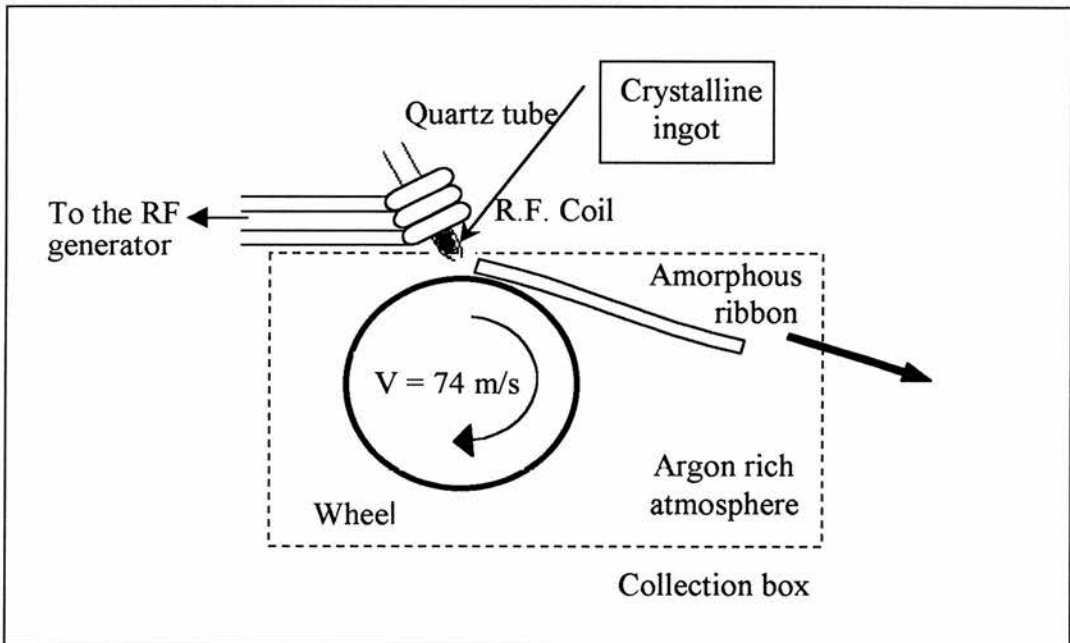


*Figure 2.6 A diagram of the main parts of the melt spinner unit.*

## 2.5 CHOICE OF MATERIAL

The phase diagram is an essential guide when preparing amorphous materials. From the phase diagram we can determine the eutectic compositions, and it is usual to choose the composition of the sample to correspond with that of the lowest eutectic point. This is important because at this composition there are several advantages we can gain, some of which:

- a) The lower the melting point, the more easily the melting is achievable.
- b) All constituent phases melt at the same time at the same temperature, as a result the composition of the liquid melt remains constant and homogenous.

However, choosing the composition at the eutectic is not always the case. Amorphous alloys can be made at different compositions as long as the composition is in close neighbourhood of a eutectic. Otherwise, we might get completely different melting temperatures for the constituents leading to inhomogeneity.

From phase diagrams shown in figures. 2.7 and 2.8, it can be seen that the deepest eutectic is close to  $X_7Y_3$  (where, X is Zr or Dy, and Y is Ni or Fe). The starting compositions for my amorphous samples are  $Ni_{133}Zr_{67}$  and  $Dy_7Fe_3$ . It should be noted that  $Ni_{133}Zr_{67}$  is not chosen as a eutectic but as a single-phase alloy.

## 2.6 VERIFICATION OF SAMPLE AMORPHICITY

A simple test, to give some indication of whether the samples are amorphous or not, is to fold them. Samples that are very brittle and crumble when bent are often crystalline, while those are very ductile and can be creased without being broken are usually amorphous. However that is not very reliable and quantitative way to measure

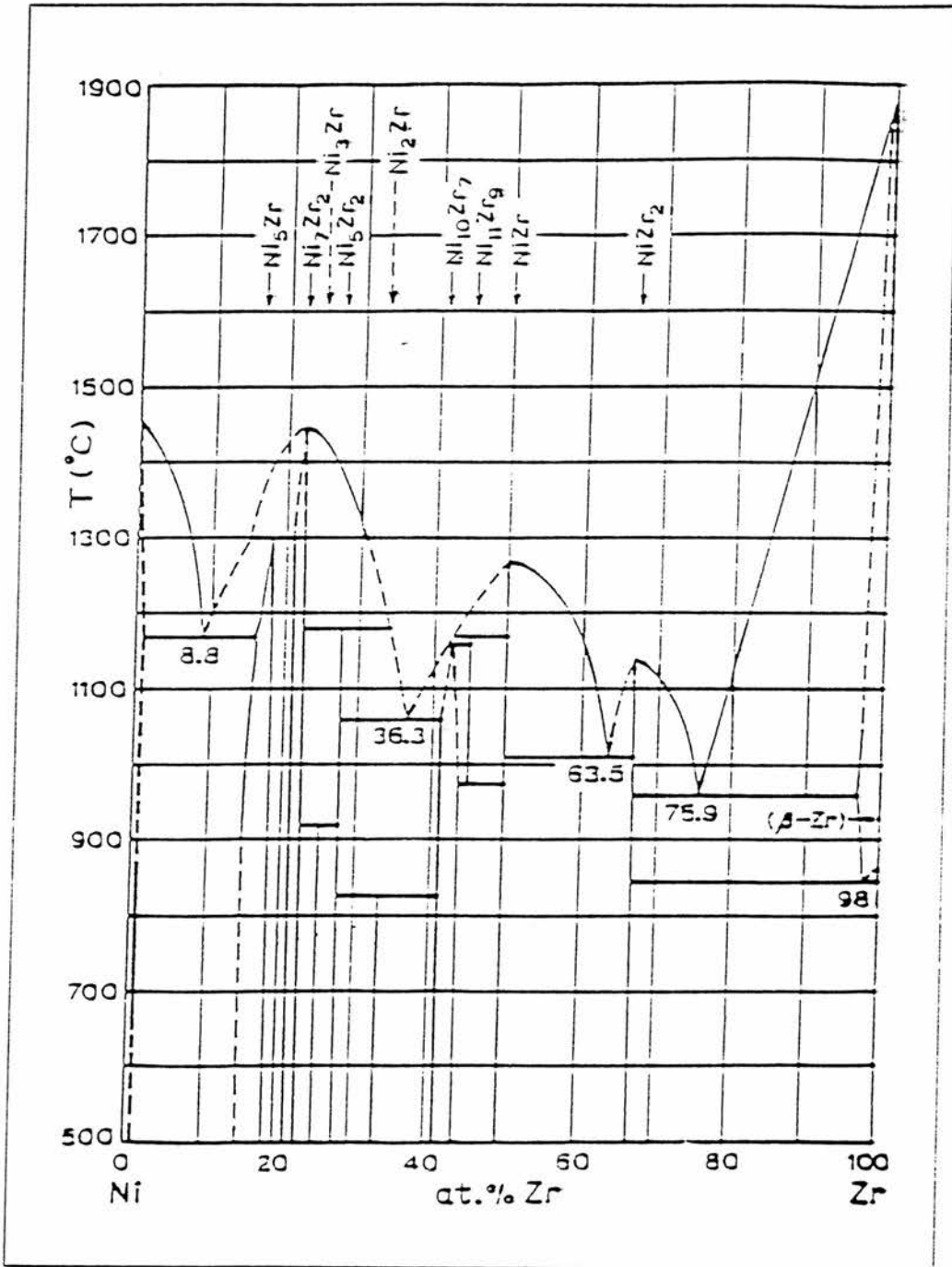


Figure 2.7 The Ni-Zr equilibrium phase diagram [12].

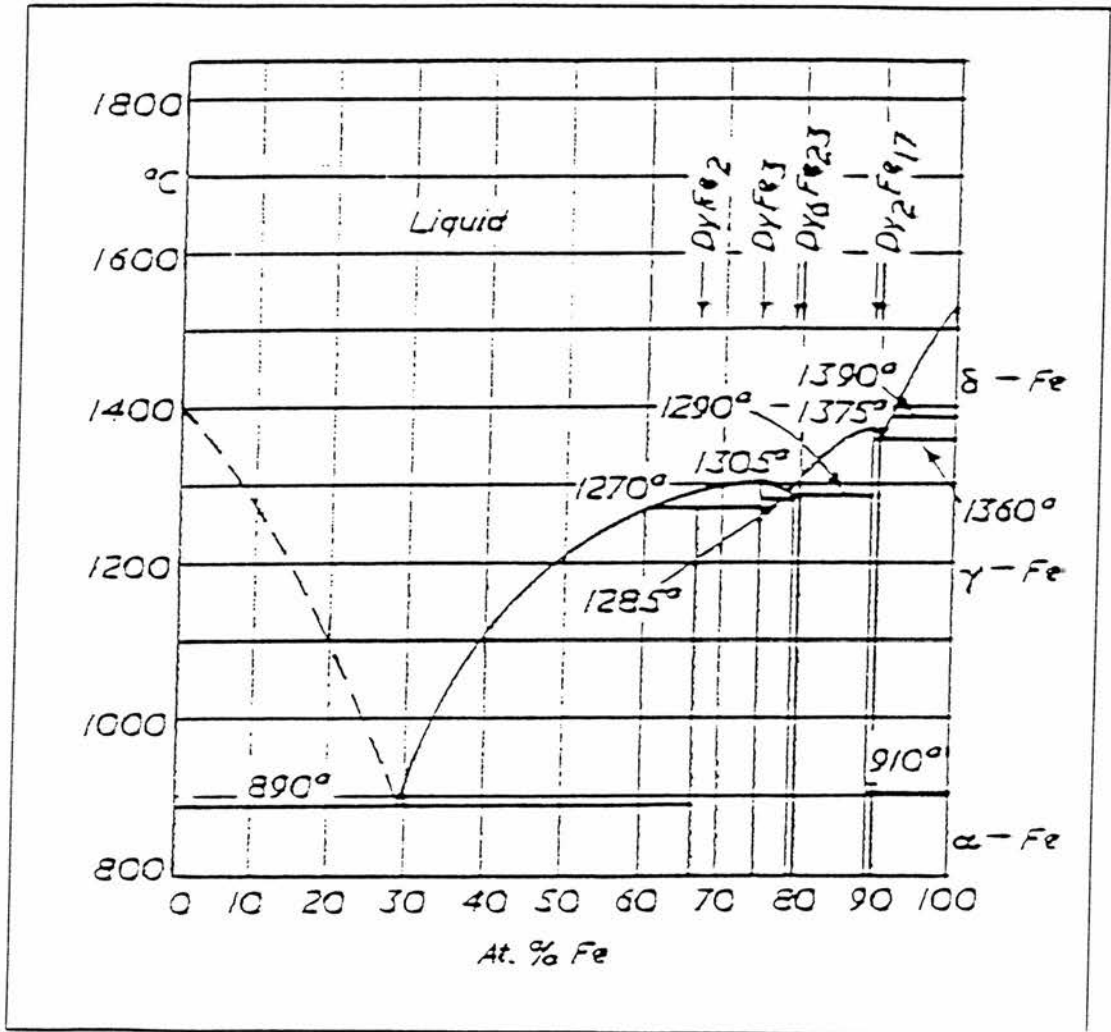
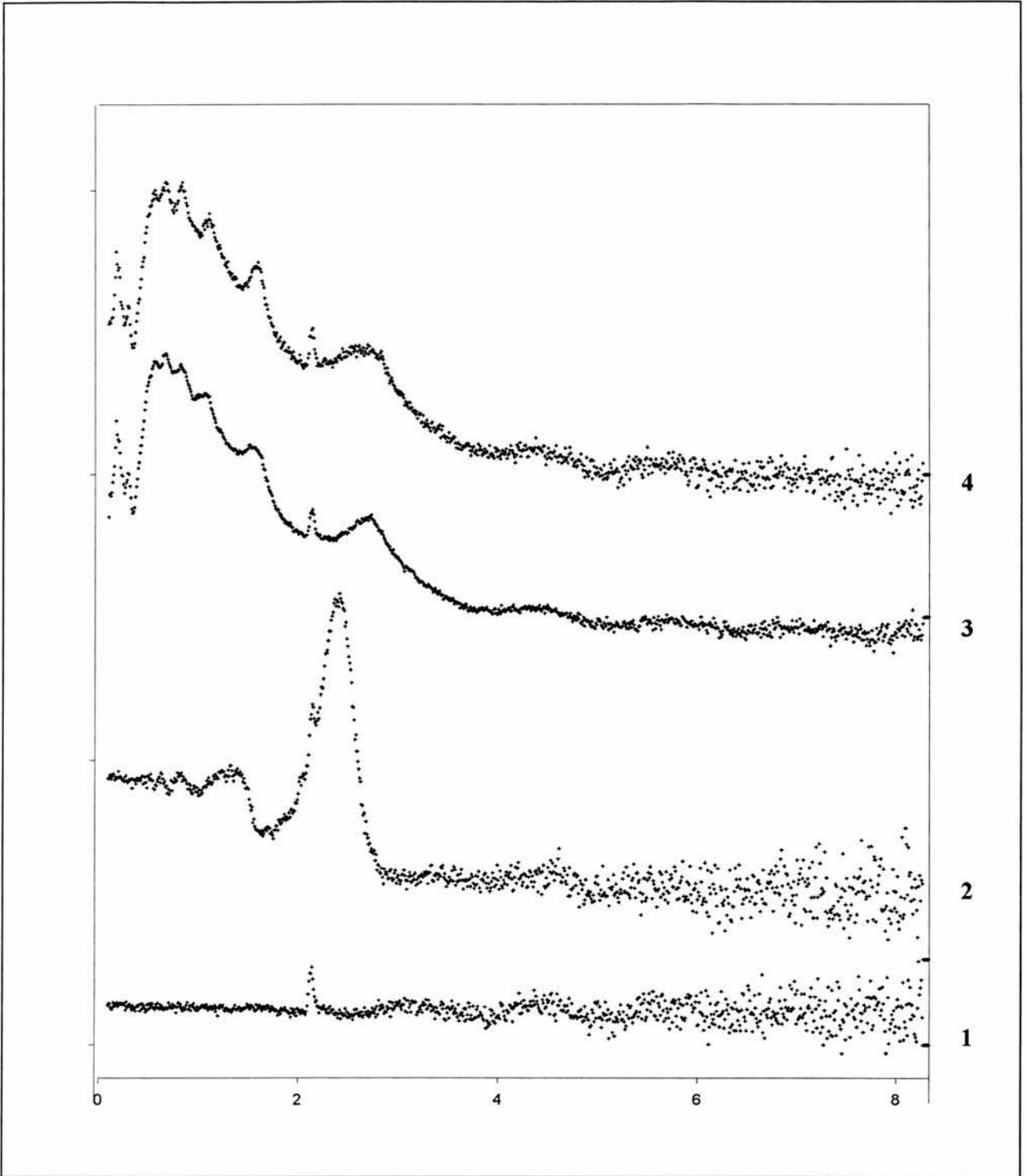


Figure 2.8 The Dy-Fe equilibrium phase diagram [13].

samples amorphicity. In order to confirm the amorphous nature of the material, neutron powder diffraction patterns of my samples were collected at room temperature. The details of the powder neutron diffraction technique are given in the Appendix. Amorphous samples give diffraction patterns with few very broad peaks, which result from local short-range order of their atoms (atomic pair correlations). Figure 2.9 shows the diffraction patterns at room temperature of the samples I made, amorphous  $\text{Ni}_{33}\text{Zr}_{67}$ , and  $\text{Dy}_7\text{Fe}_3$ .



**Figure 2-9.** Neutron diffraction patterns of the amorphous samples I studied. Pattern (1) is for the sample Vanadium can, and it has a sharp peak at  $d=2.14\text{\AA}$  which appears in all samples. Pattern (2) is the diffraction pattern of  $\text{Ni}_{33}\text{Zr}_{67}$ , (3) is of  $\text{Dy}_7\text{Fe}_3$ , (4) is of  $\text{Dy}_7\text{Ni}_3$ .

## CHAPTER III

### CRYSTALLISATION OF $\alpha$ -Ni<sub>33</sub>Zr<sub>67</sub>

#### 3.1 INTRODUCTION

The Ni-Zr equilibrium phase diagram is shown in chapter II (figure 2.7). The liquidus and solidus temperatures are not very well established, (dotted lines). There are nine intermediate phases. The intermediate phases, Ni<sub>7</sub>Zr<sub>2</sub>, NiZr, and NiZr<sub>2</sub> all melt congruently; the intermediate phases, Ni<sub>5</sub>Zr, Ni<sub>5</sub>Zr<sub>2</sub>, Ni<sub>10</sub>Zr<sub>7</sub>, and Ni<sub>11</sub>Zr<sub>9</sub>, form by peritectic reactions; and Ni<sub>2</sub>Zr and Ni<sub>3</sub>Zr form by a peritectoid reaction. There are twelve invariant reactions in the system including four eutectic, four peritectic, two eutectoid and two peritectoid. The intermediate phases Ni<sub>5</sub>Zr, Ni<sub>3</sub>Zr, and Ni<sub>10</sub>Zr<sub>7</sub> have finite solid solubilities and the others are stoichiometric. The solid solubility of Zr in (Ni) is less than 1 at. % and that of Ni in ( $\beta$ Zr) is 2.92 at. % at the eutectoid temperature [14].

Over the last few decades the Ni-Zr family and the crystallisation of  $\alpha$ -Ni<sub>x</sub>Zr<sub>1-x</sub> has been studied exhaustively. In 1953, Hayes *et al* were the first to report the existence of NiZr<sub>2</sub> compound from polycrystalline diffraction data [15], and Kirkpatrick *et al* determined its crystal structure by single crystal method in 1962 [16]. In 1983 Altounian *et al* carried out a comprehensive study of the crystallisation of  $\alpha$ -Ni<sub>x</sub>Zr<sub>1-x</sub> (x=0.20-0.70) to study the stability of these glassy states and they found that they are in the most stable state at eutectics [12]. Using Perkin-Elmer DSC-2C, transmission electron microscopy

(TEM) and electron diffraction, Altounian *et al* [17] studied, the crystallisation of the metallic glass NiZr<sub>2</sub> from melt spun precursors formed at different temperatures and found that they all crystallise polymorphically into NiZr<sub>2</sub> with no phase separation. In 1987 Fen *et al* reported their observation of micro-twin structure in crystallised NiZr<sub>2</sub> alloy [18]. Sutton *et al* in 1989 reported their observation of a precursor phase during the crystallisation of  $\alpha$ -NiZr<sub>2</sub> [19]. In 1991, Brauer *et al* identified the precursor phase as a transient metastable crystal formed before the equilibrium NiZr<sub>2</sub> phase is reached, has the space group  $O_h^7$  (Fd3m) with lattice parameter of 12.61(1) Å [20]. In 1994, Ghosh derived the thermodynamic parameters of all stable phases in the Ni-Zr system in an effort to explain the formation of metastable nanocrystalline and crystalline phases under an imposed kinetic constraints [14], and Erukhimovitch *et al* proposed an integral equation for the time-dependence evaluation of the transformed phase volume fraction in the crystallisation process instead of the famous Avrami equation [21]. In 1996, Lu *et al* found that NiZr<sub>2</sub> nanophase consists of ultrafine lamellae with thickness of a few nanometer and found well defined twin boundaries between the neighbouring lamellae [22].

Despite all this work on the Ni<sub>x</sub>Zr<sub>1-x</sub> system, no *in situ* neutron or X-ray diffraction studies have been carried out on the crystallisation of  $\alpha$ -Ni<sub>x</sub>Zr<sub>1-x</sub> in dynamic mode i.e. with linearly increasing temperature. This process gives us an opportunity to observe the true behaviour of the whole crystallisation process. In this chapter I will present the results of a study of the crystallisation of  $\alpha$ -Ni<sub>33</sub>Zr<sub>67</sub>, the composition which corresponds to the congruently melting compound NiZr<sub>2</sub>, by using two different techniques DSC and kinetic neutron diffraction.

## 3.2 RESULTS

### 3.2.1 DSC

The DSC measurements were carried out using Perkin-Elmer DSC7 differential scanning calorimetry, which is described in detail in the appendix, section (A.5.1). A few milligrams of the amorphous sample,  $\text{Ni}_{33}\text{Zr}_{67}$ , were tightly encapsulated in a standard aluminium sample pan with a cover. First, two empty sample capsules were placed into the instrument and heated linearly at a constant heat ramp rate, 10 K/min, over a determined range of temperature, 50-450 °C. The baseline, which represents the background, was obtained. One of these empty capsules then removed and replaced by a capsule containing our sample,  $\alpha\text{-Ni}_{33}\text{Zr}_{67}$ . The measurement was repeated under the same thermal conditions, and the heat flow vs. temperature curve was obtained after the base line was subtracted by the DSC7 computer software. The parameters of this experiment are tabulated in Table 3.1.

DSC measurements carried out at this stage of research, were to form an initial idea of, the number of phases would appear in the course of annealing amorphous alloys over a limited ranges of temperature at constant heating rates, (10 °C/min for all of my samples), and the temperatures at which these phases would form. These measurements can also help in planning experiments at ISIS and ILL where the experiments are expensive and the beam time offered is very limited.

The results of the DSC measurements are shown in figure 3.1. From this figure we can see that an exothermic dip occurs at a temperature of about 392 °C. This means that

$\alpha\text{-Ni}_{33}\text{Zr}_{67}$

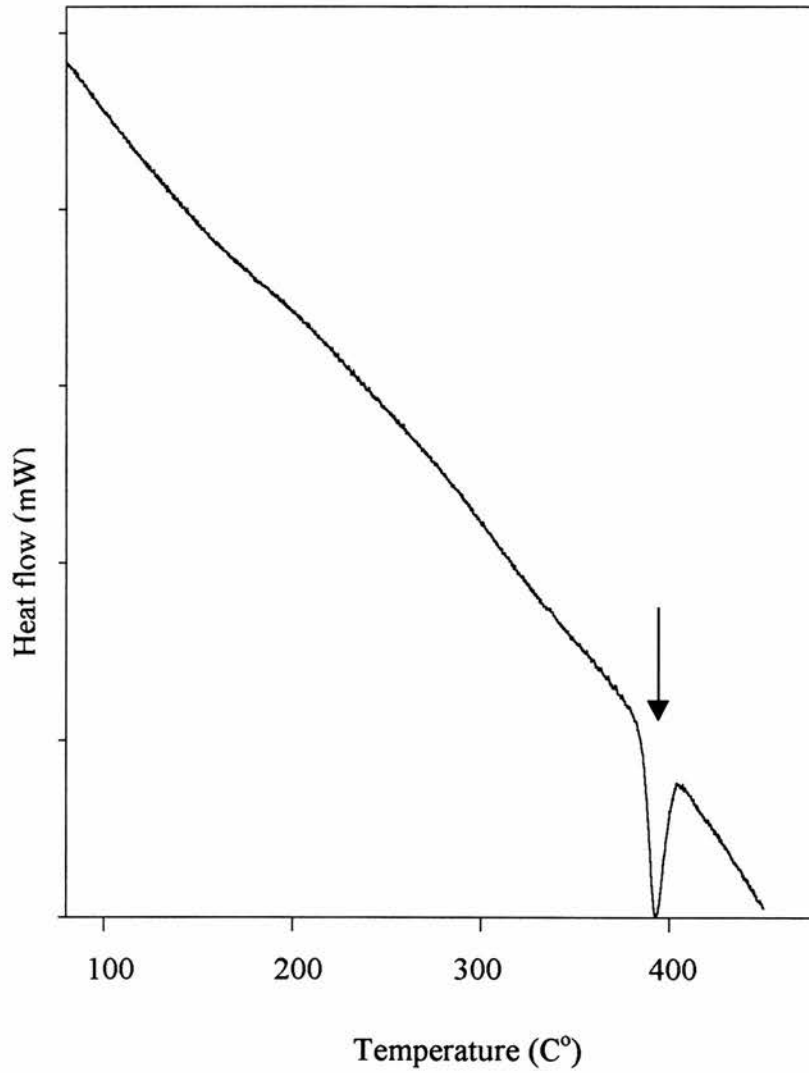


*Figure 3.1 Heat flow curve vs. Temperature for  $\alpha\text{-Ni}_{33}\text{Zr}_{67}$  taken by DSC7 at scanning rate of  $10\text{ C}^\circ/\text{min}$  with the base line subtracted. The arrow shows the temperature of the exothermic dip, ( $\sim 392\text{ C}^\circ$ ).*

phase formation occurred around this temperature, which released energy to evolve because it is an exothermic process. Examining the whole curve shows that only one phase has been formed.

### 3.2.2 NEUTRON DIFFRACTION ON POLARIS

2.17 g of amorphous  $\text{Ni}_{33}\text{Zr}_{67}$  was loaded into a vanadium can, attached to the end of a sample stick in the RALF1 furnace and exposed to a high flux intensity of a white beam of pulsed slow neutrons. It was then heated from room temperature to 464 °C at a constant heat ramp rate of 1 °C/min. Diffraction spectra were collected continuously every 12 minutes. The sample used and the parameters of this experiment are shown in detail in Table 3.1. Refinements of the diffraction spectra from the re-crystallisation products were carried out using the CCSL Rietveld refinement program [8].

Table 3.1

<i>The amorphous sample</i>	<b>DSC</b>			<b>POLARIS</b>			
	<i>Weight (mg)</i>	<i>Heating rate (°C/min)</i>	<i>Temperature range (°C)</i>	<i>Weight (g)</i>	<i>Heating rate (°C/min)</i>	<i>Temperature range (°C)</i>	<i>Counting Time for each run (min)</i>
$\text{Ni}_{33}\text{Zr}_{67}$	~50	10	50-450	2.17	1	RT- 464	12

Figure 3.2 shows diffraction patterns collected at different temperatures during the crystallisation of amorphous  $\text{Ni}_{33}\text{Zr}_{67}$ . It is clear from this figure that the material remains amorphous until 344 °C, and it suddenly begins to crystallise at the temperature range 345 - 356 °C. A cursory comparison of these patterns with increasing temperature shows that the phase (or phases) which is first formed continues with no following subsequent phase formations or transformations. This will be confirmed later on in the forthcoming discussion.

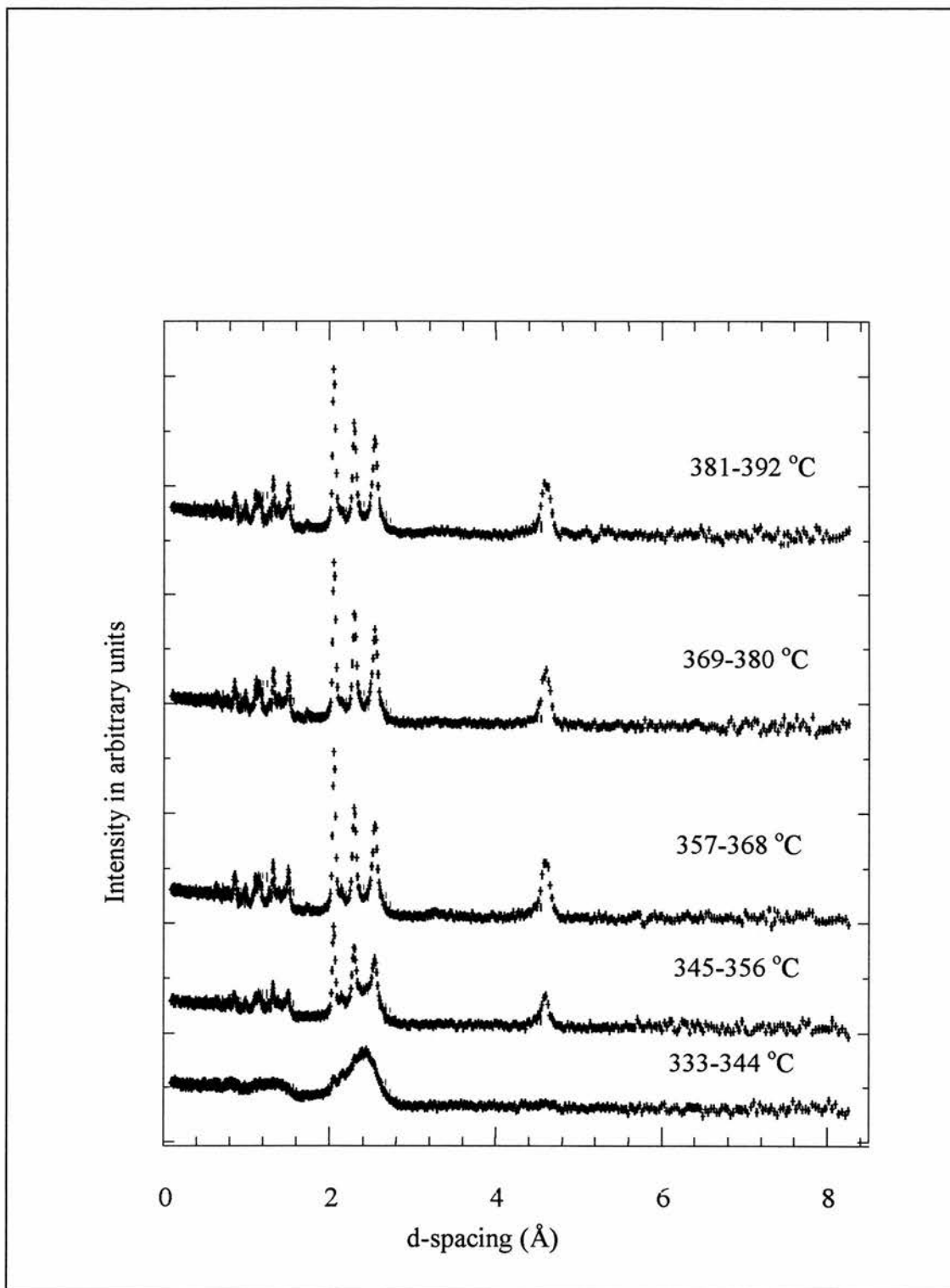


Figure 3.2 Diffraction patterns of re-crystallisation of  $\alpha\text{-Ni}_{33}\text{Zr}_{67}$  taken at POLARIS at different temperatures.

A single-phase Rietveld refinement of the diffraction pattern of the final temperature range *i.e.* 453-464 °C, was carried out using starting parameters for NiZr<sub>2</sub> available from the CDS [23] as shown in the Table 3.2. The resultant parameters from the final refinement are tabulated in Table 3.3. The final refinement obtained using these final parameters is shown in figure 3.3. The Chi-squared of the fit was 1.7576. The results of the correspondent fit were in extremely good agreement with the model represented in Table 3.2. However there were some minor differences. The refined cell dimensions  $a = b = 6.50824(5) \text{ \AA}$ ,  $c = 5.29513(8) \text{ \AA}$  are slightly bigger, 0.32 % and 0.56 %, respectively than the ones listed in Table 3.2. Subsequently, the volume of the observed unit cell is 1.20% bigger than the one listed in Table 3.2. This is because our measurements were made at high temperatures, (453-464 °C), therefore, the expansion of the cell dimensions was expected. After the refinement, the isotropic temperature factors for Ni and Zr were found to be 1.06(3) and 1.20(3)  $\text{\AA}^2$ , respectively.

From figure 3.3 one can notice that some of the peaks were slightly under-fitted, while some others were slightly over-fitted. This is most likely due to the existence of a preferred orientation. For example, when Altounian *et al.*, examined, using transmission electron microscopy TEM and electron diffraction, the 25 % NiZr<sub>2</sub> phase formed by annealing the  $\alpha\text{-Ni}_{133}\text{Zr}_{67}$  at a ramp rate of 40 °C/min to 402 °C, they found that the NiZr<sub>2</sub> phase was in a form of elongated crystals in the remaining amorphous matrix with the (111) planes parallel to the surface [17]. Brauer *et al* [20], showed that the body centred tetragonal (bct) NiZr<sub>2</sub> crystallites, formed by the isothermal annealing at 449 °C, exhibit an extremely high density planar defects, resulting in jagged edges and streaks in their micrograph of partially crystallised Ni<sub>133</sub>Zr<sub>67</sub> and rods in the <110> direction of the single crystal diffraction pattern; and mentioned that these defects seemed to occur for all crystallisation temperatures, with increased density at higher temperatures; and

Table 3.2 Starting refinement parameters (from the CDS [23])

<b>Formula</b> NiZr <sub>2</sub>						
<b>Cell Data</b>						
-----						
Dimensions (Å)			6.4875(2)	6.4875(2)	5.2656(2)	
Angles (deg)			90.000(-)	90.000(-)	90.000(-)	
Volume (Å <sup>3</sup> )			221.617			
Z-Value			4.00			
Space Group Code			I4/mcm			
Space Group No.			140			
R-Factor (%)			4.70			
Number of Atoms			2			
<b>Atomic Parameters</b>						
-----						
Atom	Wyckoff	Occup.	x	y	z	
Ni	4a	422	1.00	0.0000	0.0000	0.2500
Zr	8h	m.2m	1.00	0.1641	0.6641	0.0000

Table 3.3 The resultant parameters from the final refinement.

<b>Formula</b> NiZr <sub>2</sub>						
Chi-squared of the fit						1.7576
Isotropic temperature factors (Å <sup>2</sup> )						
Ni						1.06(3)
Zr						1.20(3)
<b>Cell Data</b>						
-----						
Dimensions (Å)			6.5082(5)	6.5082(5)	5.2951(8)	
Angles (deg)			90.000(-)	90.000(-)	90.000(-)	
Volume (Å <sup>3</sup> )			224.28(7)			
Space Group Code			I4/mcm			
Space Group No.			140			
Weighted profile R <sub>obs</sub> factor						4.69
Number of Atoms			2			
<b>Atomic Parameters</b>						
-----						
Atom	Wyckoff	Occup.	x	y	z	
Ni	4a	422	1.00	0.00000	0.00000	0.25000
Zr	8h	m.2m	1.00	0.16522	0.66522	0.00000

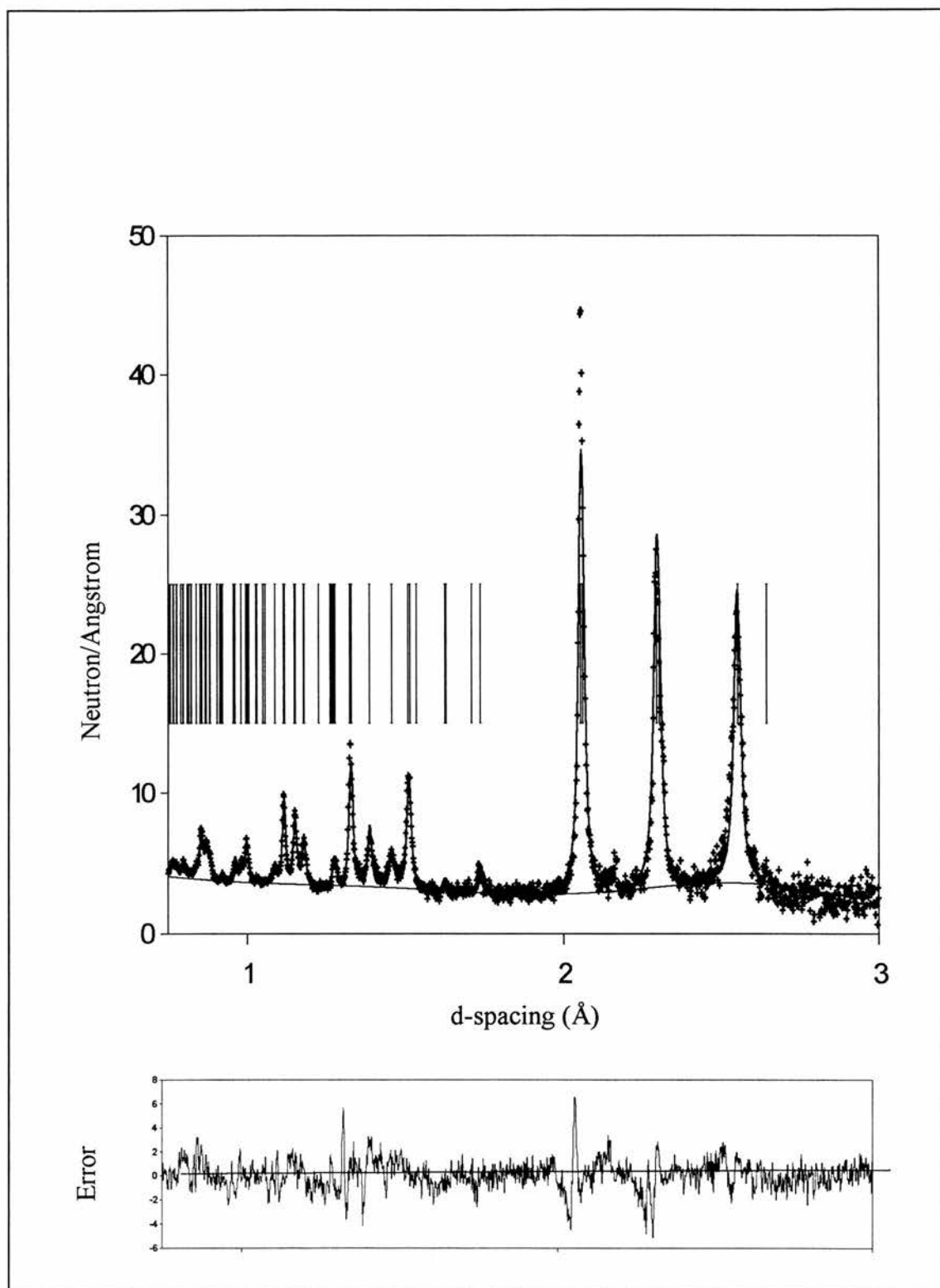


Figure 3.3 A diffraction pattern for re-crystallisation of  $\alpha\text{-Ni}_{33}\text{Zr}_{67}$  taken at the final temperature range, 453-464 °C. The crosses represent the collected data. The line is the Rietveld refinement fit to the data by  $\text{NiZr}_2$  compound. The vertical bars are the reflection indices of  $\text{NiZr}_2$ . The lower figure shows the difference between the measured data and the fit.

referred to the work of Feng *et al* work [18] who ascribed these defects to  $120^\circ$  stacking faults normal to the  $\langle 110 \rangle$  direction, and explained that the high density of these defects deter the bct structure to pack well along a  $\langle 110 \rangle$  direction.

It should also be noted that in a SANS study of the re-crystallisation of amorphous  $Y_{67}Fe_{33}$ , formation of crystallites in the shape of asymmetric micro-discs was explained at that time by the stress induced in the ribbons during the melt-spinning process of the preparation of these amorphous alloys [24]. However in our results, the addition of simple models to explain the preferred orientation did not give better fits and the problem of the preferred orientation will need more work.

I have examined the  $NiZr_2$  phase, formed during the annealing process, in more detail selecting the most prominent three peaks, peak-1, which belongs to (202) & (310) reflections, peak-2 to (112) & (220) reflections and peak-3 to (211) reflection. Their positions, areas and widths were calculated using "peak" command in GENIE program [25], with linearly increasing temperature (unfortunately when this command is used it does not give the errors in the resultant peak parameters). The results were plotted in figure 3.4. From figure 3.4.a we can see that the position of each individual peak apparently does not change significantly with increasing temperature which means that they belong to the very same phase which formed at the start of re-crystallisation and which is found to be  $NiZr_2$ . In fact there is a tiny increase in the position of these peaks with temperature, due to thermal expansion of the cell, which is hardly noticeable by the scale of this figure. Therefore, I have redrawn figure 3.4.a on a bigger scale in figure 3.5, and found that the thermal expansion coefficients to be  $11.58 \times 10^{-6} \text{ }^\circ\text{C}^{-1}$  in the direction of (202) & (310) planes, and  $12.38 \times 10^{-6} \text{ }^\circ\text{C}^{-1}$  in the direction of (112) & (220) planes, and  $13.45 \times 10^{-6} \text{ }^\circ\text{C}^{-1}$  in the direction of (211) plane.

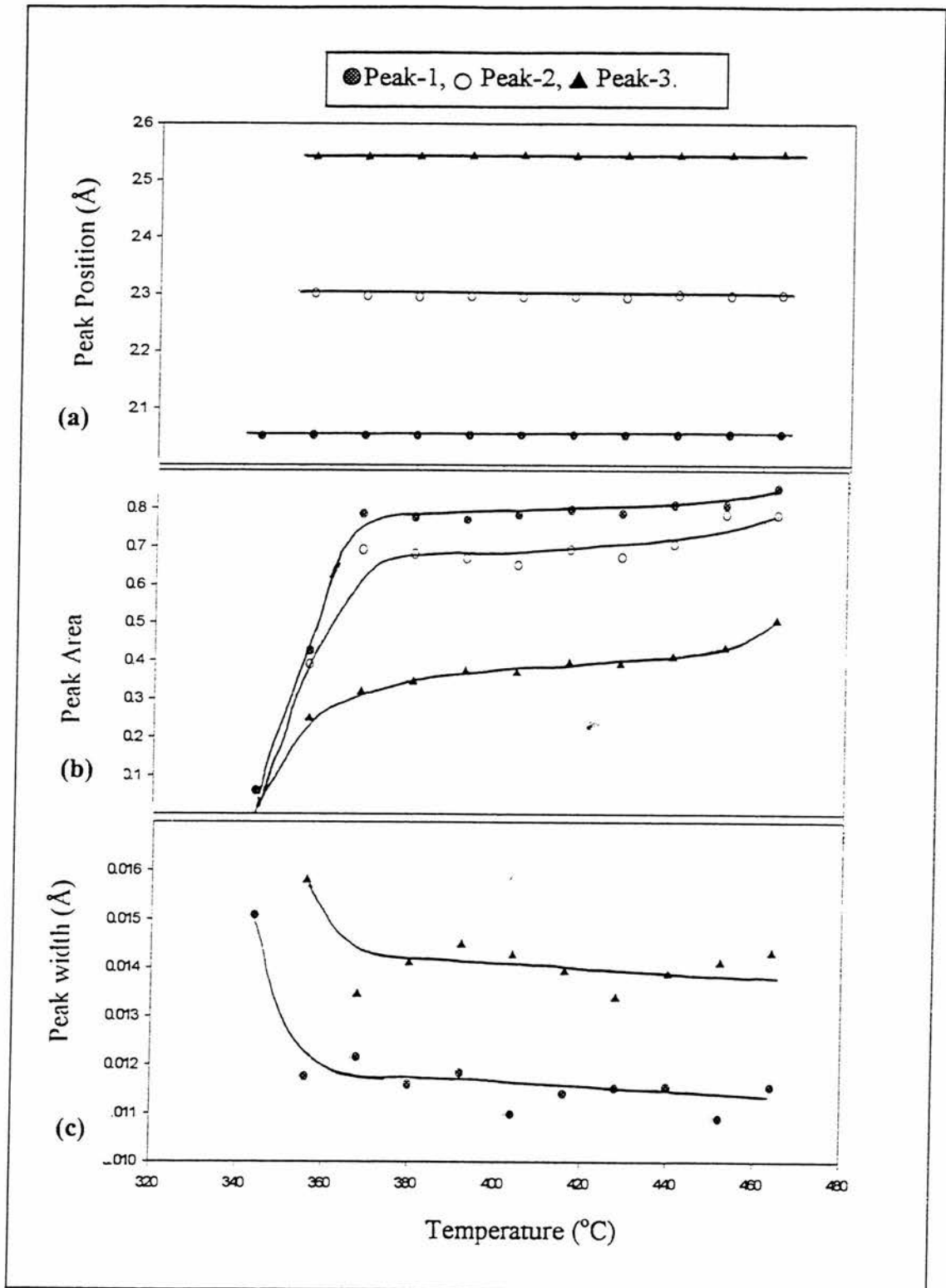


Figure 3.4 Variation of three chosen prominent peak parameters with annealing temperature, from diffraction patterns of  $\alpha\text{-Ni}_{33}\text{Zr}_{67}$  re-crystallisation: a) peaks positions b) peaks areas, c) peaks widths. Peak-1 belongs to 202 & 310 planes; Peak-2 to 112 & 220 planes and peak-3 to 211 planes. The curves drawn through the points added as an aid in viewing the data.

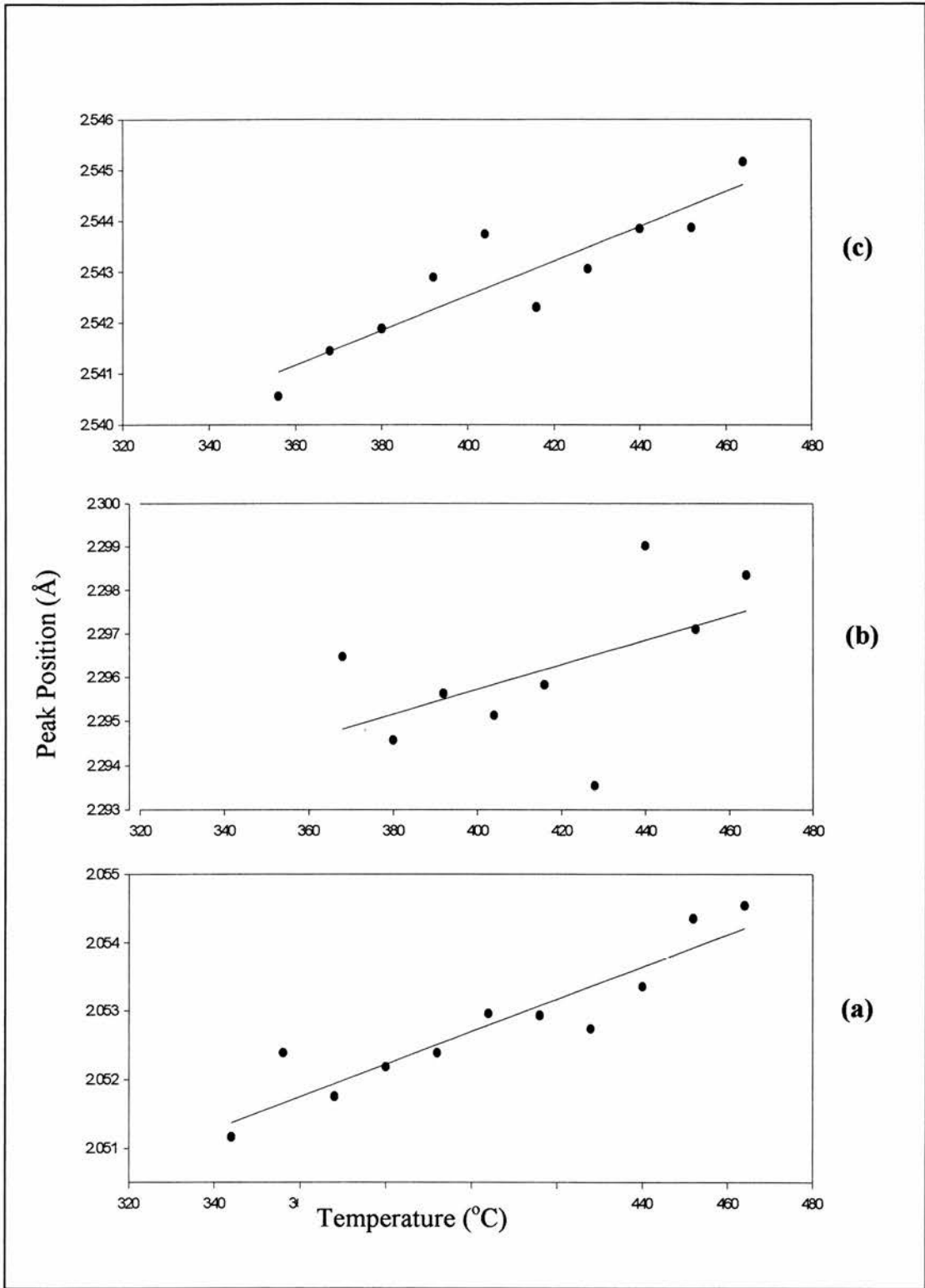


Figure 3.5 Variation of the position of three chosen peaks positions with annealing temperature, from diffraction patterns of  $\alpha$ -Ni<sub>33</sub>Zr<sub>67</sub> recrystallisation. Curves belong to a) (202) & (310), b) (112) & (220) and c) (211) planes.

From figures 3.4.b and 3.4.c, we see that at the beginning of re-crystallisation there is a correlation of wide peaks and small areas and consequently low peak intensities which means the crystallites are quite small and they are at the stage of nucleation or at the stage directly after nucleation. At about 370 °C the increase of the peaks areas and decrease of their widths suddenly slow down which means that the size of the crystallites has almost arrived to maximum and almost the whole sample has crystallised by then. After 370 °C the crystallites grow very slowly until they reach saturation. Another implication of both of these figures is that the sample is single phased, and no other phases are formed or disappeared during the whole annealing process.

The crystal structure of NiZr<sub>2</sub> is plotted in figures 3.6 and 3.7 using Crystallographica program [26], using the lattice parameters I obtained from the neutron diffraction (Table 3.3). The contents of this cell gives a density of 7.14 g.cm<sup>-3</sup> which is less by 1.96 % than the one calculated by Kirkpatrick [16], again this is due to the thermal expansion of the sample at the measurement temperature mentioned above. From figures 3.6 and 3.7, one can see that there are twelve atoms per unit cell, four Ni atoms and eight Zr atoms. Ni atoms are in linear chains, and squares of Zr atoms are positioned at the middle of consecutive Ni atoms in each chain. The consecutive squares are alternately rotated at fixed angles. This structure is discussed in greater detail by Kirkpatrick *et al* [16] and Visnov *et al* [27])

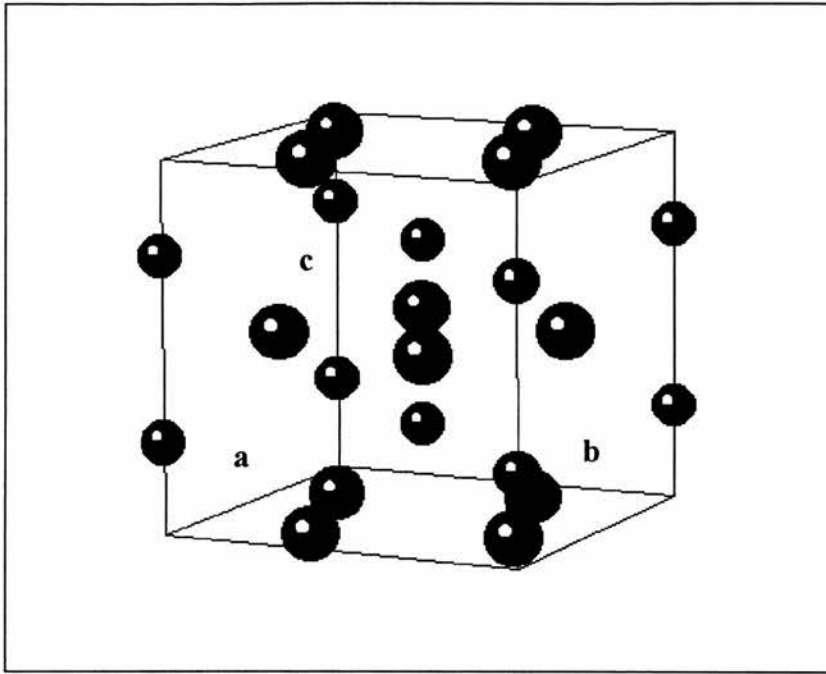


Figure 3.6 The contents of  $\text{NiZr}_2$  bct unit cell; Ni (small circles) and Zr (big circles)

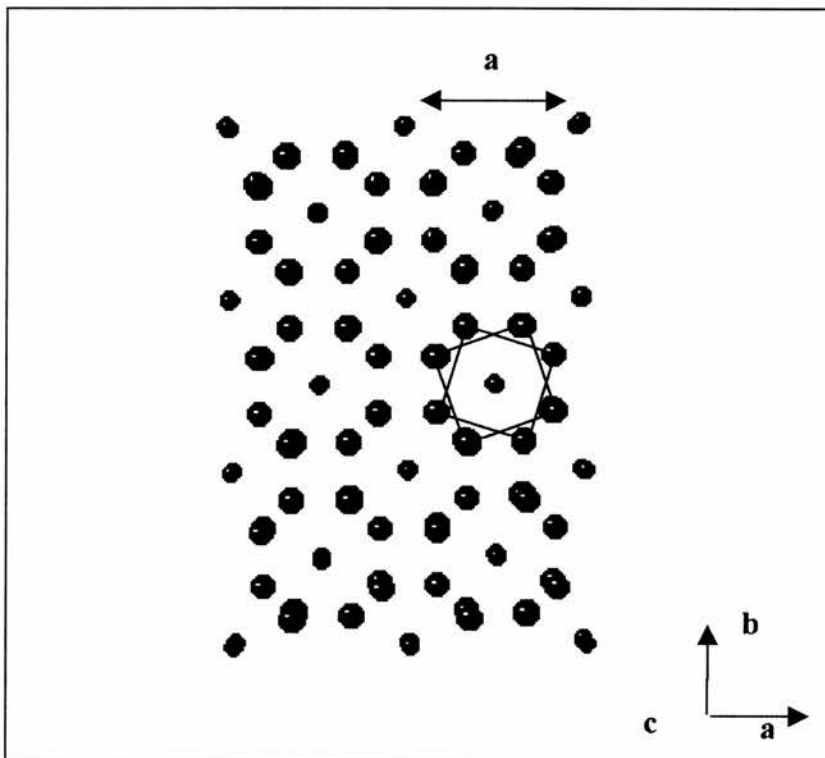


Figure 3.7  $\text{NiZr}_2$  structure; The projection is in the direction of  $c$  axis. Ni atoms are small circles ; Zr atoms are big circles. The unit cell contains twelve atoms, four Ni atoms and eight Zr atoms. Note how the two consecutive Zr squares are twisted around the Ni atoms.

### 3.3 DISCUSSION

In this chapter I have described how crystalline  $\text{NiZr}_2$  is formed by crystallising  $\alpha\text{-Ni}_{33}\text{Zr}_{67}$ . Both DSC and neutron diffraction have shown that the amorphous material directly crystallises into the final phase and no intermediate phases are found.

However, the temperature at which this crystallisation occurs appears to be different depending upon the measurement technique.

From the diffraction data we can see that the re-crystallisation process began at the temperature range of 345-356 °C (see figure 3.2) while in DSC measurements it took place at 392 °C (see figure 3.1), that is about 42 °C later. The explanation of this could be one or a combination of the following reasons:

1. In DSC apparatus there is always a lag of temperature due to the thermal resistance between the sample and the sample holder, besides the amount of this lag is considerably sensitive to heating rates and to encapsulation.
2. The DSC and neutron diffraction measurements were carried out at different heating rates (see Table 3.1). Generally speaking the higher the heating rate the higher the re-crystallisation temperature [9].
3. The temperature calibration of the DSC instrument and the relative accuracy of the DSC thermometry, and that in the neutron furnace.

In figure 3.3, it has been noticed that some of the peaks in the diffraction pattern of the polycrystalline  $\text{NiZr}_2$  were under-fitted and some were over-fitted, indicating the presence of a preferred orientation, which means that the crystallites formed are non-isotropic and the geometrical distribution of these crystallites is non-random. I spent a considerable amount of time using the built-in preferred orientation correction card, "L

PROR" in the Rietveld refinement program [8], which utilises March model after Dollase [28], trying to solve this problem. Unfortunately, I could not get satisfactory results and I was unable to determine the preferred orientation by this method. This leads me to conclude that the geometrical anisotropy of my sample was strong, because the "L PROR" card can only solve small preferred orientations. To solve this problem and determine the preferred orientation of my sample, further analysis is needed, and one can try other computer programs that utilise statistical methods where there is a whole list of them in literature (see for example [29, 30]).

## CHAPTER IV

### CRYSTALLISATION OF $\alpha$ -Dy<sub>7</sub>Fe<sub>3</sub>

#### 4.1 INTRODUCTION

There have been several studies on the crystallisation of  $\alpha$ -RE<sub>7</sub>Fe<sub>3</sub> alloys (RE is rare earth). For example, Tenhover [31] studied the crystallisation of the metallic glass Y<sub>0.66</sub>Fe<sub>0.34</sub> using <sup>57</sup>Fe Mössbauer effect spectroscopy, differential scanning calorimetry, X-ray diffraction and high-temperature resistivity measurements. He found that this alloy crystallises first into the elemental hexagonal Y and then into the C15 Laves cubic YFe<sub>2</sub>. Kilcoyne *et al* also studied the crystallisation of  $\alpha$ -Y<sub>7</sub>Fe<sub>3</sub> using kinetic neutron diffraction [4]. They showed that this alloy crystallises into the elemental hexagonal Y and then into a previously unknown new intermediate intermetallic phase, YFe, which finally transforms into the final C15 Laves cubic phase, YFe<sub>2</sub>, which coexist with the first phase. They also found that the  $\alpha$ -Y<sub>7</sub>Fe<sub>3</sub> precursor is Pauli paramagnetic, the YFe<sub>2</sub> compound is ferromagnetic, while the new YFe compound was found to be occupying an intermediate magnetic state, a weak itinerant electron ferromagnetic with a Curie temperature of 60 K and a magnetic moment of less than 1  $\mu_B$ . Karlsson *et al* [32] recently studied the  $\alpha$ -Dy<sub>7</sub>Fe<sub>3</sub> metallic glass using Reverse Monte Carlo (RMC) technique to obtain a description of the magnetic structure. Their work was based on the assumption that the atomic structure is isomorphous with  $\alpha$ -Dy<sub>7</sub>Ni<sub>3</sub> ( the atomic structure is random close packed [33]) and

they found that the near-neighbour ordering is ferromagnetic, but the spin-spin correlation is strongly oscillatory and there is no strong radial component in the spin-spin correlations and the magnetic ordering temperature was 80 K.

According to the Dy-Fe equilibrium phase diagram shown in figure 2.8 (chapter II), there are four crystalline phases,  $\text{DyFe}_2$ ,  $\text{DyFe}_3$ ,  $\text{Dy}_6\text{Fe}_{23}$ , and  $\text{Dy}_2\text{Fe}_{17}$ . However, there is also a fifth crystalline phase,  $\text{DyFe}_5$ , which is not shown by this diagram, and reported only by Nassau *et al* [34] in 1960. The space groups, cell types, and cell parameters of each of these phases are tabulated in Table 4.1 [23].

Table 4.1 [23].

Crystalline Compound	Space Group	Cell Type	Cell Parameters					
			a (Å)	b (Å)	c (Å)	$\alpha$	$\beta$	$\gamma$
$\text{DyFe}_2$	Fd-3m (227)	Cubic	7.325	7.325	7.325	90	90	90
$\text{DyFe}_3$	R-3m (166)	Hexagonal	5.125	5.125	24.578	90	90	120
$\text{Dy}_6\text{Fe}_{23}$	Fm-3m (225)	Cubic	12.055	12.055	12.055	90	90	90
$\text{Dy}_2\text{Fe}_{17}$	P63/mmc (194)	Hexagonal	8.473	8.473	8.284	90	90	120
$\text{DyFe}_5$	P6/mmm (191)	Hexagonal	4.900	4.900	4.100	90	90	120

In this chapter I will present the results of the crystallisation of  $\alpha\text{-Dy}_7\text{Fe}_3$ , the composition corresponding to the lowest eutectic in the system (see figure 2.8 in chapter II), by using the same techniques used in chapter III, i.e. DSC and kinetic neutron diffraction. I will also present the results of the DSC measurements carried out on amorphous  $\text{Y}_7\text{Fe}_3$  and  $\text{Er}_7\text{Fe}_3$  samples, in a dynamic mode, and compare them with the neutron diffraction measurements carried out by Kilcoyne and Manuel on the same materials [4, 5, 24, 35]. From these measurements I hope to get a better picture and understanding of the crystallisation of amorphous  $\text{RE}_7\text{Fe}_3$  alloys in general and  $\text{Dy}_7\text{Fe}_3$  in particular.

## 4.2 RESULTS

### 4.2.1 DSC

The DSC measurements were carried out using Perkin-Elmer DSC7 differential scanning calorimetry, which is described in detail in the appendix, section (A.5.1), and briefly described below.

First, two empty sample capsules were placed into the instrument and heated linearly at 10 °C/min, over the temperature range 50-450 °C. From this measurement the baseline, which represents the background, was obtained. One of the empty capsules was then removed and replaced by a capsule containing a sample of  $\alpha$ -Dy<sub>7</sub>Fe<sub>3</sub>. The measurement was repeated under the same thermal conditions, and the heat flow vs. temperature curve was obtained, with the base line subtracted. The parameters of this experiment are tabulated in Table 4.2; and the final curve is shown in figure 4.1

From figure 4.1, it is clear that two reactions have occurred. The first, an exothermic reaction, occurs at ~280 °C and the second one, also an exothermic reaction, at ~386 °C. By comparing this curve with those obtained from  $\alpha$ -Y<sub>7</sub>Fe<sub>3</sub> and  $\alpha$ -Er<sub>7</sub>Fe<sub>3</sub>, together with the kinetic neutron diffraction patterns collected from  $\alpha$ -Y<sub>7</sub>Fe<sub>3</sub> [4, 24, 35] and  $\alpha$ -Er<sub>7</sub>Fe<sub>3</sub> [5] it might be expected that these two reactions are (i) the primary crystallisation into the hcp elemental Dy and (ii) the eutectic crystallisation of the residual amorphous phase into the previous phase and the C15 laves phase compound DyFe<sub>2</sub>, but this will be confirmed later from the POLARIS measurements.

It should also be noted that there is an endothermic peak at ~314 °C. This will be discussed later in detail.

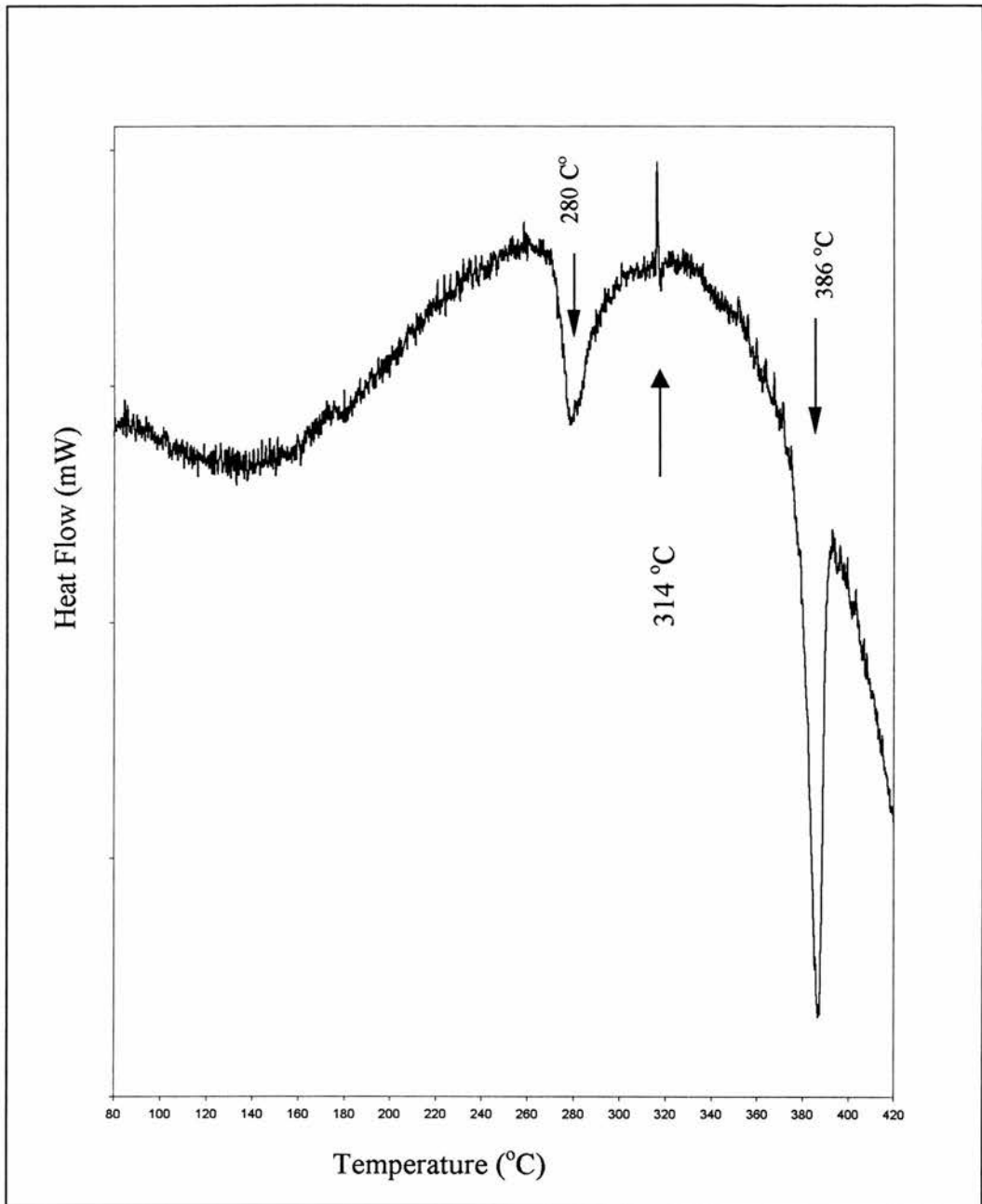


*Figure 4.1 Heat flow curve vs. temperature for  $\alpha$ -Dy<sub>7</sub>Fe<sub>3</sub> taken by DSC7 at a scanning rate of 10 °C/min with base line subtracted. The arrows show the temperatures of the two exothermic dips, 280 and 386 °C. The upward arrow shows the temperature of the endothermic spike, 314 °C.*

## 4.2.2 NEUTRON DIFFRACTION ON POLARIS

3.16 g of amorphous  $\text{Dy}_7\text{Fe}_3$  ribbon was loaded into a vanadium can, and mounted in the RALF1 furnace. The sample was then heated from room temperature to 408 °C at a constant heat ramp of 0.67 °C/min. Diffraction spectra were collected continuously every 6 minutes. Details of the sample used and the parameters of this experiment are given in Table 4.2. Refinements of the final diffraction spectrum from the recrystallisation products were carried out using the CCSL Rietveld refinement program [8].

Table 4.2

<i>The amorphous sample</i>	<b>DSC</b>			<b>POLARIS</b>			
	<i>Weight (mg)</i>	<i>Heating rate (°C/min)</i>	<i>Temperature range (°C)</i>	<i>Weight (g)</i>	<i>Heating rate (°C/min)</i>	<i>Temperature range (°C)</i>	<i>Counting Time for each run (min)</i>
$\text{Dy}_7\text{Fe}_3$	~50	10	50-450	3.16	0.67	RT- 408	6

Figure 4.2 shows the diffraction patterns of crystallisation of amorphous  $\text{Dy}_7\text{Fe}_3$ , collected at temperatures indicated. The material remains amorphous up to ~252 °C, it then begins to crystallise at ~256 °C. A comparison of these patterns with increasing temperature shows the phase that first forms, continues to exist at all subsequent temperatures. However new peaks begin to appear at ~337 °C indicating the crystallisation of a second phase which co-exists with the first phase at all subsequent temperatures. Figure 4.3, which shows two diffraction patterns at the d-spacing between 2 and 3 Å, shows the two phases more clearly in the diffraction patterns. The lower pattern is the sum of runs at temperatures between 263-335 °C, and it shows clearly the Bragg peaks belonging to the first phase. The upper pattern is the sum of runs at temperatures between 339-408 °C, and it shows how the second phase Bragg peaks (pointed out by arrows) are added to the pattern.

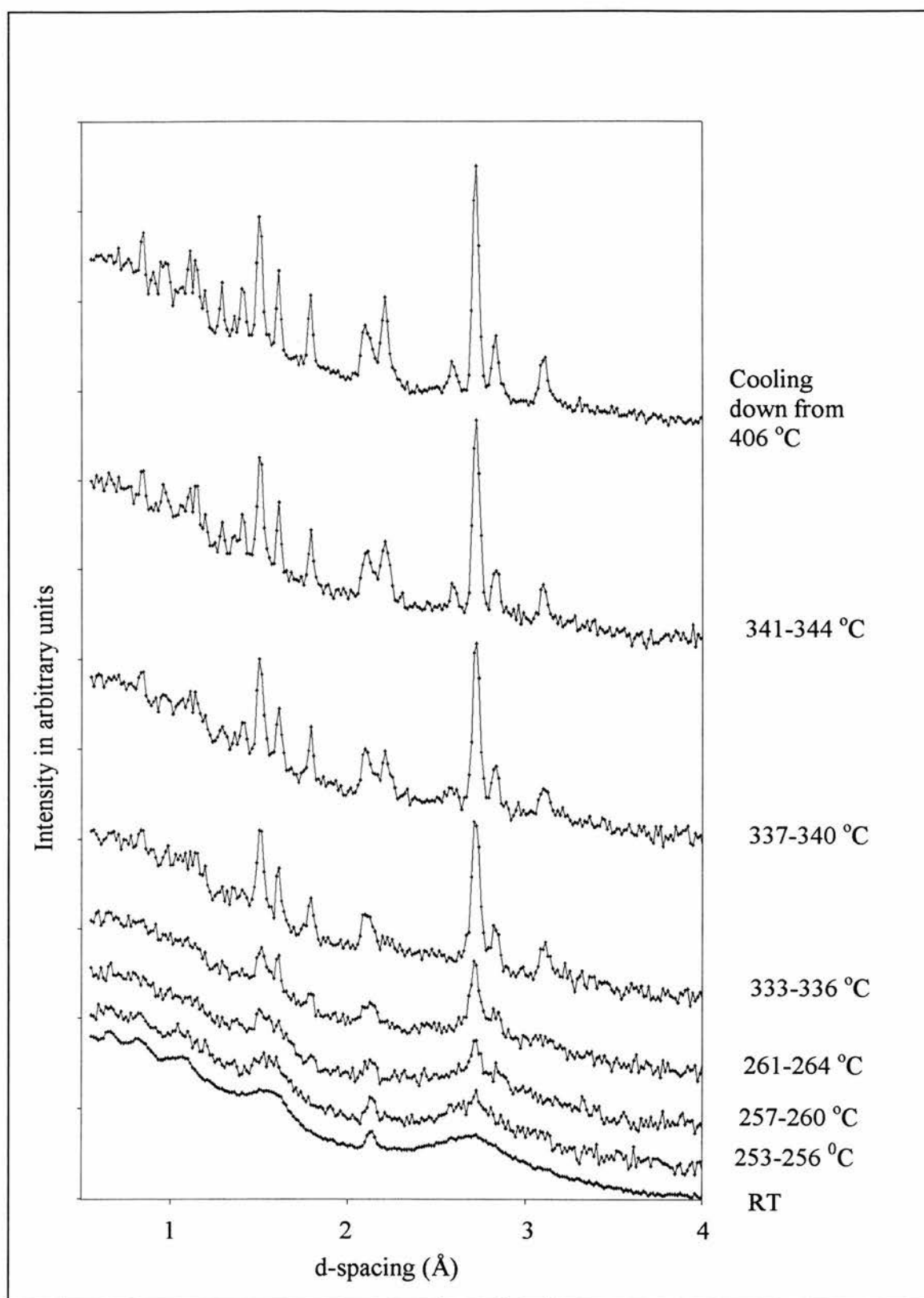
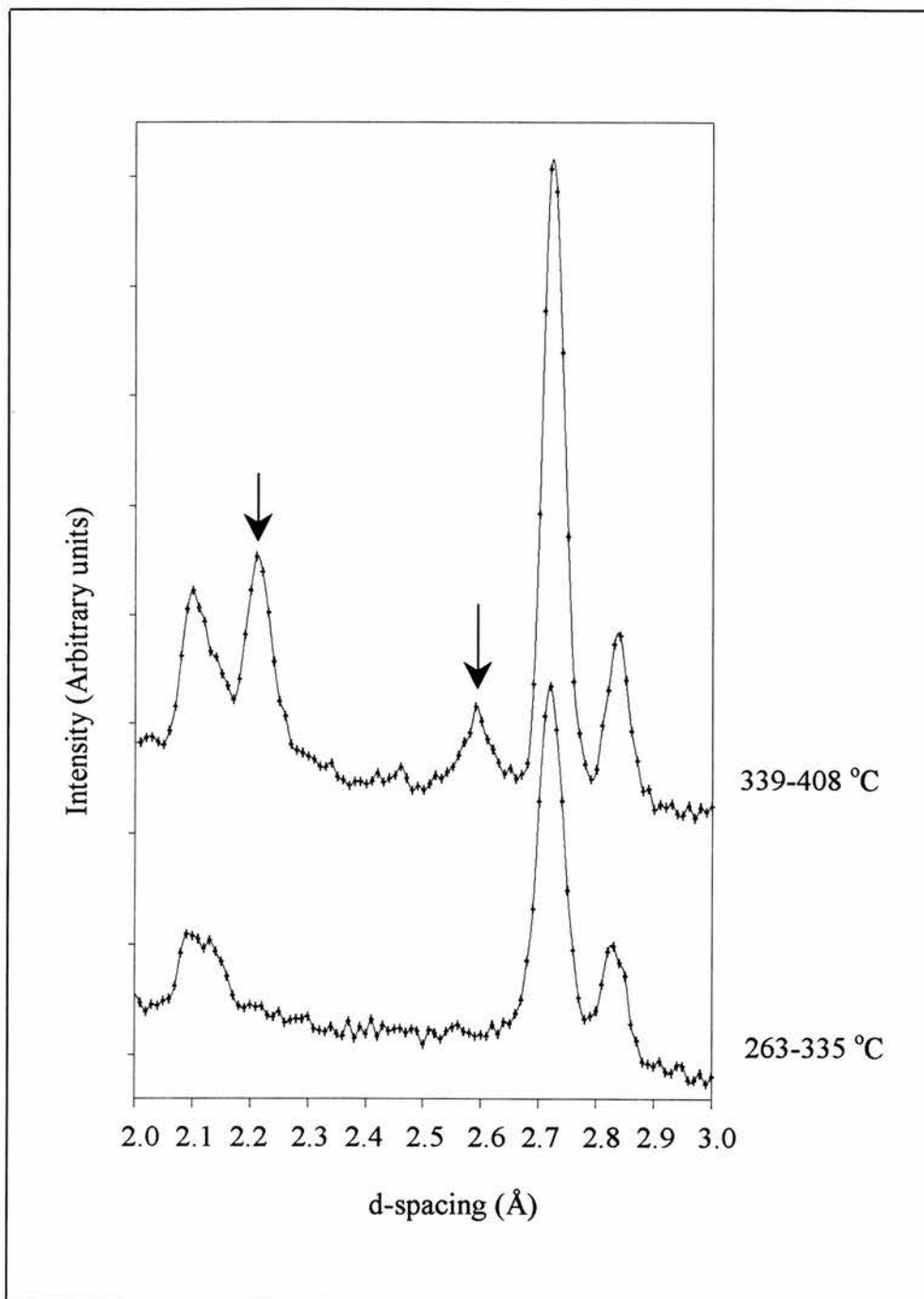


Figure 4.2 Diffraction patterns of re-crystallisation of  $\alpha\text{-Dy}_7\text{Fe}_3$  taken at POLARIS at different temperatures.



*Figure 4.3 Two diffraction patterns at d-spacing between 2 and 3 ( $\text{\AA}$ ) of re-crystallisation of  $\alpha\text{-Dy}_7\text{Fe}_3$ . The lower pattern shows the peaks evolved at the temperature range 263-335 °C; While the upper pattern shows how the new peaks (indicated by arrows) have been evolved in the successive temperature range 339-408 °C.*

A two-phase Rietveld refinement (Dy+DyFe<sub>2</sub>) was carried out for the diffraction pattern of the final product, which was collected while it was cooling down from 406 °C. The data and the fit are shown in figure 4.4. The Dy crystallises with a hexagonal unit cell, space group P6<sub>3</sub>/mmc, and the DyFe<sub>2</sub> crystallises in the C15 cubic laves phase structure, space group Fd $\bar{3}$ m. The starting parameters for Dy and DyFe<sub>2</sub> were taken from the CDS [23]. The details of these structures are given in Table 4.3. The Chi-squared of the best fit was 0.7917. The parameters of the correspondent fit are displayed in Table 4.4, and are in extremely good agreement with those displayed in Table 4.3. The resultant cell dimensions for the hexagonal Dy was ( $a = 3.60 \pm 0.06$  Å and  $c = 5.696 \pm 0.001$  Å), and the volume of the unit cell was  $64 \pm 2$  Å<sup>3</sup>. The cell dimensions for the cubic DyFe<sub>2</sub> ( $a = 7.375 \pm 0.002$  Å), and the volume of the unit cell was  $401.1 \pm 0.3$  Å<sup>3</sup>. It is clear, as was the case in the NiZr<sub>2</sub> study (chapter III), that these cell dimensions are bigger than the ones listed in literature (Table 4.3) because of the thermal expansion at higher temperatures. The isotropic temperature factors for the Dy atoms in the hexagonal Dy crystal was found to be  $0.59448$  Å<sup>2</sup>, while for the Dy and Fe atoms in the cubic DyFe<sub>2</sub> crystal were fixed at  $0.8$  Å<sup>2</sup> for each atom. When these parameters were allowed to vary in the refinement process, they took very low values and even negative values with no real improvement in the fitting of the diffraction data. The inability to fit the isotropic temperature factor is a result of poor counting statistics and high background counts. It should be noted that the crystalline Dy phase exists over the temperature range (253-408 °C) while the crystalline phase DyFe<sub>2</sub> only exists over the temperature range (330-408 °C); and these two phases do not transform once they have formed.

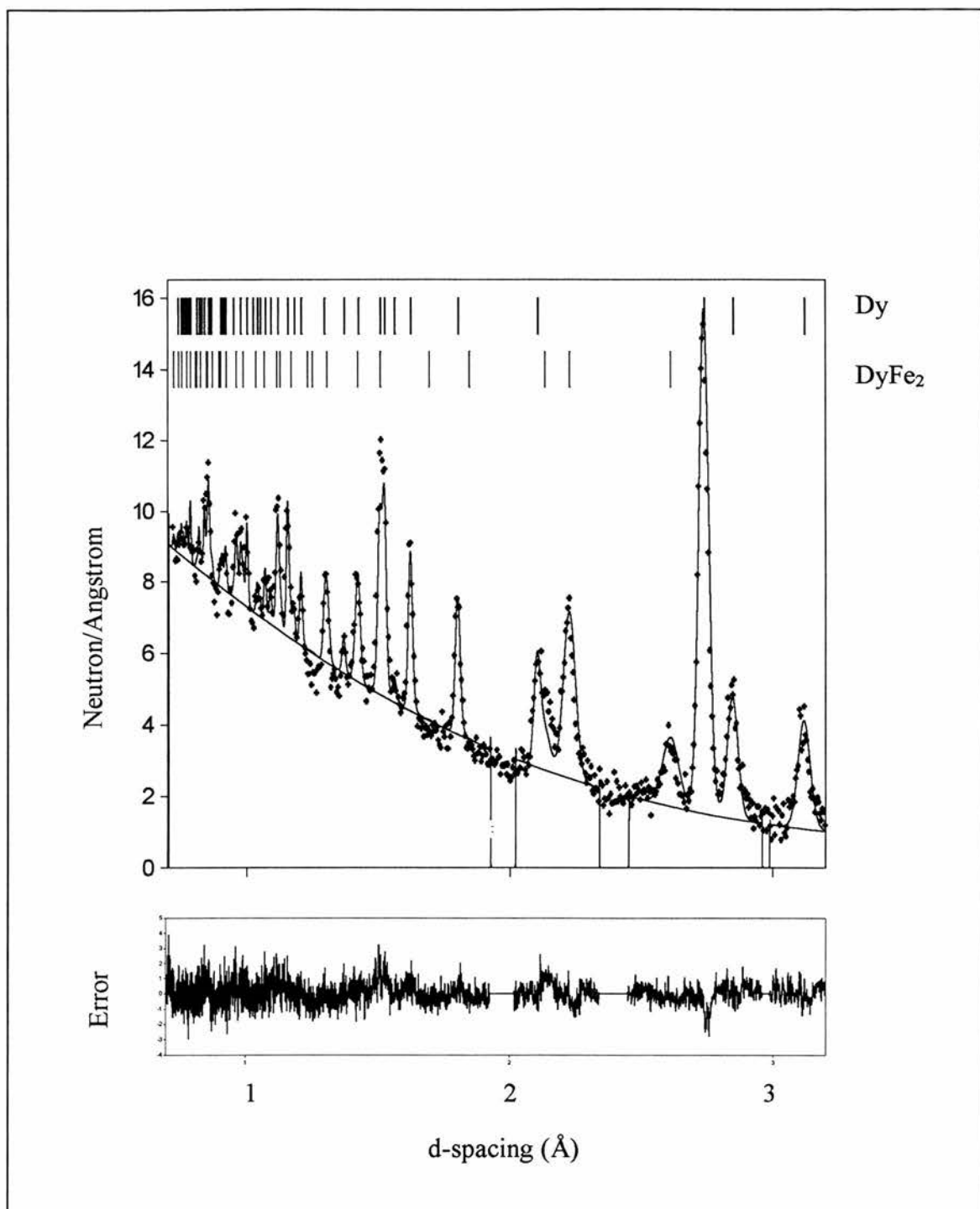


Figure 4-4 A diffraction pattern for re-crystallised  $\alpha$ -Dy<sub>7</sub>Fe<sub>3</sub> taken while it was cooling down from 406 °C. The data (cross) is fitted by the elemental Dy and DyFe<sub>2</sub> compound models (solid line) using CCSL Rietveld refinement program. The upper vertical lines are the peak positions of Dy, and the lower ones are of DyFe<sub>2</sub>. The lower figure is the difference between the measured data and the fit.

Table 4.3 The starting parameters for Dy and DyFe<sub>2</sub> as published in CDS [23].

<b>Formula</b> Dy						
<b>Cell Data</b>						
-----						
Dimensions (Å)		3.5903(1)	3.5903(1)	5.6475(2)		
Angles (deg)		90.000(-)	90.000(-)	120.000(-)		
Volume(Å <sup>3</sup> )		63.045				
Z-Value		2.00				
Space Group Code		P63/mmc				
Space Group No.		194				
Number of Atoms		1				
<b>Atomic Parameters</b>						
-----						
Atom	Wyckoff	Occup.	x	y	z	
Dy	2c -6m2	1.00	0.3333	0.6667	0.2500	
<b>Formula</b> DyFe <sub>2</sub>						
<b>Cell Data</b>						
-----						
Dimensions (Å)		7.3250(-)	7.3250(-)	7.3250(-)		
Angles (deg.)		90.000(-)	90.000(-)	90.000(-)		
Volume (Å <sup>3</sup> )		393.025				
Z-Value		8.00				
Space Group Code		Fd -3m				
Space Group No.		227				
Number of Atoms		2				
<b>Atomic Parameters</b>						
-----						
Atom	Wyckoff	Occup.	x	y	z	
Dy	8a -43m	1.00	0.0000	0.0000	0.0000	
Fe	16d -3m	1.00	0.6250	0.6250	0.6250	

Table 4.4 The final parameters for Dy and DyFe<sub>2</sub> obtained by the Rietveld refinements.

<b>Formula Dy</b>					
Chi-squared of the fit					0.7917
Isotropic temperature factor of Dy (Å <sup>2</sup> )					0.59448
<b>Cell Data</b>					
-----					
Dimensions (Å)	3.60(6)	3.60 (6)	5.696(1)		
Angles (deg)	90.000(-)	90.000(-)	120(-)		
Volume(Å <sup>3</sup> )		64(2)			
Space Group Code		P63/mmc			
Space Group No.		194			
Weighted Profile R <sub>obs</sub> factor		12.85			
Expected R <sub>obs</sub> factor		14.44			
Number of Atoms		1			
<b>Atomic Parameters</b>					
-----					
Atom	Wyckoff	Occup.	x	y	z
Dy	2c -6m2	1.00	0.3333	0.6667	0.2500

<b>Formula DyFe2</b>					
Chi-squared of the fit					0.7917
Isotropic temperature factors (Å <sup>2</sup> )					
Dy				0.8	
Fe				0.8	
<b>Cell Data</b>					
-----					
Dimensions (Å)	7.375(2)	7.375(2)	7.375(2)		
Angles (deg.)	90.000(-)	90.000(-)	90.000(-)		
Volume (Å <sup>3</sup> )		401.1(3)			
Space Group Code		Fd -3m			
Space Group No.		227			
Weighted Profile R <sub>obs</sub> factor		12.85			
Expected R <sub>obs</sub> factor		14.44			
Number of Atoms		2			
<b>Atomic Parameters</b>					
-----					
Atom	Wyckoff	Occup.	x	y	z
Dy	8a -43m	1.00	0.0000	0.0000	0.0000
Fe	16d -3m	1.00	0.6250	0.6250	0.6250

I have examined the Dy and DyFe<sub>2</sub> phases, formed during the annealing process, in more detail selecting peak (101) for Dy, and peak (311) for DyFe<sub>2</sub>. Their positions, areas and widths were calculated using "peak" command in GENIE program [25] with linearly increasing temperature (unfortunately when this command is used it does not give the errors in the resultant peak parameters). The results are plotted in figures 4.5, 4.6, and 4.7.

From figure 4.5 we can see that the position of both peaks is apparently changing very little with the increasing temperature due to the thermal expansion of the crystals. In fact, the Dy (101) d-spacing is increasing linearly with the temperature at a rate of  $4.06 \times 10^{-5} \text{ \AA}/^\circ\text{C}$ , and the thermal expansion coefficient in the direction of (101) plane is found to be  $14.96 \times 10^{-6} \text{ }^\circ\text{C}^{-1}$ . The DyFe<sub>2</sub> (311) d-spacing is increasing at a rate of  $2.37 \times 10^{-5} \text{ \AA}/^\circ\text{C}$ , and the thermal expansion coefficient in the direction of (311) plane is found to be  $10.73 \times 10^{-6} \text{ }^\circ\text{C}^{-1}$ . Figure 4.6 shows the variation of peaks areas with increasing temperature. The upper curve belongs to Dy (101) reflection. The area begins to increase sharply from about 256 C°, and it flattens over the temperature range 270-300 °C. Then for the second time, it starts to increase over 300-310 °C and to flatten over 310-330 °C. Then for the third and last time, it starts to increase over 330-340 °C and to flatten over 340-408 °C. The lower curve belongs to DyFe<sub>2</sub> (311) reflection and it begins at about 330 °C and flattens very quickly over 340-408 °C. The behaviour of these two curves can have some interesting implications. When we look at the Dy curve we see that it had three consecutive plateaux. The presence of Dy curve alone in the lower temperature range, 256-300 °C, means that the amorphous alloy first primarily crystallises into the hcp elemental Dy until the first plateau is reached at ~270 °C where the growth of Dy crystallites slows down sharply, leaving behind an Fe-rich amorphous alloy. The formation of the last Dy plateau coincides

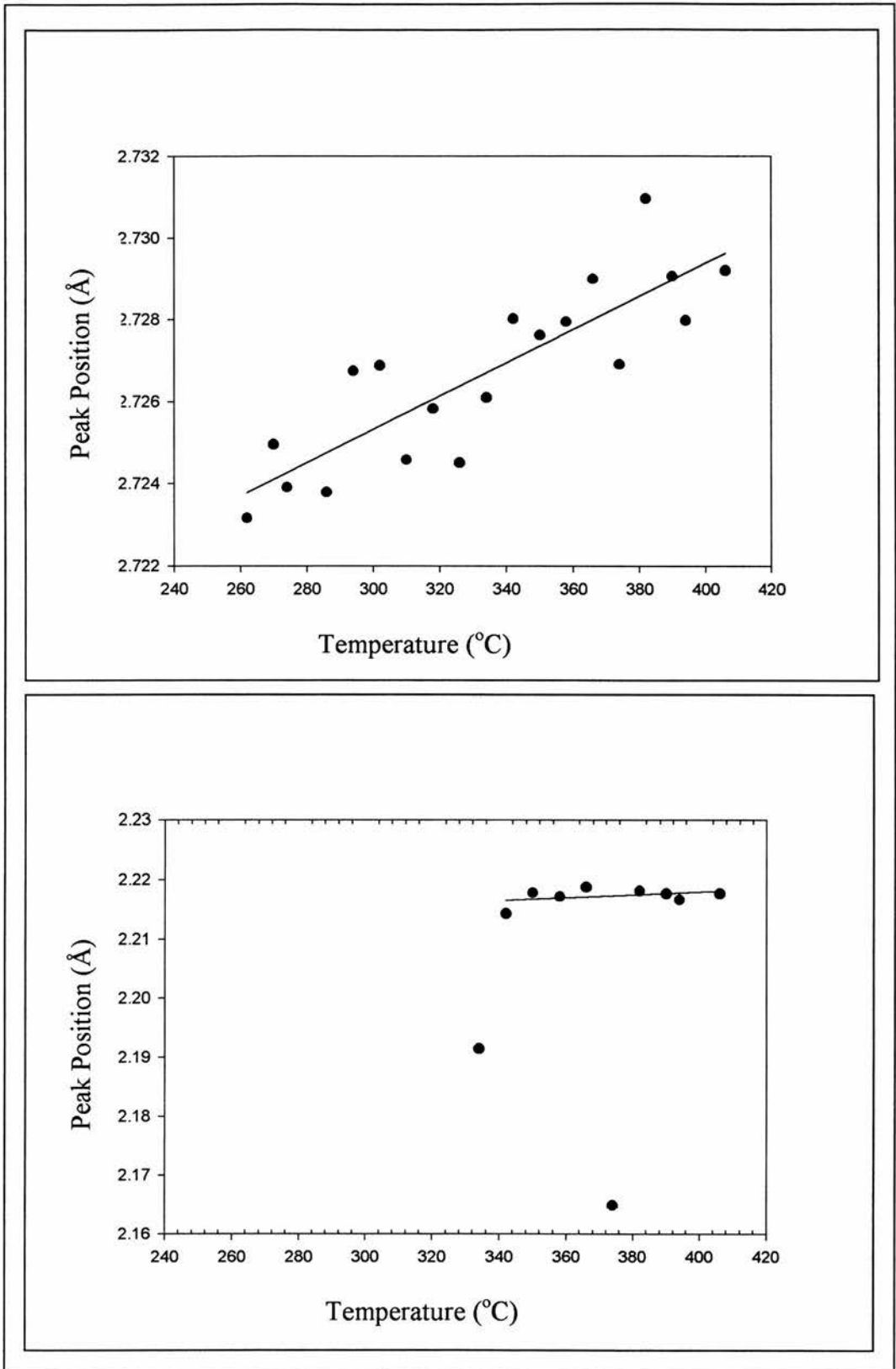


Figure 4.5 Variation of the peak position with temperature for Dy (101) peak (the upper figure) and DyFe<sub>2</sub> (311) peak (the lower figure).

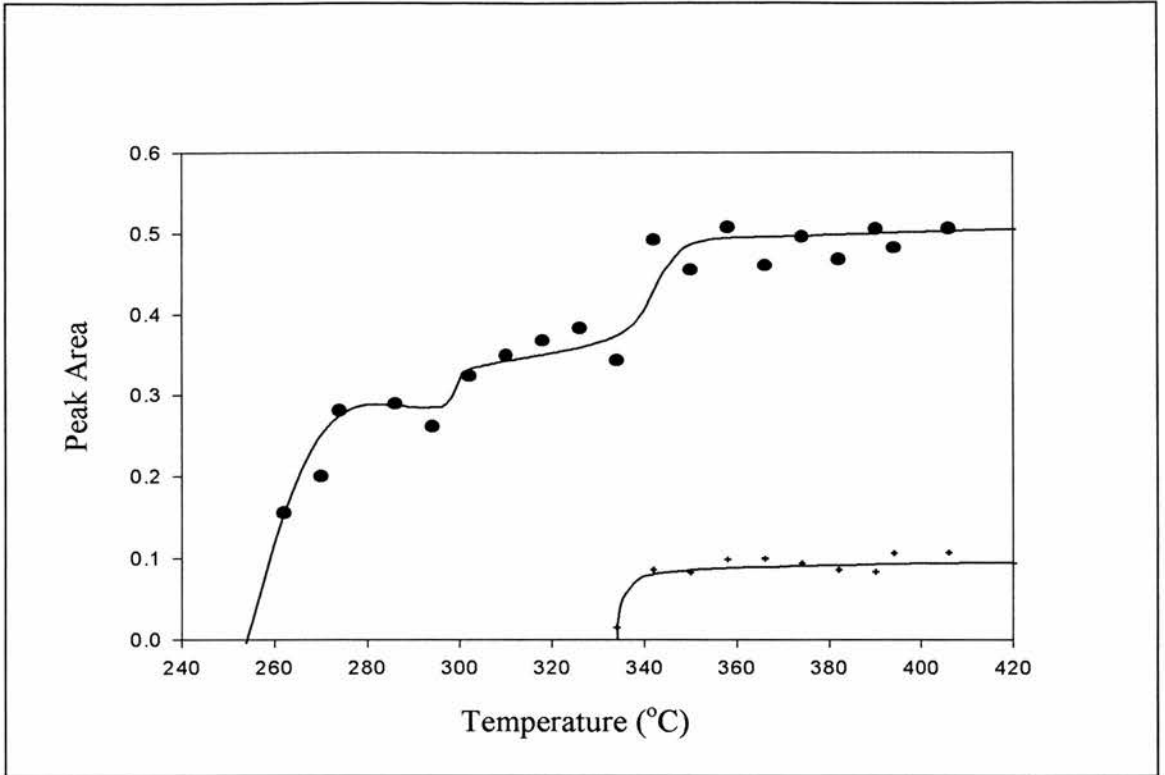


Figure 4.6 Variation of the peak area with temperature for Dy (101) peak (the upper curve) and DyFe<sub>2</sub> (311) peak (the lower curve). The curves drawn through the points were added as an aid in viewing the data.

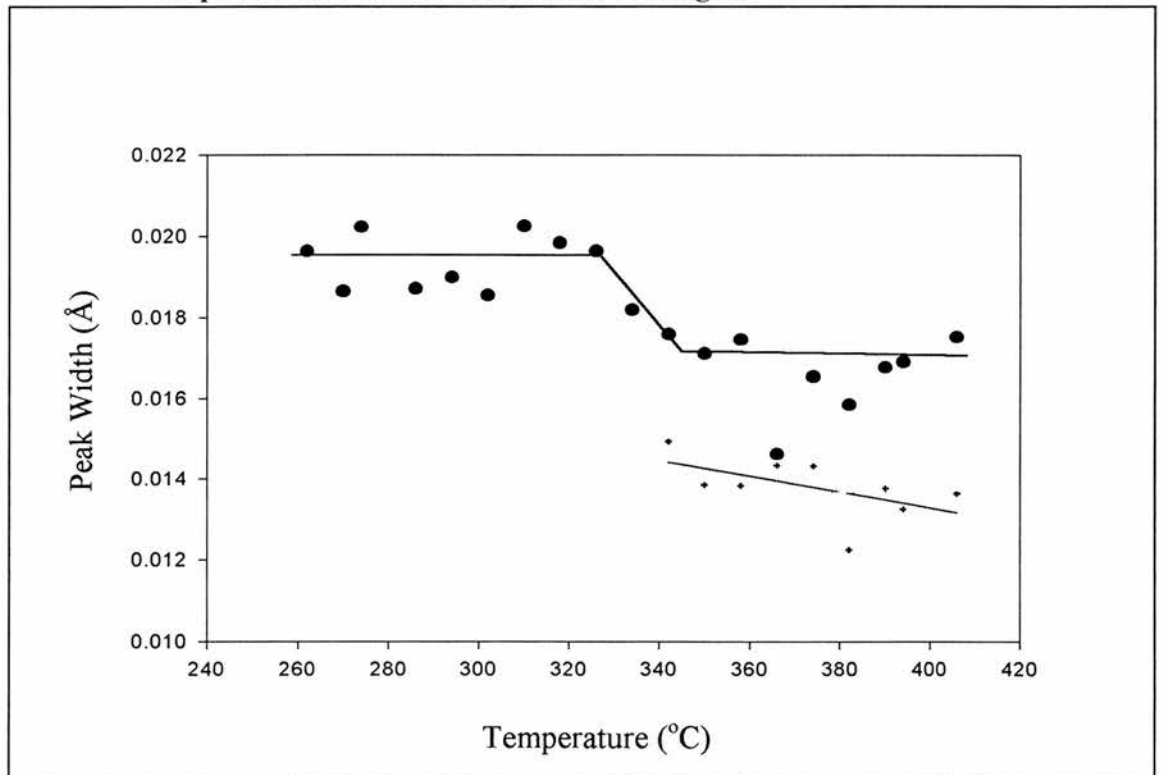
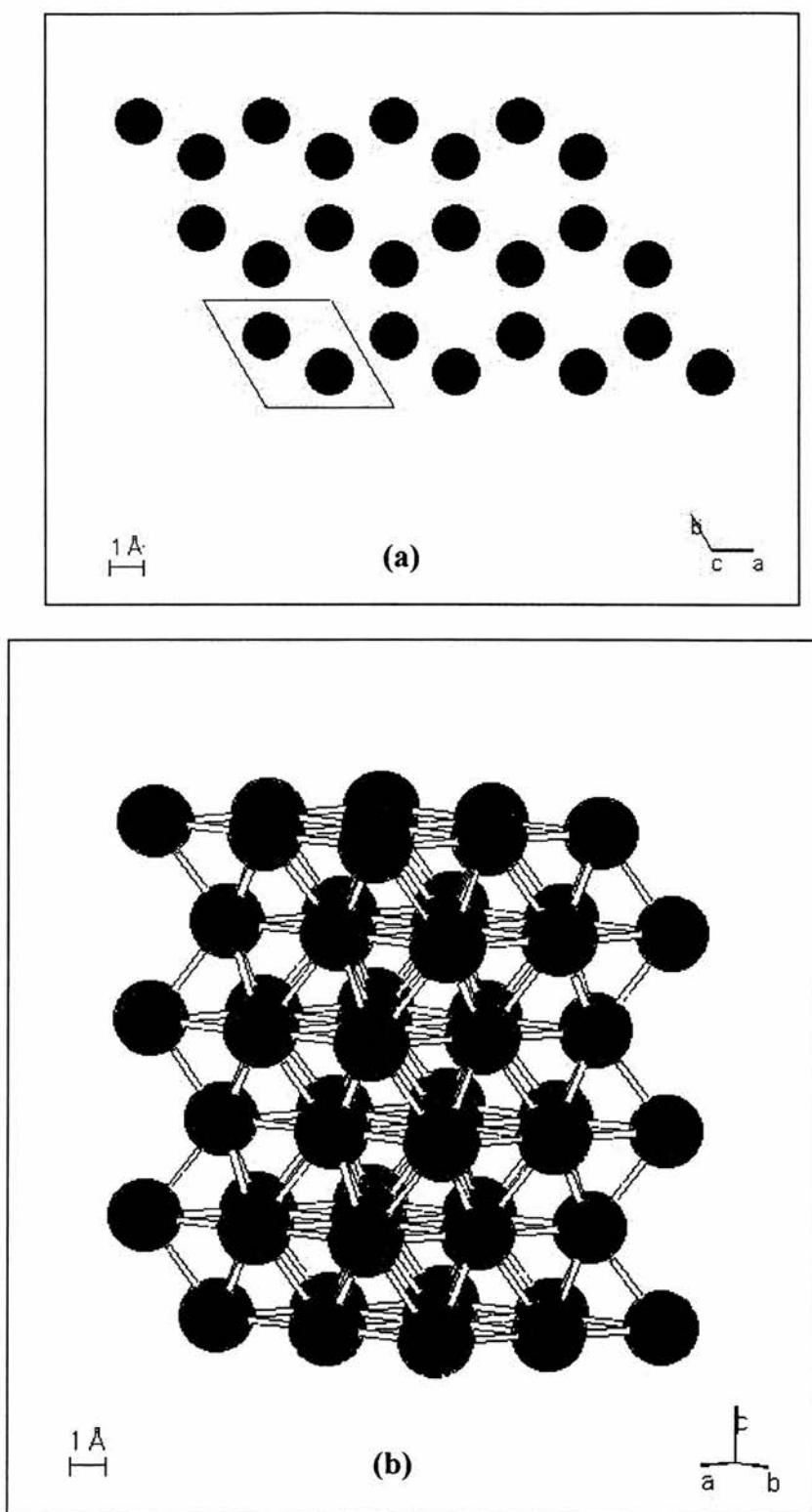


Figure 4.7 Variation of the peak width with temperature for Dy (101) peak (the upper curve) and DyFe<sub>2</sub> (311) peak (the lower curve). The curves drawn through the points were added as an aid in viewing the data.

with the appearance of the  $\text{DyFe}_2$  phase, the lower curve. This means that the residual Fe-rich amorphous alloy crystallises eutectically over the temperature range 330-340 °C into the hcp elemental Dy and the C15 cubic laves phase  $\text{DyFe}_2$ . The growth of these two phases almost stops after ~340 °C where the last plateaux begin to appear. Could we deduce then that the formation of the middle plateau is an indication to the co-existence of some unnoticed phase? Similar behaviours were reported by Manuel *et al* [4, 24, and 35] in their studies of the crystallisation of amorphous  $\text{Y}_7\text{Fe}_3$  where they found that the crystallisation proceeds at about 300 °C via an initial crystallisation of Y into an hcp structure and at about 390 °C a new intermediate phase begins to appear with a stoichiometric YFe composition, a hexagonal space group  $\text{P6}_3/\text{mmc}$ , and extraordinarily large cell dimensions,  $a=12.90 \text{ \AA}$  and  $c=11.71 \text{ \AA}$ . This new phase co-exists with the previous phase to 450 °C, then transformed into the final cubic C15 Laves phase  $\text{YFe}_2$ . The elemental hcp Y was found to form disc-shaped nano-crystallites with radii of ~300 Å and thickness of ~30 Å [24]. They also reported similar behaviour in the crystallisation of the amorphous  $\text{Er}_7\text{Fe}_3$  [5]. Therefore, a previously unknown intermediate phase might be expected to form between the two phases, Dy and  $\text{DyFe}_2$ , between ~300 and ~330 °C, and is predicted to be a new compound,  $\text{DyFe}$ . Unfortunately the long counting time required to obtain a spectrum on POLARIS meant that this phase could not be seen in these diffraction patterns, figure 4.2. However, there is some weak indication that this might be the case. When we look at the DSC curve of the crystallisation of the  $\alpha\text{-Dy}_7\text{Fe}_3$ , figure 4.1, we notice the existence of a very narrow sharp endothermic peak at ~314 °C which might be a spurious spike but this is unlikely because its appearance at the expected temperature. From figure 4.7 we see that the Dy peak width, (upper curve), has step like behaviour with an upper plateau from about 256 °C to about 330 °C, then the width drops steeply

and a lower plateau begins at around 340 °C. This continues to the final temperature, 408 °C. We also notice that the second plateau of the Dy and the very slowly decreasing DyFe<sub>2</sub> curve (the lower curve) begin at the same temperature, ~340 °C. When we compare this figure, figure 4.7, with figure 4.6 we see that there is an inverse relation between the areas of peaks and their widths with increasing temperature. This behaviour is typical of the crystal growth, beginning with nucleation, the stage directly after nucleation and the following growth of crystallites sizes. We see from figure 4.7 the extent of Dy upper plateau covers the same temperature range of the first two successive plateaux of Dy curve in figure 4.6 *i.e.* 256-330 °C. The extent of Dy lower plateau covers the same temperature range of the final plateau of Dy curve in figure 4.6, *i.e.* 340-408 °C. This shows that the Dy crystallites are small and growing until they reach a limit when they can grow no further and all crystallites compact with each other.

The crystal structure of the elemental Dy is plotted in figure 4.8, and that of DyFe<sub>2</sub> in figure 4.9 using Crystallographica program [26], using the lattice parameters obtained from the best fit to the neutron diffraction pattern (Table 4.4). The contents of hexagonal Dy cell gives a density of 8.42407 g.cm<sup>-3</sup> and that of cubic DyFe<sub>2</sub> gives a density of 9.08054 g.cm<sup>-3</sup>. which is less by 0.21 % than the one calculated by Deodhar *et al* [36], this is again due to the thermal expansion of the sample at the measurement temperature mentioned above. From figure 4.8 one can see that there are two atoms per unit cell. From figure 4.9 we see that the unit cell of cubic DyFe<sub>2</sub> has twenty four atoms, eight Dy atoms and sixteen Fe atoms. Both atoms are arranged in linear chains.



*Figure 4.8 The hexagonal structure. of the elemental Dy The unit cell contains two atoms. a) a projection in the direction of the  $c$  axis; b) The spatial distribution of the atoms in the hexagonal structure.*

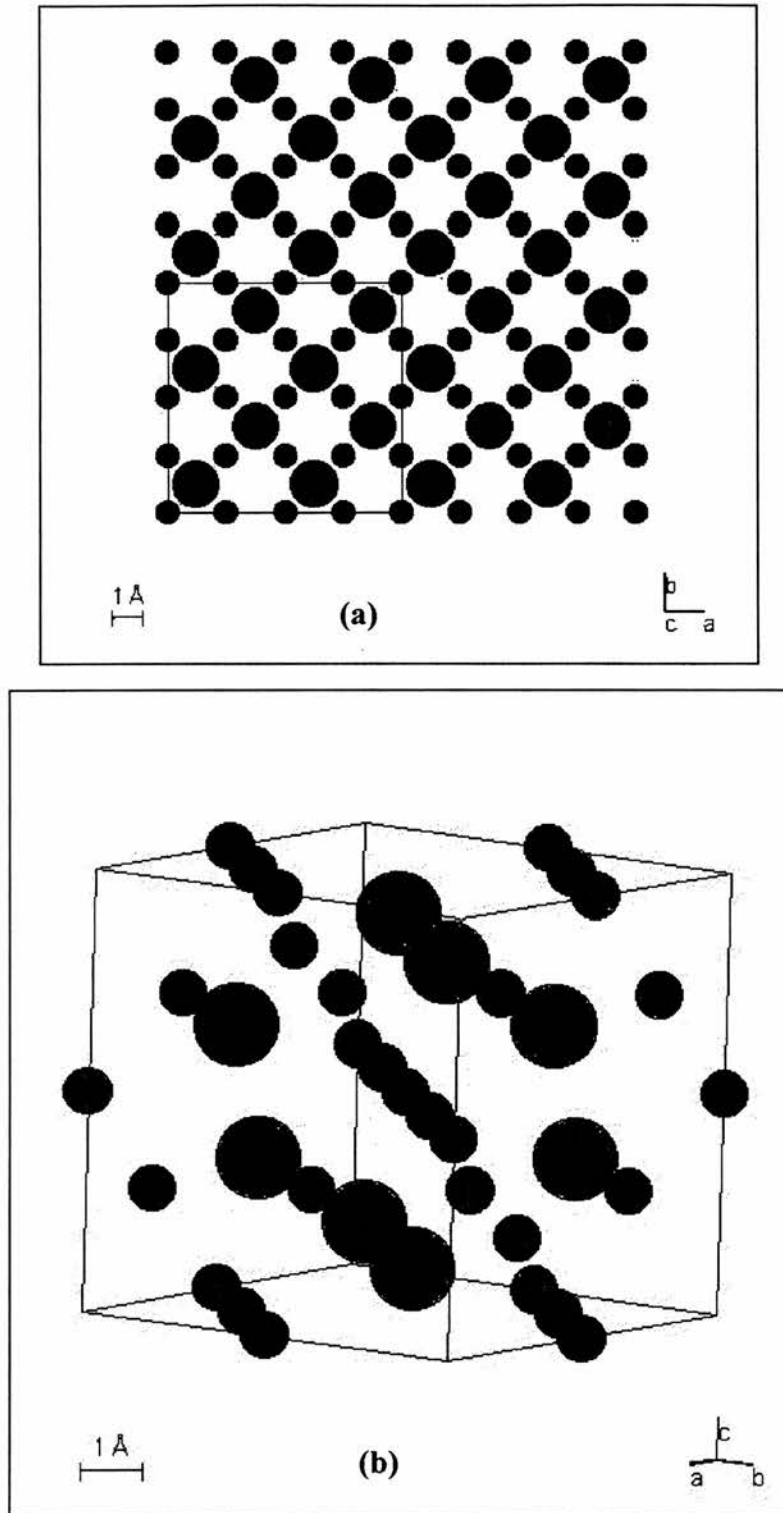


Figure 4.9 The C15 cubic laves phase structure of the DyFe<sub>2</sub> compound. The unit cell contains twenty four atoms ( big circles), eight Dy atoms and sixteen Fe atoms (small circles). Fig. (a) is the projection of the crystal in c direction, and Fig (b) is the cubic unit cell.

### 4.3 DISCUSSION

In this chapter I have presented the results of a study of the crystallisation of  $\alpha$ -Dy<sub>7</sub>Fe<sub>3</sub>. I have shown that two crystalline phases appear as the temperature increases: First the elemental hexagonal Dy then the cubical C15 Laves phase DyFe<sub>2</sub> compound. I have also discussed the possibility of the existence of a new intermediate third phase from the peak at ~314 °C on the DSC curve (figure 4.1), although the phase could not be seen in the neutron diffraction patterns, possibly that this new intermediate phase is short-lived similar to the intermediate YFe phase, so it might not be there in the POLARIS diffraction pattern, appearing and then quickly disappearing so we do not see a good Bragg peak indicative of this new phase. There have been previous studies on the crystallisation of  $\alpha$ -RE<sub>7</sub>Fe<sub>3</sub> (RE is rare earth), for example in 1981 Tenhover [31] studied the crystallisation of the metallic glass Y<sub>0.66</sub>Fe<sub>0.34</sub> using <sup>57</sup>Fe Mössbauer effect spectroscopy, differential scanning calorimetry, X-ray diffraction and high-temperature resistivity measurements and he found that at a scanning rate of 10 °C/min for the DSC and 1 °C/min for the resistivity measurements, confirmed by other measurements, that the amorphous Y<sub>0.66</sub>Fe<sub>0.34</sub> crystallises first into the elemental hcp Y at ~307 °C then at ~427 °C into the C15 Laves phase YFe<sub>2</sub> which co-exists with the first phase. These two temperatures are almost the same as I found for these two phases in my DSC measurement of the crystallisation of  $\alpha$ -Y<sub>7</sub>Fe<sub>3</sub>, which were 295 and 413 °C (see figure 4.10). However, he did not see the intermediate phase, YFe, which was, as I mentioned earlier in more details, discovered later in 1998 by Manuel *et al* [4,24,35]. In their studies of the crystallisation of  $\alpha$ -Y<sub>7</sub>Fe<sub>3</sub> using kinetic neutron diffraction where they were able to show that the phases formed were Y, YFe, and YFe<sub>2</sub>. Similarly Kilcoyne *et al* [5] were able to show in a study of the

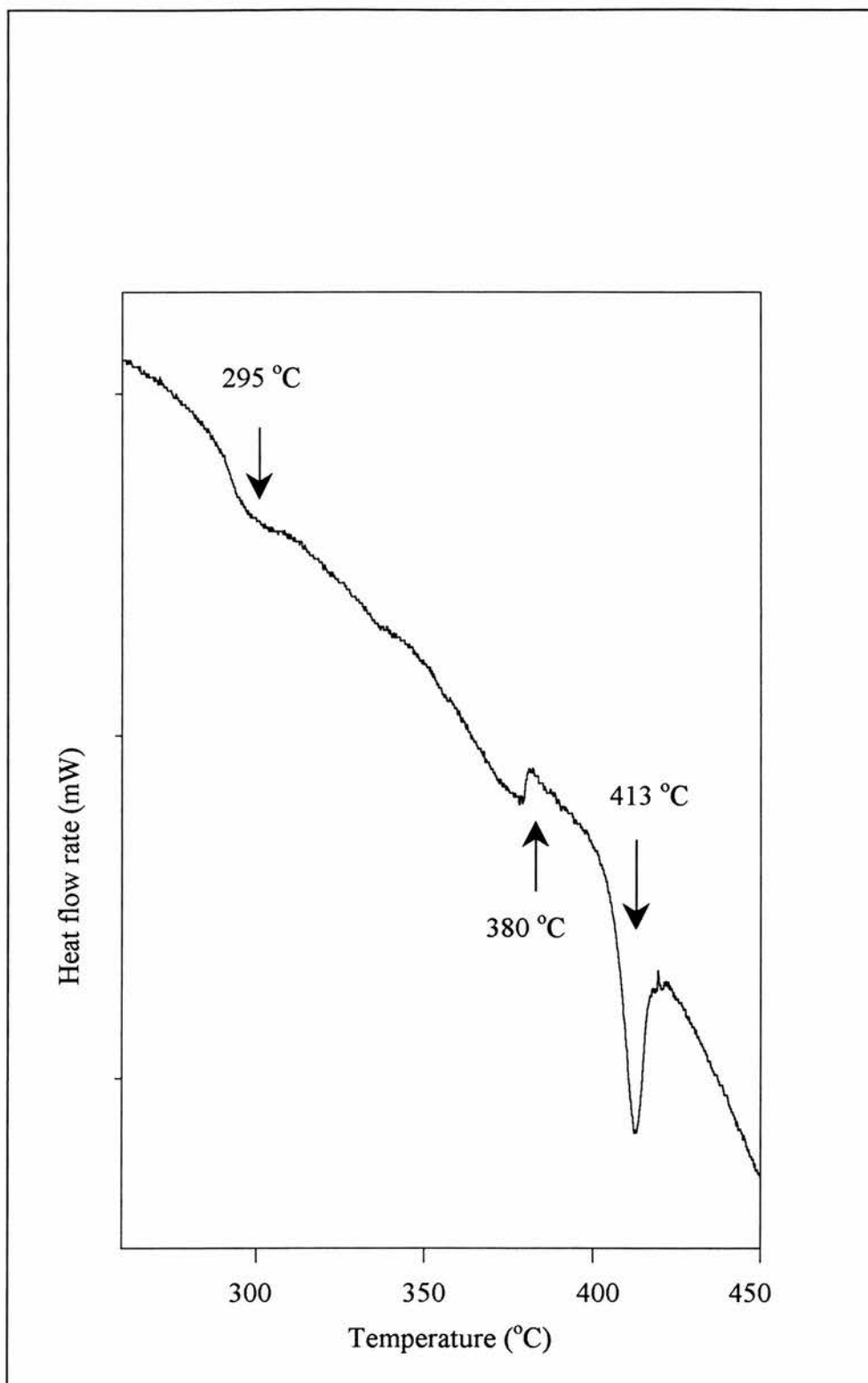
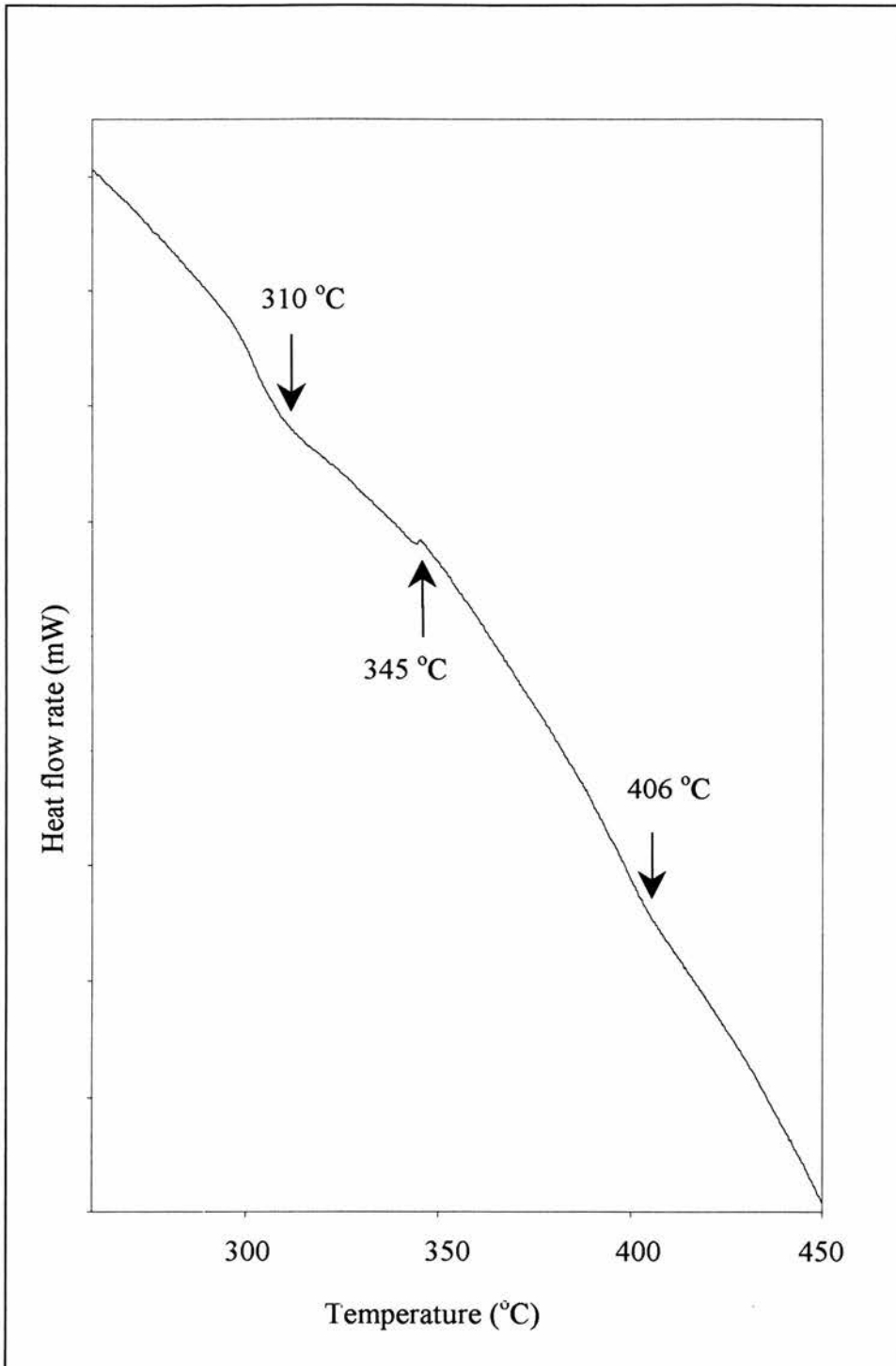


Figure 4.10 Heat flow curve vs. Temperature for  $\alpha\text{-Y}_7\text{Fe}_3$  taken by DSC7 at scanning rate of  $10^\circ\text{C}/\text{min}$  with base line subtracted. The downward arrows show the temperatures of two exothermic dips, 295 and 413  $^\circ\text{C}$ . The upward arrow shows the temperature of an endothermic peak, 380  $^\circ\text{C}$ .

crystallisation of another similar glass,  $\text{Er}_7\text{Fe}_3$ , that it also crystallises through three different phases, Er, ErFe, and  $\text{ErFe}_2$ .

In order to study the possibility of a similar DyFe phase, I have studied the crystallisation of amorphous  $\text{Y}_7\text{Fe}_3$  and  $\text{Er}_7\text{Fe}_3$  alloys using differential scanning calorimetry. My DSC measurements of these two alloys have shown that there are two exothermic dips at about 295 and 413 °C, and an endothermic peak at about 380 °C in the DSC curve from  $\text{Y}_7\text{Fe}_3$ . In figure 4.11 we see that there is an exothermic dip around 310 °C, an endothermic peak around 345 °C, and an exothermic dip at around 406 °C in the DSC curve from  $\text{Er}_7\text{Fe}_3$ . By comparing these two figures, with the curve obtained for  $\text{Dy}_7\text{Fe}_3$  (figure 4.1), it is reasonable to conclude that the very narrow endothermic peak at about 314 °C in figure 4.1 might be a signature of an entirely new, possibly, "DyFe", phase which we could not see in neutron diffraction patterns probably because of the relatively poor resolution and low neutron intensity of POLARIS and the high neutron absorption by Dy element. Therefore, I believe that this experiment should be repeated using neutron diffractometers with higher resolutions and counting statistics such as GEM in ISIS or D20 in ILL.

Furthermore, we know that  $\text{DyFe}_2$  is a positive giant magnetostrictive compound, but with large magnetic anisotropy, which means that very large magnetic fields are required to achieve the giant magnetostiction desired. We also know that  $\text{TbFe}_2$  compound is also a giant magnetostrictive, however with negative magnetic anisotropy. Mixing Tb, Dy, and Fe elements has led to the production of the well known giant magnetostrictive material, Terfenol-D, which has the composition  $\text{Tb}_{0.3}\text{Dy}_{0.7}\text{Fe}_2$ , with increased magnetostriction and reduced anisotropy [w3]. A



*Figure 4.11 Heat flow curve vs. Temperature for  $\alpha\text{-Ee}_7\text{Fe}_3$  taken by DSC7 at scanning rate of  $10^\circ\text{C}/\text{min}$  with base line subtracted. The downward arrows show the temperatures of two exothermic dips, 310 and  $406^\circ\text{C}$ . The upward arrow shows the temperature of an endothermic peak,  $345^\circ\text{C}$ .*

review of giant magnetostrictive materials and their practical utilities and applications was reported by Eda *et al* [37]. I believe that following this route of crystallisation on amorphous Tb-Dy-Fe alloys can contribute to a better understanding of the magnetic structure and properties of the giant magnetostrictive materials, and particularly Terfenols of desired properties can be tailored for specific applications.

I should also mention here that DSC and *in situ* kinetic neutron diffraction measurements using Perkin-Elmer DSC7 calorimeter and POLARIS diffractometer were also carried out on another member of RE-TM alloy family, namely  $\alpha$ -Dy<sub>7</sub>Ni<sub>3</sub>. Preliminary analyses showed that there were at least two crystalline phases evolved at  $\sim 284$  °C and  $\sim 313$  °C. I have been able to identify one of the phases as the orthorhombic compound, Dy<sub>3</sub>Ni<sub>2</sub>, space group Pnma (#62) with the initial unit cell dimensions  $a=6.9433$  Å,  $b=9.5852$  Å and  $c=6.2964$  Å. Unfortunately, I was not able to identify the other phase/phases because of the poor statistics resolution of the POLARIS measurement. Therefore I would suggest another *in situ* neutron diffraction measurement to be carried out using higher count rate neutron diffractometers such as D20 at ILL or GEM at ISIS.

## CHAPTER V

### SUMMARY, CONCLUSIONS AND FUTURE WORK

#### 5.1 SUMMARY AND CONCLUSIONS

In this work I have indicated to the shortcomings and limitations of the standard methods of determining equilibrium phase diagrams, where the materials were mixed and annealed at pre-determined temperatures and for specified periods of time and then quenched to capture the final phases developed. I Then referred to the current trends of research in this area and showed how the previously unavailable facilities (*e.g.* neutron facilities in ISIS and ILL) have paved the way to novel techniques in the study of phase diagrams and to the discovery of new RE-TM compounds [4, 5].

The primary aim of this thesis was the study of the re-crystallisation of amorphous binary RE-TM alloys using *in situ* kinetic neutron diffraction and DSC techniques as a continuation of the main theme motivated by the discovery of the new phases in Y-Fe, Er-Fe and Y-Co in the previous work of our group. Firstly, I studied the crystallisation of  $\alpha$ -Ni<sub>33</sub>Zr<sub>67</sub> alloy using DSC7 and in situ kinetic diffraction measurements at POLARIS. Both measurements have shown the polymorphic crystallisation of this sample into the well know tetragonal compound, NiZr<sub>2</sub>, space group I4/mcm (#140) with cell dimensions, a=6.5082(5) Å & c=5.2951(8)

Å. There was no other intermediate phases formed or transformed in the course of the crystallisation.

Secondly and finally, I studied the crystallisation of  $\alpha$ -Dy<sub>7</sub>Fe<sub>3</sub> alloy using the same techniques as for  $\alpha$ -Ni<sub>133</sub>Zr<sub>67</sub>. I found that the sample crystallises first into the hexagonal elemental Dy then into the cubic C15 Laves phase, DyFe<sub>2</sub> that coexists with the first phase. I also found from the DSC measurement a slight indication to the existence of an intermediate phase Unfortunately I was not able to see this phase in POLARIS diffraction data. By comparing this DSC data with other DSC data I obtained for both Y-Fe and Er-Fe alloys, and by comparing the analysis I carried out of the neutron diffraction data, with the results of the previous kinetic neutron diffraction studies carried out by Kilcoyne *et al* [4, 5] on the crystallisation of amorphous Y-Fe and Er-Fe alloys, I came to the conclusion that a previously unknown new intermediate Dy-Fe phase, possibly DyFe compound, might exist.

## 5.2 FUTURE WORK

The work in this thesis was motivated by the discovery of new RE-TM compounds, which have new interesting magnetic and crystal structures. More researches need to be carried out, as we now have the advantages of novel techniques, which were unavailable for the scientists in the past. The work carried out here on RE-TM systems has exploited *in situ* kinetic neutron diffraction for studying the re-crystallisation of amorphous RE-TM alloys. It is possible to study

a virtually unlimited range of these materials by varying the composition and the elements contained in the precursor alloys.

The first problem is to confirm the presence of the new Dy-Fe phase and to solve the magnetic and crystal structure. This can be done by repeating the Dy-Fe measurements using neutron diffractometers with better resolution and higher flux intensity such as GEM at ISIS or D20 at ILL.

In general, the magnetic properties and atomic structures of all the new RE-TM phases discovered so far still need to be identified. Susceptibility measurements on VSM instrument, magnetic ordering measurements on Mössbauer instrument,  $\mu$ SR measurements at ISIS and further analysis of previous kinetic neutron diffraction data, can solve these problems. Finally, a method of isolating these new phases from the remaining precursors or accompanying phases needs to be developed, possibly via new crystallisation routes or different precursors.

# APPENDIX

## EXPERIMENTAL TECHNIQUES

### A.1 INTRODUCTION

The techniques used in carrying out the measurements in this thesis are primarily, kinetic neutron diffraction using the pulsed neutron powder diffractometer "POLARIS" at ISIS and the differential scanning calorimetry using the Perkin-Elmer "DSC7" calorimeter.

In this chapter, a detailed description of the pulsed neutron source "ISIS", the neutron powder diffractometer "POLARIS", and in more detail the theory of the crystal structure determination using neutron diffraction, the theory of the data analysis "Rietveld refinement", and a brief description of differential scanning calorimetry using the Perkin -Elmer "DSC7" calorimeter will be given.

### A.2 NEUTRON DIFFRACTION

The neutron is a fundamental particle which posses no detectable electrical charge, and has a mass of  $1.675 \cdot 10^{-27}$  Kg, a magnetic moment of -1.913 nuclear magnetons, a spin of  $\frac{1}{2}$ , and a wavelength,  $\lambda$ , given by de Broglie's law [38],

$$\lambda = \frac{h}{mv} \tag{A.1}$$

where,  $h$  is Planck's constant,  $v$  is the neutron velocity and  $m$  is its mass.

The existence of neutron as a neutral particle with a mass almost equal to that of the proton, was first predicted by Lord Rutherford in 1920, and established by Sir J. Chadwick in 1932. Four years later, Mitchell and Powers demonstrated the neutron diffraction in 1936. Finally, Halpern and Johnson explained the magnetic scattering of neutrons in 1939 [38].

Neutrons can only be produced by nuclear reactions (fission or spallation).

To perform neutron diffraction experiments, a very high beam intensity of thermal neutrons is needed, because of its weak interaction with matter. This is usually obtained either by nuclear reactors or high-energy particle accelerators [w4, w5]. A typical flux intensity would be of the order of  $10^{16}$  n/cm<sup>2</sup>/sec [39].

Nuclear reactors give continuous spectrum of neutron energies, white-beam, and therefore, to select a single energy a crystal monochromator is used. Nuclear accelerators also give white neutron beams but with two options, 1) A monochromator crystal can be used to select a single wavelength, or more commonly 2) the beam is given in pulses, a mode which enables the user to get the full advantage of the whole range of the neutron energy spectrum at one go. The wavelength in this case is determined by time of flight, t-o-f, where data is collected at fixed Bragg angles as a function of neutron energy [w4, w5].

Now let us consider why neutrons are very popular and preferable to other kinds of radiation in studying the microscopic structure and dynamics of the condensed matter [7, 38, w6, and w7],

1. The dynamics and the microscopic structure can be measured at the same time.

2. Neutrons can have very wide range of wavelengths from 0.05-20Å. Therefore, It can be used to probe spatial structure at a scale ranging from atomic to macromolecular.
3. Thermal neutrons have energies in the range of meV to eV, which are of the same magnitude as those of atomic and electronic processes. This enables us to probe the molecular translations, rotations, vibrations, lattice modes, and electronic transitions;
4. Unlike X-rays, neutrons scatter from the atomic nuclei of materials. This explains the fact that the neutron scattering length is proportional to the atomic weight and not to the atomic number, the fact which can be exploited to:
  - a) distinguish between different isotopes of the same element.
  - b) distinguish between the neighbouring elements in the periodic table;
  - c) detect the light elements in the presence of heavier elements.
5. Interaction of neutrons with matter is so weak, and therefore they are considered as non-destructive probing tools, and can be used with no damaging effect, even on biological or polymeric materials;
6. Neutrons have a magnetic moment, which provide a probe for investigation of the magnetic ordering of a material and full information about magnetic excitation and magnetic moment distributions at atomic scale. That is, the data collected for chemical structural analysis is suitable at the same time for magnetic structure analysis, since both magnetic and nuclear scattering cross sections are of the same order of magnitude;
7. Neutrons interact weakly with matter causing it a very little disturbance. Therefore, first-order perturbation theory- the Born approximation can

appropriately describe the neutron scattering cross-sections, making data relatively simple to interpret;

8. Again because of the interaction of neutrons with matter is very weak, It is therefore highly penetrative. This facilitates the investigation of the interior part of large samples, where X-rays, electron and optical beams fail.
9. Interaction of neutrons with hydrogen atoms is unique. This can be used to examine the spatial and temporal correlations of hydrogen and deuterium labelled molecules.
10. Neutrons can probe temporal effects ( $10^{-7}$ - $10^{-15}$  s), which completes the available scale by other techniques, where NMR and photon correlation spectroscopy cover the lower range and the electron energy loss and photo-emission spectroscopy cover the higher range.

In my study I used the pulsed neutron source, ISIS, in conducting my diffraction experiments. Therefore, the time of flight technique, t-o-f, was necessarily involved. The description of which is given in details in the following section.

### **A.2.1 THE PULSED NEUTRON SOURCE "ISIS"**

ISIS is the world's most powerful pulsed spallation source, and produces neutrons, muons, and neutrinos with very high brightness. It is situated at Rutherford Appleton Laboratory near Oxford [7, w6]. ISIS is a multi-disciplinary research centre used by scientists from different fields such as physics, chemistry, material science, biology, crystallography and earth science.

Although ISIS produces neutrons, muons, and neutrinos, for studies of condensed matter and fundamental physics [7, w6], I will restrict the following description to the production of neutrons.

There are five main stages in the processes of neutron production [7, 40, and w6],

1. *Ion Source:* In the ion source H and Caesium (Cs Vapour) are mixed together. Electrons released from Cs are trapped by H atoms and form H<sup>-</sup> ions.
2. *Injector:* Once H<sup>-</sup> ions are formed they are extracted and accelerated from the source by the voltage difference between the source (-665 KV) and the first end of a linear accelerator (linac) (0 V). The beam enters the linac, which accelerates it by radio-frequency electric fields to 70 MeV. It is then injected to another accelerator, the synchrotron.
3. *Synchrotron:* At the injection into the synchrotron the electrons are stripped from H<sup>-</sup> ions by means of a very thin alumina foil (0.25 mm thick) and protons are produced. The synchrotron circulates the protons and continues to accelerate them until their energies are reached to 800 MeV.
4. *Target Station:* These highly energetic protons are then guided to a target station made from a heavy metal such as tantalum, uranium...etc. Upon collision each proton produces many neutrons.
5. *Moderator:* However, neutrons have very high energies and consequently very short wave lengths. To use them in the field of condensed matter research, their wavelengths should be increased, i.e. to atomic and molecular scales, therefore they are slowed down by surrounding the target with hydrogenous materials. At ISIS the moderators are ambient temperature water (316K, H<sub>2</sub>O), liquid methane (100K, CH<sub>4</sub>) and liquid hydrogen (20K, H<sub>2</sub>).

The neutrons coming out from the moderators are guided into beam-lines which lead to different instruments such as POLARIS, CRISP...etc. (as shown in figure A.1 [w8]).

The neutrons generated by the ISIS source have rather different characteristics than those generated by a nuclear reactor [7, w6],

1. The energy and wavelength of each neutron is directly determined by using time of flight technique on the white neutron beam.
2. Using small moderators preserve sharpness of the initial 0.4  $\mu$ S neutrons pulse, and also give rich epithermal neutrons
3. Using white beams enables fixed scattering geometries to be used.
4. Wide spectral range in both momentum transfer and energy is covered.
5. The pulse nature of the beam can be exploited to study sharp transitions and time dependant kinetic parameters.
6. Good signal-to-noise levels are ensured by the duty cycle of the accelerator.

## **A.2.2 THE NEUTRON POWDER DIFFRACTOMETER**

### **"POLARIS"**

POLARIS [6, 41, w9, and w10] is a medium resolution, high intensity powder diffractometer located on beam-line N7 at ISIS. It utilises fixed geometry diffraction method, where the time of flight technique is used. Some of its characteristics and applications are:

1. The ability of rapid structure characterisation;

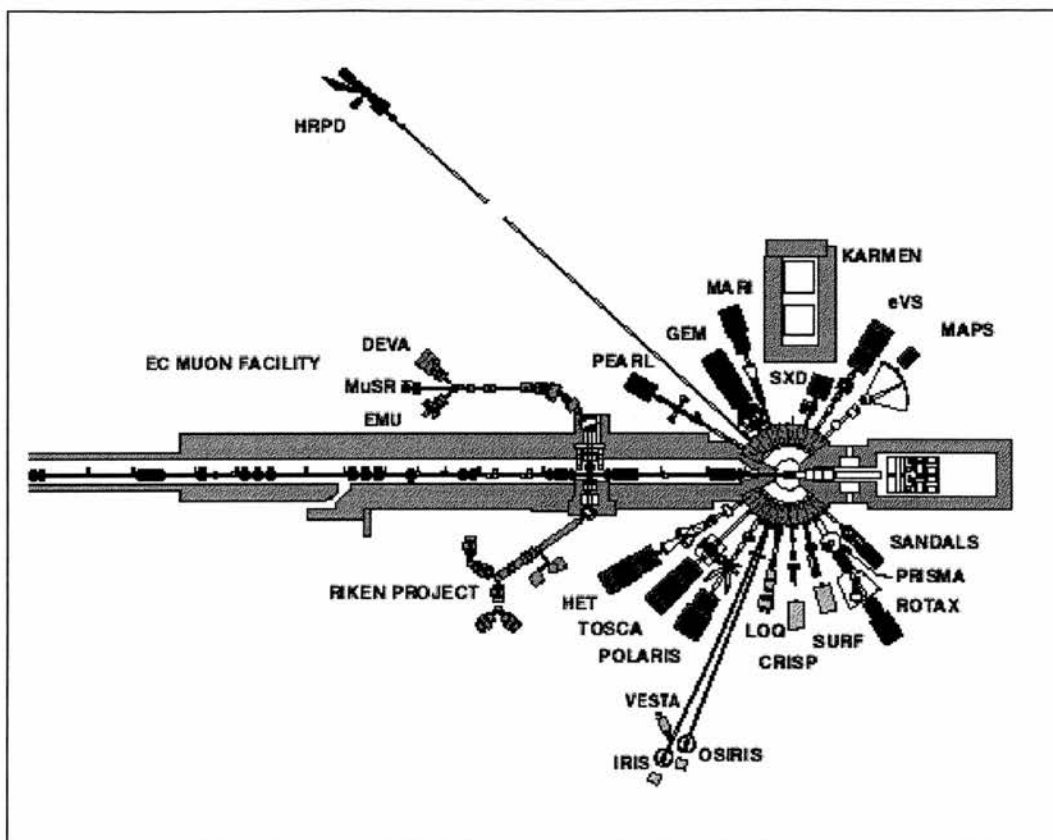


Figure A.1 The ISIS facility [w8].

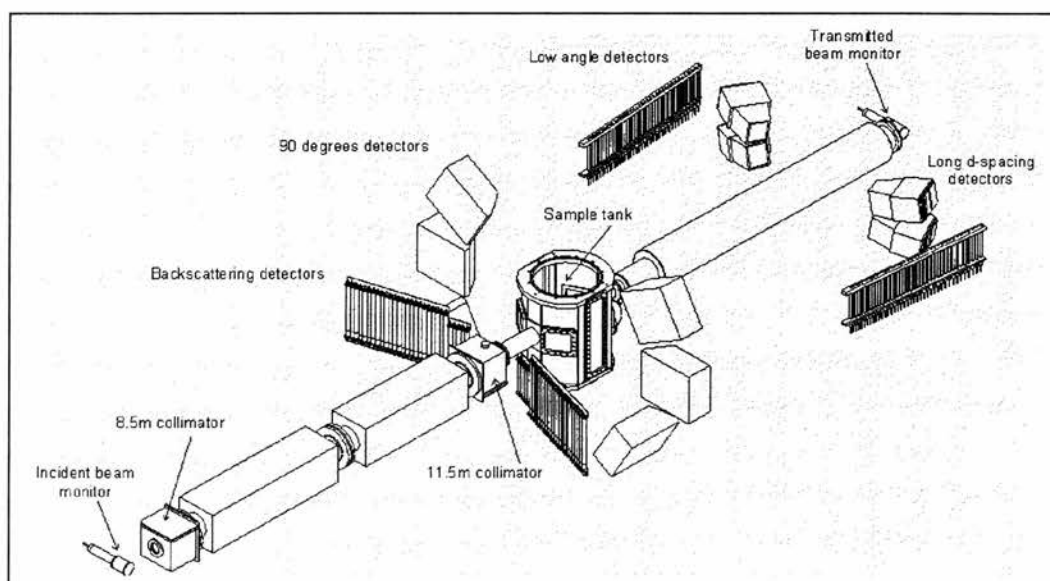


Figure A.2 POLARIS the powder diffractometer [w10].

2. The ability to run in-situ experiments at non-ambient temperatures or at high pressures (over 25 GPa);
3. The ability to collect data suitable for *ab-initio* structural characterisation.
4. The ability to study very small samples (less than 1 mm<sup>3</sup>);
5. The ability to measure effects of extremely short lives (10<sup>-7</sup>-10<sup>-15</sup> s);
6. The availability of intense epithermal neutrons at ISIS allows measurements of very short d-spacing down to 0.3 Å;
7. The ability to study the magnetic ordering of materials;
8. The ability to measure thermal vibration parameters and site occupancies.

The design of the instrument is shown in figure A.2. POLARIS receives a white beam of neutrons from a 295 K H<sub>2</sub>O moderator poisoned with Gd. There are a total of 434 <sup>3</sup>He gas filled and ZnS scintillator detectors arranged in four banks. The details are described in Table A.1.

It is straightforward to deduce the relationship between  $d$  the inter-planer spacing and the total time of flight,  $t$ ,

$$d(\text{Å}) = \frac{1.977 \times 10^{-3}}{L(\text{m}) \sin \theta} t(\mu\text{s}) \quad (\text{A.2})$$

The resolution,  $\Delta d/d$ , of any detector in the POLARIS instrument is given by,

$$R_d = \frac{\Delta d}{d} = \left[ (\Delta\theta \cot \theta)^2 + \left( \frac{\Delta t}{t} \right)^2 + \left( \frac{\Delta L}{L} \right)^2 \right]^{1/2} \quad (\text{A.3})$$

where,  $d$  is the d-spacing,  $\theta$  is the detector angle,  $t$  is the total time of flight, and  $L$  is the total flight path from moderator to the detector. Relation (A.3) is the key relation in the design of neutron powder diffractometers, where detectors aligned accordingly to keep the resolution constant at each detector bank. A quick look at this relation can tell us that the resolution is at its worst at low angles and at its best at large angles.

Table A.1. POLARIS detector configuration [w10]

<b>Position</b>	<b>Very low angle (B)</b>	<b>Low angle (A)</b>	<b>90 degrees (E)</b>	<b>Backscattering (C)</b>
<b>Type</b>	ZnS scintillator	½" <sup>3</sup> He tubes	ZnS scintillator	1" <sup>3</sup> He tubes
<b>No. of detectors</b>	80	80	216	58
<b>2θ range</b>	13°-15°	28° - 42°	85° - 95°	130° - 160°
<b>Ω(steradians)</b>	0.009	0.046	0.48	0.29
<b>Δd/d (%)</b>	3 × 10 <sup>-2</sup>	1 × 10 <sup>-2</sup>	7 × 10 <sup>-3</sup>	5 × 10 <sup>-3</sup>
<b>L<sub>2</sub> (m)</b>	~ 2.2	1.72 - 2.65	~0.8	0.60 - 1.30
<b>d range (Å )</b>	0.5 - 21.6	0.5 - 8.3	0.2 - 4	0.2 - 3.2
<b>Q-range (Å<sup>-1</sup>)</b>	0.3 - 12.6	0.75 - 12.6	1.5 - 31.4	2.0 - 31.4

The resolution gets better for longer flight paths as in a different diffractometer design, HRPD [28] at ISIS.

### **A.3. CRYSTAL STRUCTURE DETERMINATION FROM NEUTRON DIFFRACTION**

#### **A.3.1 PRINCIPLE OF STRUCTURE DETERMINATION**

The wavelength of any radiation is dependent on its energy,

$$\lambda = \frac{h}{\sqrt{2mE}} \quad (\text{For corpuscle radiation (de Broglie wavelength)}) \quad (\text{A.4})$$

$$\lambda = \frac{hc}{E} \quad (\text{For electromagnetic radiation}) \quad (\text{A.5})$$

where,  $\lambda$  is wavelength,  $h$  is Planck constant,  $m$  is the mass of the corpuscle,  $E$  is its kinetic energy and  $c$  is the speed of light.

The length of visible light waves limits the resolution of optical microscope, which is of the order of 500 Å. Radiation with wavelengths smaller or approaching inter-atomic distances should be used to see the atoms. This leads us to use radiation such as X-ray ( $\lambda \sim 1$  Å), high-energy electron sources ( $\lambda \sim 0.01$  Å) or thermal neutron sources ( $\lambda \sim 1$  Å).

## A.3.2 CRYSTAL STRUCTURE INVESTIGATION BY NEUTRONS

Neutrons are one of the most powerful tools in studying the basic interactions responsible in forming the condensed matter state. For structural investigations, thermal neutrons ( $E \sim 25$  meV) are used in diffraction experiments. Diffraction patterns are collected, and if the material is crystalline the lattice parameters and the atomic positions can be inferred.

### A.3.2.1 BRAGG'S LAW [42, 43]

Since the neutrons have wave properties, Bragg's law, as described below, governs their scattering from crystals.

If we assume that the crystallographic parallel atomic planes work as reflective mirrors against the incident wave, and the scattering is assumed to be elastic, *i.e.* the wavelength does not change by reflection, then the path difference of the reflecting rays from two neighbouring planes will equal to,

$$\text{Path difference} = PQ + QR = 2d \sin \theta = n\lambda \quad (\text{A.6})$$

Where,  $d$  is the distance between two nearest neighbouring parallel planes,  $\lambda$  is the neutron wavelength,  $\theta$  is the reflection angle and  $n$  is an integer number. This is known as Bragg's law, which is demonstrated diagrammatically in figure A.3. Because of  $0 < \sin \theta < 1$ , therefore,  $\lambda < 2d$  is an important condition for this law to work..

The Bragg condition can also be written in the reciprocal lattice in a simple way. For demonstration purpose I have redrawn figure A.3 in a vector space as shown in figure

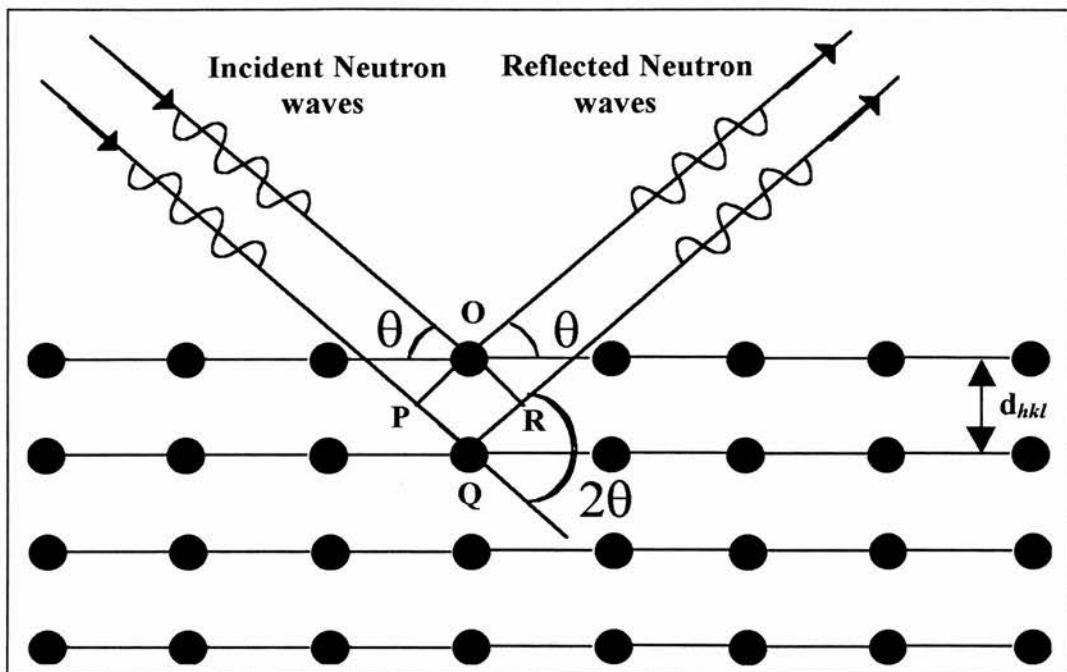


Figure A.3 Diffraction of neutron beams from crystallographic planes  
(Bragg condition)

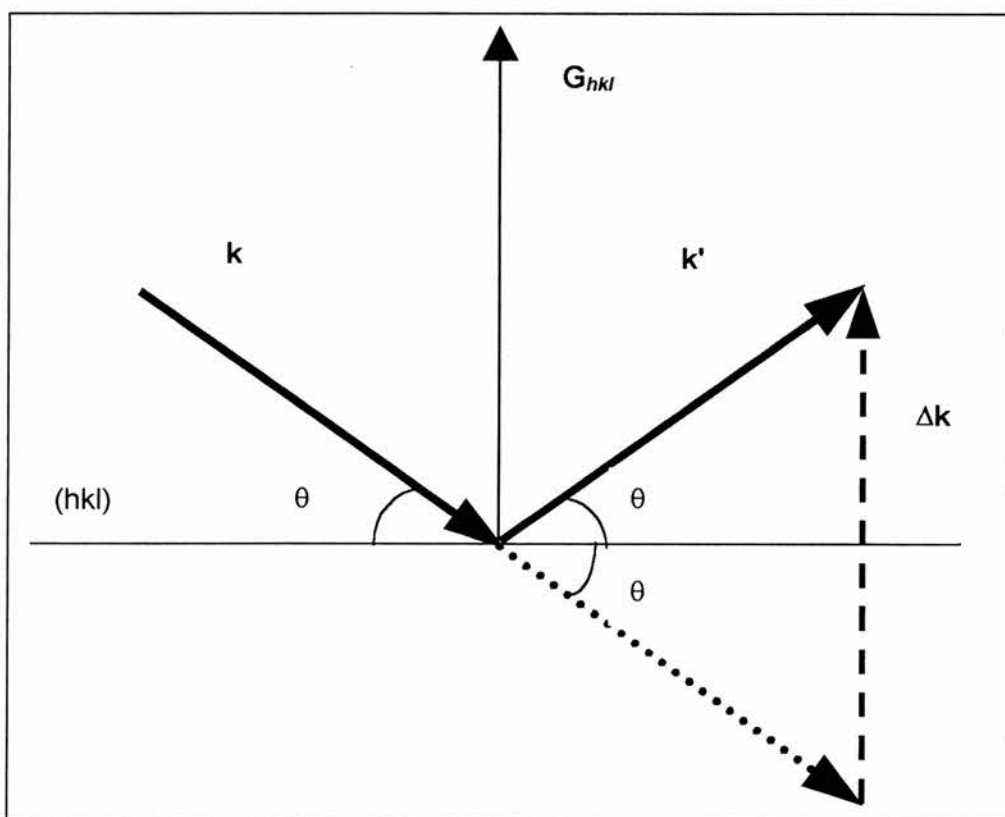


Figure A.4 Vector representation of neutron diffraction from a group of parallel planes  $(hkl)$  in the reciprocal space. The Bragg condition is realised when  $\Delta \mathbf{k} = \mathbf{G}_{hkl}$ .

A.4. The reciprocal lattice is built up by the vectors  $\mathbf{a}^*$ ,  $\mathbf{b}^*$  and  $\mathbf{c}^*$  which are defined as the following,

$$\mathbf{a}^* = 2\pi \frac{\mathbf{b} \times \mathbf{c}}{V}, \quad \mathbf{b}^* = 2\pi \frac{\mathbf{c} \times \mathbf{a}}{V}, \quad \mathbf{c}^* = 2\pi \frac{\mathbf{a} \times \mathbf{b}}{V} \quad (\text{A.7})$$

where,

$V = \mathbf{a} \cdot (\mathbf{b} \times \mathbf{c})$  is the volume of the elementary unit cell in real space.  $\mathbf{a}$ ,  $\mathbf{b}$  and  $\mathbf{c}$  are the basis vectors of the real lattice.

In the reciprocal space, a vector  $\mathbf{G}$  can represent each group of parallel planes  $(hkl)$ , which is always perpendicular to these planes,

$$\mathbf{G} = h\mathbf{a}^* + k\mathbf{b}^* + l\mathbf{c}^*$$

where,  $(hkl)$  are the Miller indices for the parallel lattice planes,

From the definitions (A.7), it can be seen that,

$$\left. \begin{aligned} \mathbf{a}^* \cdot \mathbf{a} &= \mathbf{b}^* \cdot \mathbf{b} = \mathbf{c}^* \cdot \mathbf{c} = 2\pi \\ \mathbf{a}^* \cdot \mathbf{b} &= \mathbf{a}^* \cdot \mathbf{c} = 0 \\ \mathbf{b}^* \cdot \mathbf{c} &= \mathbf{b}^* \cdot \mathbf{a} = 0 \\ \mathbf{c}^* \cdot \mathbf{a} &= \mathbf{c}^* \cdot \mathbf{b} = 0 \end{aligned} \right\} \quad (\text{A.8})$$

It can be shown that the inter-planar spacing  $d_{hkl}$  is equal to  $2\pi$  divided by the modulus of the reciprocal lattice vector defined by  $hkl$ , i.e.,

$$d_{hkl} = \frac{2\pi}{|\mathbf{G}_{hkl}|} \quad (\text{3.9})$$

Hence, Bragg condition can be rewritten as,

$$\mathbf{K} = \mathbf{G}_{hkl} \quad (\text{A.10})$$

where,  $\mathbf{K} = \mathbf{k}' - \mathbf{k}$  is the difference wave vector between incident wave  $\mathbf{k}$  and the scattered wave  $\mathbf{k}'$  as demonstrated in figure A.4.

It can also be written in component form,

$$\left. \begin{aligned}
 \mathbf{a} \cdot \mathbf{K} &= 2 \pi h \\
 \mathbf{b} \cdot \mathbf{K} &= 2 \pi k \\
 \mathbf{c} \cdot \mathbf{K} &= 2 \pi l
 \end{aligned} \right\} \quad (\text{A.11})$$

In crystal analysis there are two important measurements: reflection angles and the intensity of the reflected beams.

### A.3.2.2 DIFFRACTED INTENSITY [43]

When a neutron, described by a plane wave  $\exp(i\mathbf{k}\mathbf{r})$ , impinges elastically on a nucleus, it scatters with a spherical wave of amplitude  $-\frac{b}{r} \exp(i\mathbf{k}\mathbf{r})$  at a distance  $r$  from the nucleus (see figure A.5).  $b$  is called the neutron coherent scattering length and is different for different nuclei.

To study the diffraction of a neutron beam by a crystal, we consider each elementary cell as a scattering unit with scattering amplitude,  $F$ , which equals the coherent scattering length,  $b$ , if the unit cell has only one nucleus. So, if we sum the amplitudes of waves scattered by all elementary cells taking into account the phase difference,  $\mathbf{K}\mathbf{R}_i$  from each individual cell at position  $\mathbf{R}_i$  from the origin of chosen co-ordinates, we get the total amplitude  $\Psi$  of the scattered wave from the lattice,

$$\Psi \sim F \cdot \sum_i e^{i\mathbf{K} \cdot \mathbf{R}_i} = F \cdot \sum_{n_1=0}^{N_1-1} e^{i\mathbf{K}_{n_1} \cdot \mathbf{a}} \cdot \sum_{n_2=0}^{N_2-1} e^{i\mathbf{K}_{n_2} \cdot \mathbf{b}} \cdot \sum_{n_3=0}^{N_3-1} e^{i\mathbf{K}_{n_3} \cdot \mathbf{c}} \quad (\text{A.12})$$

It was assumed that the lattice contains  $N_1$  units along the direction,  $\mathbf{a}$ ,  $N_2$  units along  $\mathbf{b}$  and  $N_3$  units along  $\mathbf{c}$ . The intensity,  $I$ , of the Bragg diffraction is proportional to the square of its amplitude, So by summing eq. (A.12) and squaring it we get,

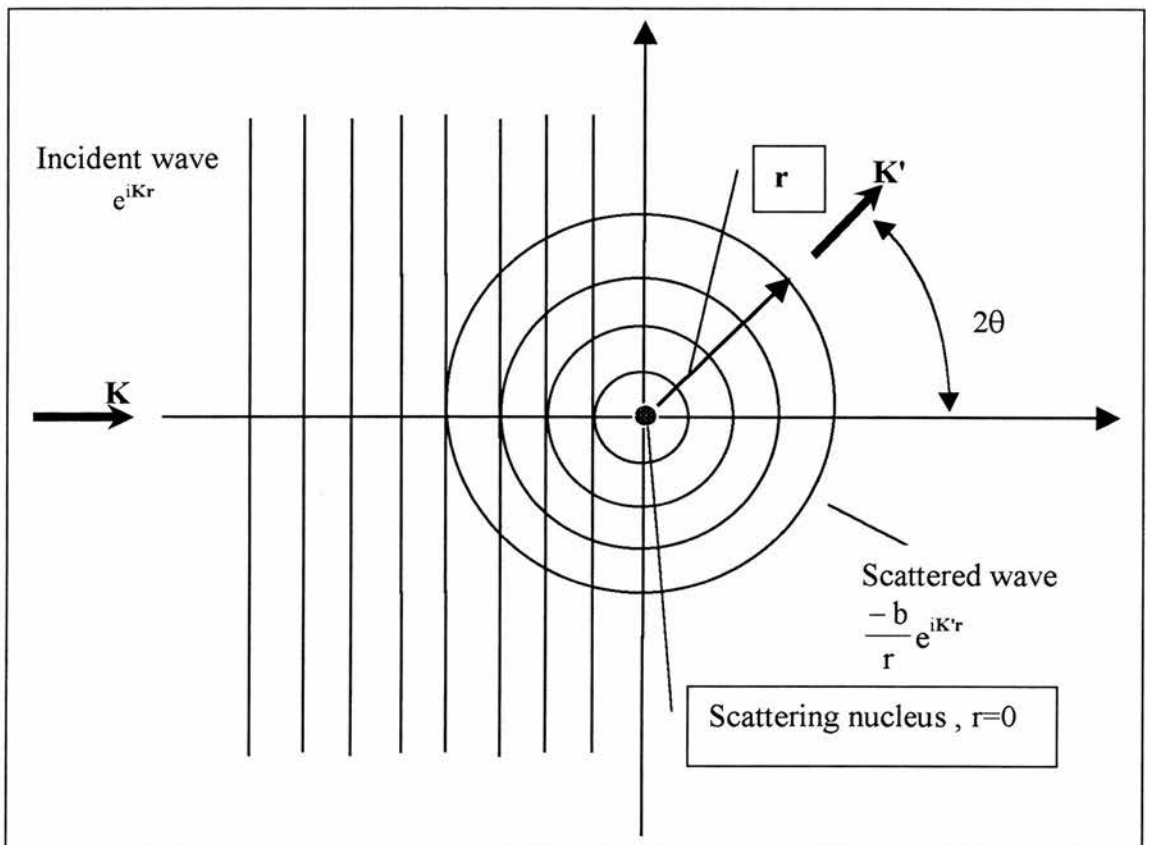


Figure A.5 Neutron elastic scattering from a nucleus, where,  $|\mathbf{K}| = |\mathbf{K}'|$

$$I \sim |\Psi|^2 = |F|^2 \cdot \frac{\sin^2(\frac{1}{2} \cdot N_1 \cdot \mathbf{K} \cdot \mathbf{a})}{\sin^2(\frac{1}{2} \cdot \mathbf{K} \cdot \mathbf{a})} \cdot \frac{\sin^2(\frac{1}{2} \cdot N_2 \cdot \mathbf{K} \cdot \mathbf{b})}{\sin^2(\frac{1}{2} \cdot \mathbf{K} \cdot \mathbf{b})} \cdot \frac{\sin^2(\frac{1}{2} \cdot N_3 \cdot \mathbf{K} \cdot \mathbf{c})}{\sin^2(\frac{1}{2} \cdot \mathbf{K} \cdot \mathbf{c})} \quad (\text{A.13})$$

It can be seen from eq. (A.13) that the intensity,  $I$ , varies periodically with  $\mathbf{K}$ , and has maximum values every time Bragg condition is satisfied (see eqs. (A.11)). It can be deduced from eq. (A.13) that the maximum intensity is proportional to  $(N_1^2 N_2^2 N_3^2)$  and the width of the fringes is inversely proportional to  $(N_1 N_2 N_3)$ , therefore the (integrated) intensity will be proportional to the division of the first factor by the second one, i.e. proportional to  $(N_1 N_2 N_3)$  which is the volume of the diffracting sample. This is valid only in the case of small samples where multiple scattering is trivial. Eq. (A.13) enables us to determine the symmetry and the basis lattice vectors  $\mathbf{a}$ ,  $\mathbf{b}$  and  $\mathbf{c}$  by knowing the positions of the diffraction peaks.

However we still need to study the structure factor,  $F$ , for its role in the diffraction peaks intensities. The structure factor,  $F$ , is in fact the scattering amplitude of a unit cell and is defined as the sum of the neutron coherent scattering lengths,  $b_i$ , of all individual atoms,  $i$ , located inside the unit cell taking into account the appropriate phase differences,  $e^{-i\mathbf{K} \cdot \rho_i}$ , Thus,

$$F = \sum_i f_i = \sum_i b_i e^{-i\mathbf{K} \cdot \rho_i} \quad (\text{A.14})$$

where,  $\mathbf{K} = \mathbf{k} - \mathbf{k}'$  is the neutron wave-vector transfer,  $\rho_i$  is the position vector of each atom,  $i$ , in the unit cell with respect to origin of the unit cell itself, *i.e.*:

$$\rho_i = x_i \mathbf{a} + y_i \mathbf{b} + z_i \mathbf{c} \quad (\text{A.15})$$

where,  $(x_i, y_i, z_i)$  is the co-ordinates of the atoms in the unit cell, given in units of the lattice generator lengths  $(a, b, c)$ .

We know when Bragg condition is satisfied we have,



$$\mathbf{K} = \mathbf{G} = h\mathbf{a}^* + k\mathbf{b}^* + l\mathbf{c}^* \quad (\text{A.16})$$

By substituting eqs. (A.15) and (A.16) into eq. (A.14) and taking into account eq.(A.11), we get the *structure factor* for the crystallographic plane  $(hkl)$ ,

$$F_{hkl} = \sum_i b_i e^{2\pi i(hx_i + ky_i + lz_i)} \quad (\text{A.17})$$

From eq. (A.17) we notice that,

1. The structure factor,  $F_{hkl}$ , has different values for different crystallographic planes  $(hkl)$ .
2.  $F_{hkl}$  is also a function of the positions of the atoms,  $(x_i, y_i, z_i)$ , inside a unit cell.

We know that the intensities of the diffraction peaks are proportional to the square of the structure factors, i.e.  $I_{hkl} \sim |F_{hkl}|^2$ . Inversely, one may infer the positions of the atoms,  $(x_i, y_i, z_i)$ , in a unit cell, by knowing the intensities of the diffraction peaks and the scattering lengths,  $b_i$ , of each atom constituting the unit cell, in condition that the phases connected with each  $b_i$  is either 0 or  $\pi$ , i.e. when the structure of the crystal is centrosymmetric.

So far the atoms in the crystal were assumed to be at rest. In reality atoms are constantly in motion and they vibrate around their equilibrium positions. This means some of neutrons impinging on these atoms can lose or gain energy depending on whether they increase or decrease the motion of these atoms. This means some neutrons will scatter inelastically and incoherently. This will subsequently cause a reduction in the intensity of the Bragg peaks, and a discrepancy will appear between the observed and theoretically calculated peaks. To solve this problem, Debye and Waller introduced a new factor into the mathematical expression of the structure factor that reduces the overall structure factor. This factor is called *Debye-Waller*

factor, which is in its simplest form  $e^{-\tilde{B}K^2}$ . Thus, the structure factor has the new form,

$$F_{hkl} = \sum_i b_i e^{-\tilde{B}K^2} e^{2\pi i(hx_i + ky_i + lz_i)} \quad (\text{A.18})$$

For the Bragg scattering we have  $|K| = |\mathbf{G}| = \frac{2\pi}{d} = \frac{4\pi \sin \theta}{\lambda}$ . Substituting this into eq. (A.18), we get,

$$F_{hkl} = \sum_i b_i \cdot e^{-B \left(\frac{\sin \theta}{\lambda}\right)^2} \cdot e^{2\pi i(hx_i + ky_i + lz_i)} \quad (\text{A.19})$$

where,  $B = 4\pi \tilde{B} = \text{constant}$ .  $\tilde{B}$  is directly related to the average square amplitude of the atomic motion and depends on temperature and pressure. Some values of  $\tilde{B}$  can be found in the International Tables of Crystallography [44]. For some materials, Debye-Waller factor can also be dependent on the direction of  $\mathbf{K}$ .

As a summary, the crystal symmetry and the unit cell parameters are determined from the locations of the diffraction peaks, while the position of the atoms are determined from the structure factor which is calculated from the intensity of these peaks. In addition, we can get information about the crystal size (or the crystalline grains in case of polycrystalline materials or powdered crystals) from the shape (width) and the intensity of the diffraction peaks.

## A.4 RIETVELD REFINEMENT

Growing large single crystals is not an easy task to achieve and it is often practically impossible for most materials. However forming very small crystallites does not need much effort, and diffraction patterns can be collected from these numerous crystallites

by a technique called powder diffraction. However, this method has a major drawback, when large portions of the data overlap, serious difficulties in structure determination are encountered. This drawback is overcome by the Rietveld method, which is simply a computer program employs least squares iteration techniques.

The Rietveld method is a powerful tool for extracting information about crystal structures from neutron and X-ray powder diffraction patterns. It is also so beneficial in quantitative phase analysis, and most recently in the determination of crystallite size and micro-strain parameters. It is a very valuable tool for researchers working in different fields such as crystallography, material science, chemistry and physics.

In the following I shall describe the Rietveld method in refining nuclear and magnetic structures which employs the direct intensities rather than single or overlapping peak integrated intensities from neutron powder diffraction patterns.

This method reserves the information contained in the overlapping peaks and therefore is advantageous over the refinement methods of integrated intensities of the separate groups of overlapping peaks [45], where this information is lost.

First I shall describe the Rietveld Method for the single wavelength powder diffraction analysis because of its relative simplicity, then generalise it into time of flight powder diffraction analysis because it is much more complicated but the principle is the same.

#### **A.4.1 RIETVELD METHOD FOR A SINGLE WAVELENGTH NEUTRON POWDER DIFFRACTION [46]**

To describe the measured neutron diffraction peak shape, it is essential to find an appropriate mathematical function. It was found that the peak shape is dependent on

several factors: The neutron spectral distribution, the monochromator mosaic distribution, the transmission functions of the Soller slits, and the sample shape and crystallinity. It is found empirically that the convolution of these factors is almost an exact Gaussian function. However, we should note that each of these individual factors does not necessarily have a Gaussian shape.

If we assume that each individual Bragg peak has the above mentioned Gaussian shape, their contribution to the observed profile,  $y_i$ , at position,  $2\theta_i$ , can be written as,

$$y_i = t S_k^2 j_k L_k \frac{2\sqrt{\ln 2}}{H_k \sqrt{\pi}} \exp \left[ -4 \ln 2 \left( \frac{2\theta_i - 2\theta_k}{H_k} \right)^2 \right] \quad (\text{A.20})$$

where,

$t$  is the step width of the counter,

$S_k^2 = F_k^2 + J_k^2$ , is the sum of the nuclear and magnetic contribution, respectively,

$j_k$  is the multiplicity of the reflection,

$L_k$  is the Lorentz factor,

$2\theta_k$  is the calculated position of the Bragg peak corrected for the zero-point shift of the counter,

$H_k$  is the full width at half maximum.

$y_i = Y_i - B_i$  is the corrected intensity, where,  $Y_i$  is the observed intensity at the angle  $2\theta_i$ , and  $B_i$  is the back ground for the intensity  $Y_i$ , ( $B_i$  is obtained by linear interpolation of different points on the observed diffraction pattern, and determined graphically)

The subscript,  $k$ , labels the number of the single Bragg peak, while,  $i$ , refers to any point on the diffraction peak. Equation (A.20) can be rewritten in a simpler form,

$$y_i = I_k \exp \left[ -b_k (2\theta_i - 2\theta_k)^2 \right] \quad (\text{A.21})$$

by writing the maximum intensity of the Bragg peak,  $k$ , as,

$$I_k = t S_k^2 j_k L_k \frac{2\sqrt{\ln 2}}{H_k \sqrt{\pi}} \quad (\text{A.22})$$

where,

$$b_k = \frac{4 \ln 2}{H_k^2} \quad (\text{A.23})$$

However, this peak shape is not very simple as it might seem, and an explanation of some of the terms involved is given next.

### a) The peak width $H_k$

The peak width,  $H_k$ , is not the same for all diffraction peaks, and varies with the diffraction angle according to the following equation.

$$H_k^2 = U(\tan \theta_k)^2 + V \tan \theta_k + W \quad (\text{A.24})$$

where,  $U$ ,  $V$  and  $W$  are the half-width parameters and found by measuring  $H_k$  from the diffraction pattern. When this equation was formulated the particle size effect on peak broadening was kept in mind. However, the particle size broadening effect problem will be discussed in detail later in section (d).

### b) The asymmetry of the peak shape

The shapes of the real diffraction peaks are not exactly Gaussian and show asymmetry about their maxima, where these maxima tend to shift to direction of higher d-spacing. However, the integrated intensities remain unchanged. The reason for this shift is the finite heights of the slits and the sample. Equation (A.21) can be modified to correspond with the real peak shapes by adding a semi-empirical correction factor for asymmetry. Thus it becomes,

$$y_i = I_k \exp\left[-b_k (2\theta_i - 2\theta_k)^2\right] \cdot \left\{1 - P(2\theta_i - 2\theta_k)^2 \cdot \frac{s}{\tan \theta_k}\right\} \quad (\text{A.25})$$

where, P is the asymmetry parameter, and ( $s = +1, 0, -1$ ) depending on the difference, ( $2\theta_i - 2\theta_k = +, 0, -$ ).

### c) Preferred orientation correction

An important problem in powder diffraction is preferred orientation, where crystallites are often distributed nonuniformly in the polycrystalline specimen, due to the preparation technique or the behaviour of the crystallites themselves. This often leads to systematic changes in the integrated intensities [29]. In the special case, when these crystallites are disc-shaped they tend to align their normals in the direction of the cylindrical sample holder axis.

The intensities of the diffraction patterns can be corrected by introducing a preferred orientation correction factor as follows,

$$I_{\text{corr}} = I_{\text{obs}} \exp(-G \alpha^2) \quad (\text{A.26})$$

where,  $\alpha$  is the acute angle between the scattering vector and the normal to the crystallite, and G is the preferred orientation parameter.

The distribution of the normals about the preferred orientation is assumed to be Gaussian and G gives a measure of the half-width of this distribution.

### d) The Lorentz factor $L_k$

The Lorentz factor,  $L_k$ , was introduced because of the broadening effects of the imperfections in the crystal. The Lorentzian shape was chosen because of its extended tails, which can make the peak spread away from its centre. The broadening effect reduces the overall resolution power of the instrument, and it depends on the sizes of the imperfections. The smaller the extent of the imperfections is the broader the peaks are and subsequently the smaller the resolution is. For small crystallites this can be

proven by using the Laue equations (A.13) where we mentioned that the width of the Bragg peak is inversely proportional to the crystal size (for this case to the small crystallite size).

Since the powder particles (granules) usually have more than one domain (small crystallites), it is not possible to infer their sizes from the broadening.

It is worthwhile mentioning, that in case of time of flight, t-o-f, neutron powder diffraction (which will be described later in section A.4.3), the broadening caused by the particle size increases as the wavelength increases.

#### e) The structure factor $S_k$

The structure factor  $S_k$  is composed of two factors, a nuclear term,  $F_k$ , and a magnetic term,  $J_k$ . When the effect of thermal vibration of the constituent atoms and the preferred orientation is taken into account, we can write the structure,  $S_k$ , as,

$$S_k^2 = (F_k^2 + J_k^2) \exp\left(-2Q\left(\frac{\sin \theta_k}{\lambda}\right)^2 + G \alpha_k^2\right) \quad (\text{A.27})$$

where,  $Q$  is the over all isotropic temperature factor. Now, let us discuss each of the structure factors in more details,

- (i) The expression for the nuclear structure factor,  $F_k^2$ , can be written as (see eq. (A.19)),

$$F_k^2 = A_k^2 + B_k^2 \quad (\text{A.28})$$

where,

$$A_k = \sum_i n_i b_i \exp\left[-B_i\left(\frac{\sin \theta_k}{\lambda}\right)^2\right] \sum_r \cos 2\pi(h x_{i,r} + k y_{i,r} + l z_{i,r}) \quad (\text{A.29})$$

and,

$$B_k = \sum_i n_i b_i \exp \left[ -B_i \left( \frac{\sin \theta_k}{\lambda} \right)^2 \right] \sum_r \sin 2\pi(h x_{i,r} + k y_{i,r} + l z_{i,r}) \quad (\text{A.30})$$

where,

$\sum_i$  is the summation over all atoms in the asymmetric unit,

$\sum_r$  is the summation over all equivalent positions,

$b_i$  is the coherent scattering length of the  $i^{\text{th}}$  atom,

$B_i$  is the individual isotropic temperature parameter,

$n_i$  is the site occupation number,

$x_{i,r}, y_{i,r}, z_{i,r}$  is the fractional co-ordinates of the  $i^{\text{th}}$  atom in the  $r^{\text{th}}$  equivalent position,

$h, k, l$  are the Miller indices pertaining to  $F_k^2$ .

$n_i = \frac{m}{M}$  for fully occupied lattice; where,  $m$  is the multiplicity of the position,

special or general and it ranges from  $1 \rightarrow M$ , and  $M$  is the multiplicity of the general position in the particular space group.

- (ii) The expression for the magnetic scattering coherent cross section,  $J_k$ , can be written as,

$$J_k^2 = |\mathbf{P}_e|^2 - |\hat{\mathbf{e}} \cdot \mathbf{P}_e|^2 \quad (\text{A.31})$$

where,

$\hat{\mathbf{e}}$  is the unit vector in the direction of the scattering vector  $\mathbf{d}^*$ ; where,

$$\mathbf{d}^* = h\mathbf{a}^* + k\mathbf{b}^* + l\mathbf{c}^* \quad (\text{A.32})$$

$\mathbf{P}_e$  is the magnetic structure factor, and can be resolved into its components,

$$\mathbf{P}_e = (\mathbf{A}_x + \mathbf{A}_y + \mathbf{A}_z) + i(\mathbf{B}_x + \mathbf{B}_y + \mathbf{B}_z)$$

where,

$$\mathbf{A}_X = \frac{e^2 \gamma}{2mc^2} \sum_i n_i f_i \exp \left[ -B_i \left( \frac{\sin \theta_k}{\lambda} \right)^2 \right] \cdot \sum_r \mathcal{H}_{i,X,r} \cos 2\pi(h_{X_{i,r}} + k_{Y_{i,r}} + l_{Z_{i,r}}) \quad (\text{A.33})$$

$$\mathbf{B}_X = \frac{e^2 \gamma}{2mc^2} \sum_i n_i f_i \exp \left[ -B_i \left( \frac{\sin \theta_k}{\lambda} \right)^2 \right] \cdot \sum_r \mathcal{H}_{i,X,r} \sin 2\pi(h_{X_{i,r}} + k_{Y_{i,r}} + l_{Z_{i,r}}) \quad (\text{A.34})$$

where,

X=x, y, z

e is the electron charge,

m is the mass of an electron,

c is the speed of light,

$\gamma$  is the magnetic moment of the neutron in nuclear magnetons,

$f_i$  is the form factor for the unpaired electrons on the  $i^{\text{th}}$  atom,

$\mathcal{H}_{i,X,r}$  is the component of the magnetic vector in the  $\mathbf{X}$  direction and localised on the  $i^{\text{th}}$  atom in the  $r^{\text{th}}$  equivalent position.

The above equations for the magnetic cross section can be applied to any magnetic structure with a unit cell defined by  $u\mathbf{a}$ ,  $v\mathbf{b}$ , and  $w\mathbf{c}$ , where  $u$ ,  $v$ , and  $w$  are integers and  $\mathbf{a}$ ,  $\mathbf{b}$ , and  $\mathbf{c}$  are the original nuclear unit cell vectors (*i.e.* when the magnetic unit cell is equal to, or a multiple of, the nuclear cell).

#### A.4.2. PRINCIPLE OF FITTING DIFFRACTION PATTERN

Now, let us return back to eq.(A.25), which describe the peak shape of constant wavelength powder diffraction, and write it in a simpler form,

$$y_i = \omega_{i,k} S_k^2 \quad (\text{For single peak}) \quad (\text{A.35})$$

where,

$$\omega_{i,k} = t_{j_k} L_k \frac{2\sqrt{\ln 2}}{H_k \sqrt{\pi}} \exp\left[-b_k (2\theta_i - 2\theta_k)^2\right] \cdot \left\{1 - P(2\theta_i - 2\theta_k)^2 \cdot \frac{s}{\tan \theta_k}\right\} \quad (\text{A.36})$$

$\omega_{i,k}$  is a measure of the contribution of the Bragg peak at position  $2\theta_k$  to the diffraction profile  $y_i$  at position  $2\theta_i$ .

In the case of overlapping Bragg peaks (where more than one Bragg peak contributes to the profile intensity,  $y_i$ , at position  $2\theta_i$ ) the resultant diffraction peak can be written as,

$$y_i = \sum_k \omega_{i,k} S_k^2 \quad (\text{For overlapping peaks}) \quad (\text{A.37})$$

Generally, in any peak deconvolution routine there are three main steps to follow, which would apply on the process of segregation the diffraction pattern into its component peaks as follows [47],

1. Subtraction of the background signal from the diffraction pattern either by fitting a polynomial to the minimal points on the curve, or by taking a second read-out without the presence of the crystalline sample.
2. Identification of the positions of the component peaks from local maxima, minima, and the deflection points on the whole diffraction pattern. First, the data points in the whole diffraction pattern are fitted with some function for example with a polynomial. Secondly, this function is derivated. The local maxima and minima of this derivative will correspond to the first and the second limits of the individual peaks, respectively. Finally, this derivative is derivated again and the minima of this second derivative will correspond to the positions of these peaks.

3. According to this initial estimation of the peaks positions, a refinement program will try to fit the diffraction pattern with peaks of a previously specified shape (in this case the modified Gaussian, eq. (A.37)).

The peak parameters could be determined from minimising an adopted Chi-squared merit function.

#### A.4.2.1. LEAST-SQUARES REFINEMENT

A Chi-squared merit function,  $M$ , should be adopted and minimised with respect to the parameters. This function is,

$$M = \sum_i W_i \left( S_{i,obs}^2 - \frac{1}{c} S_{i,calc}^2 \right)^2 \quad (\text{A.38})$$

for the refinement on separated integrated intensities;

$$M = \sum_i W_i \left( \sum_k S_{k,obs}^2 - \frac{1}{c} \sum_k S_{k,calc}^2 \right)^2 \quad (\text{A.39})$$

for the integrated intensities of groups of overlapping reflections; and

$$M = \sum_i W_i \left( y_{i,obs} - \frac{1}{c} y_{i,calc} \right)^2 \quad (\text{A.40})$$

for the profile refinement

$$M = \frac{1}{n - p + c} \cdot \sum_i W_i (y_{k,obs} - y_{k,calc})^2 = \frac{R_{\text{weighted profile}}}{R_{\text{expected profile}}} \quad (\text{A.41})$$

where,

$\sum_i$  is the sum over the independent observations,

$\sum_k$  is the sum over the overlapping reflections in each group,

$n, p, c$  are the number of observations, variables, and constraints, respectively,

$W_i = \frac{1}{\sigma^2(Y_i) + \sigma^2(B_i)}$  is a statistical weight to be assigned to the corrected intensity  $y_i$ .

where,

$\sigma^2 = 0$  for  $B_i$  chosen to be zero, because  $B_i$  is determined graphically so its variance is not known.

$\sigma^2 = Y_i$  for  $Y_i$  from the counting statistics

Hence,  $W_i = \frac{1}{Y_i}$ .

Minimising  $M$  gives a number of equations. If each peak has  $n_p$  parameters and the background has  $n_B$  parameters, then the number of equations would be  $n_p$  times the number of peaks plus  $n_B$ . The resultant equations are non-linear functions to these parameters, therefore solving them analytically is impossible and the only way to solve them is to use numerical iterative methods. One can find in literature that there are various methods, such as the Levenberg-Marquars Method (LLM) and the Newton-Raphson Method (NRM) [48].

Rietveld refinement computer program should be based upon one or more of these numerical iterative methods, "A computer program carries out the least-square refinement in the usual manner."[46].

Initial approximate values for all parameters should be given to the program in its first cycle, this is because the problem is not linear in these parameters as we mentioned above. The program tries to find the best possible fit to the diffraction pattern by refining these parameters in the subsequent cycles until a determined convergence criterion is reached. It is possible to keep any parameter constant during the refinement or to introduce linear or quadratic constraints between any number of them.

To know how good the fit is, some measure of the "goodness of the fit" is needed.

There are two kinds of measures,

- 1) **Qualitative**, where a visual comparison between the observed and the calculated pattern is carried out, and this is, in fact, the most reliable method, and enhanced by plotting the difference between the two.
- 2) **Quantitative**, the quantities that measure the goodness of the fit are called R factors. Let us define an approximation of the observed integrated intensities by separating the peaks according to the calculated values of the integrated intensities, *i.e.*,

$$I_{k,obs} = \sum_j \omega_{j,k} \cdot S_{k,cal}^2 \cdot \frac{y_{i,obs}}{y_{i,cal}} \quad (\text{A.42})$$

This equation is often called peak separation method.

where,

$\sum_j$  is the sum over all  $y_{i,obs}$  which can theoretically contribute to the

integrated intensity  $I_{k,obs}$ .

From the values of  $I_{k,obs}$ , we can obtain the values of  $F_{k,obs}^2$ ,  $J_{k,obs}^2$  and  $S_{k,obs}^2$ , and

define the following R values,

$$R_{nuclear} = 100 \cdot \frac{\sum_i \left| F_{i,obs}^2 - \frac{1}{c} F_{i,calc}^2 \right|}{\sum_i F_{i,obs}^2} \quad (\text{A.43})$$

$$R_{magnetic} = 100 \cdot \frac{\sum_i \left| J_{i,obs}^2 - \frac{1}{c} J_{i,calc}^2 \right|}{\sum_i J_{i,obs}^2} \quad (\text{A.44})$$

$$R_{total} = 100 \cdot \frac{\sum_i \left| S_{i,obs}^2 - \frac{1}{c} S_{i,calc}^2 \right|}{\sum_i S_{i,obs}^2} \quad (\text{A.45})$$

$$R_{\text{profile}} = 100 \cdot \frac{\sum_i \left| y_{i,\text{obs}}^2 - \frac{1}{C} y_{i,\text{calc}}^2 \right|}{\sum_i y_{i,\text{obs}}^2} \quad (\text{A.46})$$

$$R_{\text{weighted profile}} = 100 \cdot \left[ \frac{\sum_i W_i \cdot \left| y_{i,\text{obs}} - y_{i,\text{calc}} \right|^2}{\sum_i W_i \cdot y_{i,\text{obs}}^2} \right]^{1/2} \quad (\text{A.47})$$

$$R_{\text{expected profile}} = 100 \cdot \left[ \frac{n - p + c}{\sum_i W_i \cdot y_{i,\text{obs}}^2} \right]^{1/2} \quad (\text{A.48})$$

$$R_{\text{integrated intensities}} = 100 \cdot \frac{\sum_i \left| I_{k,\text{obs}} - I_{k,\text{calc}} \right|}{\sum_i I_{k,\text{obs}}} \quad (\text{A.49})$$

#### A.4.2.2. LEAST-SQUARES PARAMETERS

To sum up, the least square parameters can be classified into two categories,

1. The first category, the profile parameters
  - a) The positions of the Bragg peaks,
  - b) The half-widths of the Bragg peaks,
  - c) The possible asymmetry of the diffraction peaks, and
  - d) The property of the powder sample (i.e. preferred orientation).

These parameters are,

- |                     |   |
|---------------------|---|
| U, V, W             | are half-width parameters as defined in eq. (A.24),                       |
| Z                   | is the electronic detector delay zero point correction in $\mu\text{s}$ . |
| P                   | is asymmetry parameter as defined in eq. (A.25),                          |
| G                   | is preferred orientation parameter as defined in eqs. (A.26 and A.27),    |
| A, B, C, D, E, E, F | are cell parameters according to the equation,                            |

$$\frac{1}{d^2} = Ah^2 + Bk^2 + Cl^2 + Dkl + Ehl + Fhk \quad (\text{A.50})$$

One should note that these quantities are not the cell parameters ( $a, b, c, \alpha, \beta, \gamma$ ) themselves but are quantities related to their reciprocal space as detailed below.

$$\left. \begin{array}{ll} A = a^*; & D = 2b^*c^*\cos\alpha; \\ B = b^*; & E = 2c^*a^*\cos\beta; \\ C = c^*; & D = 2a^*b^*\cos\gamma. \end{array} \right\} \quad (\text{A.51})$$

2. The second category is the structure parameters, which define the contents of the asymmetric unit cell.

$c$  is the overall scale factor such that  $y_{\text{cal}} = c \cdot y_{\text{obs}}$ ,

$Q$  is the overall isotropic temperature parameter as defined in eqs. (A.18, A.19 and A.27),

$x_i, y_i, z_i$  are fractional co-ordinates of the  $i^{\text{th}}$  atom in the asymmetric unit as defined in eq. (A.15),

$B_i$  is the atomic isotropic temperature parameter as defined in eqs. (A.29 and A30),

$n_i$  is the occupation number as defined in section (e (i)),

$\mathcal{H}_{x,i}, \mathcal{H}_{y,i}, \mathcal{H}_{z,i}$  are components of the magnetic vector of the  $i^{\text{th}}$  atom in the asymmetric unit as defined in eq. (A.33 and A.34).

The contents of the complete unit cell is described when the contents of the asymmetric unit cell are given in addition to the set of symmetry operations which generate the remaining positions and the magnetic vectors in the cell. The symmetry operations on the nuclear positions consist of a rotation and a translation, *i.e.*,

$$\begin{pmatrix} x_{i,r} \\ y_{i,r} \\ z_{i,r} \end{pmatrix} = \mathbf{R}_r \begin{pmatrix} x_i \\ y_i \\ z_i \end{pmatrix} + \vec{T}_r \quad (\text{A.52})$$

where,  $\mathbf{R}_r$  and  $\vec{T}_r$  are respectively a  $3 \times 3$  rotation matrix and a  $1 \times 3$  translation vector describing the  $i^{\text{th}}$  equivalent position.

The magnetic vector can undergo a rotation only, *i.e.*,

$$\begin{pmatrix} \mathcal{H}_{x,i,r} \\ \mathcal{H}_{y,i,r} \\ \mathcal{H}_{z,i,r} \end{pmatrix} = \mathbf{M}_{i,r} \begin{pmatrix} \mathcal{H}_{x,i} \\ \mathcal{H}_{y,i} \\ \mathcal{H}_{z,i} \end{pmatrix} \quad (\text{A.53})$$

where,  $\mathbf{M}_{i,r}$  is a  $3 \times 3$  rotation matrix which describes the rotation of the magnetic vector of the  $i^{\text{th}}$  atom on going from the asymmetric unit to the  $i^{\text{th}}$  equivalent position. The subscript  $i$ , on this matrix, implies that when magnetic vectors are transferred to the  $i^{\text{th}}$  equivalent position in the asymmetric unit, they are not necessarily subjected to the same rotation. Therefore, there could be a different sets of rotation matrices for each individual magnetic atom sitting in the asymmetric unit.

### A.4.3. RIETVELD METHOD FOR TIME OF FLIGHT

#### NEUTRON POWDER DIFFRACTION [28]

All the above description was for the constant wavelength Rietveld method where Gaussian peak shape was adopted. However, for the time of flight, t-o-f, neutron powder diffraction, the same principles are applied. The details of the calculation of the peak shape,  $y_{i,\text{cal}}$  will be different than above where certain terms need to be modified. These modifications mainly are,

1. Introduction of the absorption corrections, where they are wavelength dependent.

This was neglected for the constant wavelength diffraction,

2. Introduction of extinction corrections for the same reason as in (1), and finally,
3. Introduction of a more complex peak shape.

The peak shape in t-o-f powder diffraction is very complicated. This is because of inclusion of many complicated physical factors, which are,

1. Pulse shape,
2. Moderator physics,
3. Instrumental resolution, and
4. Sample effect.

If we neglect factor (4), we can get a reasonable approximation of the peak shape, as shown below,

$$P(t) = \frac{t^2}{2\tau_f^3} \exp\left(\frac{-t}{\tau_f}\right) * \left[ (1-R) \cdot \delta(t) + R \left( \frac{1}{\tau_s} \right) \exp\left(\frac{-t}{\tau_s}\right) \right] * \frac{1}{\sigma\sqrt{2\pi}} \exp\left(\frac{-x^2}{2\sigma^2}\right) \quad (\text{A.54})$$

where,

$t$  is the time of flight,

$\tau_f$  is the fast exponential decay constant for epithermal neutrons,

$\tau_s$  is the slow exponential decay constant for thermal neutrons,

$R$  is the so-called switch function (switching between epithermal and thermal neutrons contributions to the peak shape), and related to a Boltzmann function,  $\exp\left(-\frac{E}{E_0}\right)$ . This factor,  $R$ , represents the fractional contribution of  $\tau_s$ , and  $(1-R)$  represents the fractional contribution of  $\tau_f$

$\sigma$  is a Gaussian width parameter,

$*$  is the convolution operator, where the convolution function,  $c(\mathbf{u})$ , of two functions,  $f(\mathbf{r})$  and  $g(\mathbf{r})$ , is a third function defined as,

$$c(\mathbf{u}) = f(\mathbf{r}) * g(\mathbf{r}) = \int_{\mathbf{r}} f(\mathbf{r}) \cdot g(\mathbf{u} - \mathbf{r}) \cdot d\mathbf{r}$$

As we see from eq. (A.54), the peak shape has been defined as a convolution of three functions, where the first two are related to the moderator physics (fast and slow decays, and the switch function), while the final function is a Gaussian which represents the contribution to the overall instrumental resolution and describes (the beam divergence, the sample size, and other effects).

These peak shape factors can be determined and refined by refinement programs and there are many of them such as,

1. GDELSQ (Gaussian Double Exponential Least Squares), which has a peak shape obtained by convoluting a Gaussian with two decaying exponential functions representing the fast and the slow contributions of the moderator.
2. VDELSQ (Voigt Double Exponential Least Squares), which is the same as above added to it a Lorentzian component, and
3. VICLSQ (Voigt-Ikeda- Carpenter Least Squares), where the convolution of a double decaying exponential, Gaussian, and Lorentzian functions, is incorporated into the program.

I shall only list how the peak shape factors are parameterised in the latter,

- |                            |  |                |
|----------------------------|--|----------------|
| 1. Switch (R)              | $a_R / \left[ \exp\left(\frac{\lambda}{b_R}\right) + \exp\left(\frac{c_R^2}{\lambda^2}\right) \right]$ | (3 parameters) |
| 2. Fast decay ( $\tau_f$ ) | $a_f + b_f \lambda + c_f \lambda^2$  | (3 parameters) |
| 3. Slow decay ( $\tau_s$ ) | $(a_s + b_s \lambda) \operatorname{erfc}(d_s (c_s - \lambda))$   | (4 parameters) |
| 4. Gaussian ( $\sigma$ )   | $(a_\sigma + b_\sigma \lambda^2 + c_\sigma \lambda^4)^{1/2}$   | (3 parameters) |
| 5. Lorentzian ( $\gamma$ ) | $a_\gamma + b_\gamma \lambda + c_\gamma \lambda^2$   | (3 parameters) |

We can see that there are sixteen parameters involved in this program and in principle all can be refined. In practice, only a limited number of these parameters are allowed to vary and the rest is fixed at values depending on the neutron source and instrument characteristics. An explanation of these 16 peak shape parameters and how they are varied in a refinement program are given below:

1. Switch (R): The switch function represents the moderator contribution to the peak shape and is derived semi-empirically from refinement of data from an MgO sample. It links the fast exponential decay effect (on epithermal neutrons) and the slow exponential decay effect (on thermal or Maxwellian neutrons) imposed by the moderator upon the peak shape. The term  $\exp(\lambda/b_R)$  represents the absorption in the moderator and is obviously dominating at short wavelengths. The term  $\exp(-c_R^2/\lambda)$  is the Boltzmann fraction and contributes most at long wavelengths to the peak shape. The switch parameters,  $a_R$ ,  $b_R$  and  $c_R$ , are empirically determined and never allowed to vary in the refinement process.
2. Fast decay ( $\tau_f$ ): As we mentioned above the moderator effect on epithermal neutrons which escape the slowing-down process is to impose a fast exponential decay upon the peak shape which is characterised by the constant  $\tau_f$ . However,  $\tau_f$  varies with the wavelength. In practice, it varies only as a function of  $\lambda$ , therefore in a refinement process,  $a_f$  is fixed at an empirically determined value,  $c_f$  is fixed to zero value, and the most important term  $b_f$  can only be varied with great caution when the accuracy of the refinement is guaranteed.
3. Slow decay ( $\tau_s$ ): As for epithermal neutrons, the moderator imposes a slow exponential decay upon the peak shape with a constant  $\tau_s$  for thermal neutrons. However, the behaviour of this constant with wavelength is rather complicated in the switching region between the epithermal and thermal neutrons and is

independent of  $\lambda$  at long wavelengths. The error function,  $\text{erfc}(d_s(c_s-\lambda))$ , is derived empirically from refinement of data of MgO sample, and represents well the switching behaviour. All the parameters  $a_s$ ,  $b_s$ ,  $c_s$  and  $d_s$  are found empirically. In a refinement process, the last two parameters are fixed and set to zero values for POLARIS data. Whereas the first two parameters,  $a_s$  and  $b_s$ , can be varied only in the case of very accurate refinements with an extreme caution. The parameter  $a_s$  is the most important one and represent well the magnitude of  $\tau_s$  at long times.

4. Gaussian ( $\sigma$ ): The three parameters,  $a_\sigma$ ,  $b_\sigma$  and  $c_\sigma$ , describe the Gaussian component of the Voigt function (convolution of Gaussian and Lorentzian) and are measured in microseconds. The first parameter  $a_\sigma$  is due to the finite width of the neutron pulse, ( $\sim 0.4 \mu\text{s}$ ) for the beam produced at ISIS, and to paracrystallinity in the sample. It is independent of the wavelength and usually has a negligible value and fixed to zero value in the refinement of POLARIS data. The  $b_\sigma\lambda$  term is the most significant term. It includes the broadening effect of sample strains in addition to a small contribution from the angular instrumental resolution  $\Delta\theta\cot\theta$ . Therefore, the parameter  $b_\sigma$  is one of the most valid parameters to vary in a refinement. The  $b_\sigma\lambda^2$  term is due to particle size and stacking faults broadening effects and it has a very small contribution to  $\sigma$ . Therefore, varying  $b_\sigma$  parameter is usually left to the last stage in a refinement to make the final fitting adjustments because of its small contribution.
5. Gamma ( $\gamma$ ): The three parameters,  $a_\gamma$ ,  $b_\gamma$  and  $c_\gamma$ , as for  $\sigma$ , describe the Lorentzian component of the Voigt function and are also measured in microsecond. The first parameter  $a_\sigma$  is  $\lambda$  independent and is due to paracrystallinity in the sample but with no neutron pulse broadening. It is has usually a negligible value and also fixed to zero value in the refinement of POLARIS data. The  $b_\gamma\lambda$  term includes the

broadening effect arising from strains in the sample and from angular instrumental resolution  $\Delta\theta\cot\theta$  but this time with minor contribution. Therefore, refining  $b_\gamma$  comes last in the refinement process. The most dominant term in the Lorentzian function is  $c_\gamma\lambda^2$  arising from particle size and stacking faults. Therefore,  $c_\gamma$  is another most valid to vary.

## **A.5. THERMAL ANALYSIS (Calorimetry) [9, 10, and 11]**

Caloric measurements have been around since the middle of the 18<sup>th</sup> century. The aim of calorimetry is to measure heat, and this means to exchange heat, which usually demonstrate itself as a change in the temperature of the body under the observation. The differences of local temperatures along the path can show the flowing heat rate. Chemical and many physical transitions are associated with the production or consumption of heat. Investigation of such processes can be carried out universally by calorimetric methods, where the amount of heat input or output from a sample can be measured exactly.

There is a huge diversity of calorimeters used to measure heats and heat capacities in different areas of application. In the following I shall only describe the calorimeter I used, the heat compensating calorimeter, or more specifically, the power compensation differential scanning calorimeter (the Perkin-Elmer calorimeter DSC7)

## A.5.1 THE DIFFERENTIAL SCANNING CALORIMETER

### DSC7

Differential scanning calorimetry (DSC) is a technique of non-equilibrium calorimetry in which the heat flow into or from a sample and a reference is measured as some function of time or temperature. In differential thermal analysis (DTA), the temperature difference between a sample and reference is measured as some function of time or temperature. In DSC, the heat flow is measured by keeping the sample and reference thermally balanced by changing a current passing through the heater under the two chambers.

In my measurements, I used a Perkin-Elmer DSC7 calorimeter; a schematic representation of it is shown in figure A.6. It consists of two identical micro-furnaces; each of them has a temperature sensor and a heating resistor. The two micro-furnaces de-coupled thermally by being separated from each other. They are both placed inside an aluminium block, which is kept at a constant temperature by means of a nitrogen gas draught of a pre-set temperature of 0 C°. One of the micro-furnaces contains the sample and the other one contains the reference sample, which is usually an empty capsule of aluminium. The measurement signal is the temperature difference between the two systems. Each of the two micro-furnaces is heated separately so that they conform to a given temperature-time program. When the two micro-furnaces are at the same temperature, the same heating power is supplied to each of them via a control circuit (see figure A.7). However when extra heat is released or consumed during sample transition (exothermic or endothermic process) the sample heating power is regulated via a proportional controller so that the electric heat supplied is decreased or

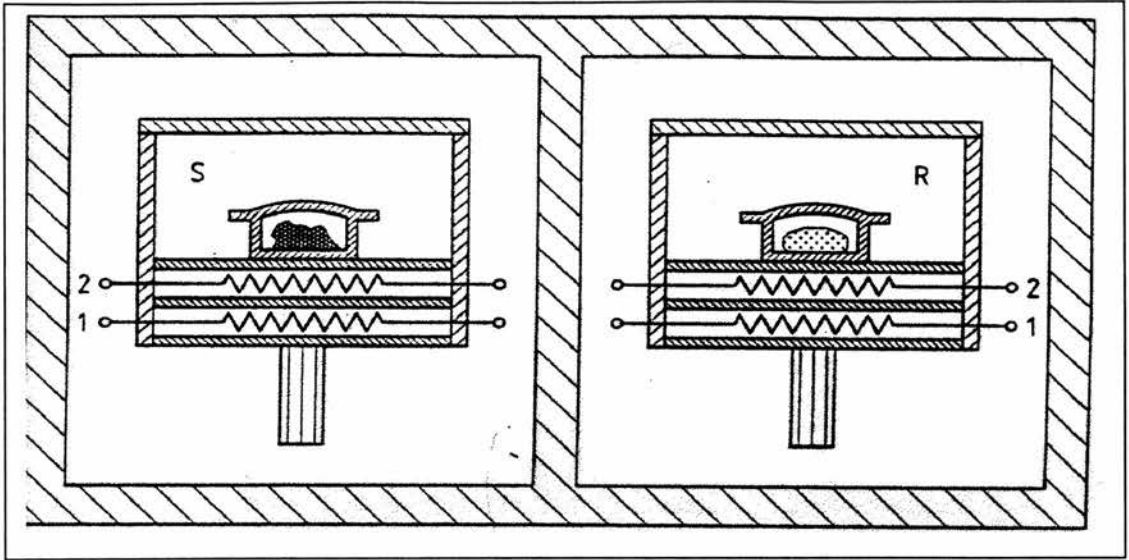


Figure A.6 Power compensation DSC (Perkin-Elmer Corp.). Set-up of the measuring system. S sample measuring system with sample crucible, micro-furnace and lid, R reference sample system (analogous to S), 1 heating wire, 2 resistance thermometer. Both measuring systems separated from each other-are positioned in a surrounding (block) at constant temperature [9].

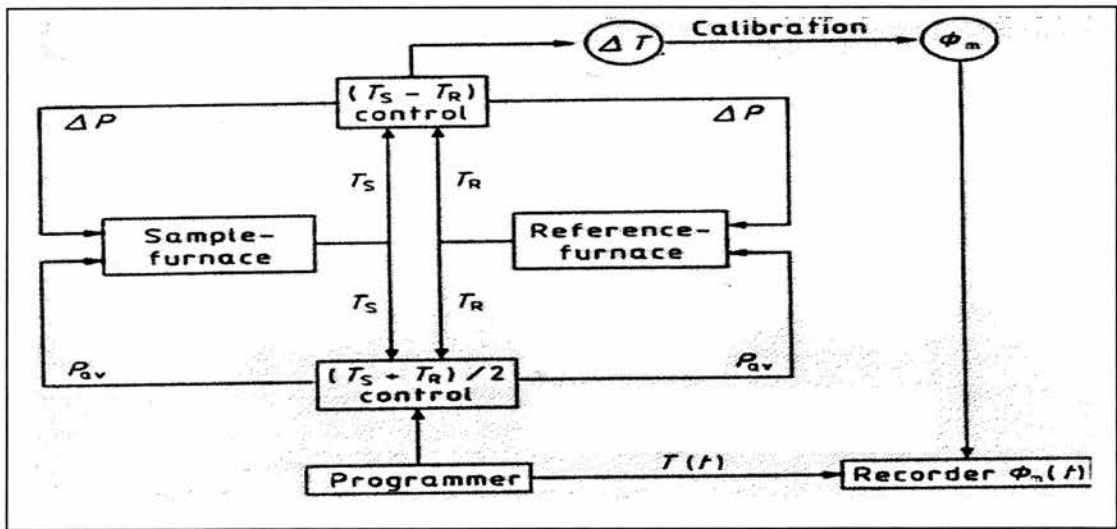


Figure A.7 Power compensation DSC (Perkin-Elmer Corp.). Block diagram showing the function principle.  $T_s$  temperature of the sample furnace,  $T_R$  temperature of the reference sample furnace,  $\Delta T = T_s - T_R$ ,  $P_{av}$  average heating power,  $\Delta P$  compensation heating power,  $\phi_m$  measured heat flow rate (measurement signal) [9].

increased by just the amount as has been generated or consumed during the transition process. The heating power  $\Delta P$  is proportional to the temperature difference  $\Delta T$ , which is the measured signal *i.e.*,

$$\Delta P = -K_1 \Delta T \quad (\text{A.53})$$

where,  $K_1$ , is a factory-set fixed quantity of the proportional controller.

A heat flow rate  $\phi_m$  is assigned to the measurement signal  $\Delta T$  as a result of a factory-installed calibration.

$$\phi_m = -K_2 \Delta T \quad (\text{A.54})$$

where,  $K_2$ , is a definite quantity adjusted via software (calibration).

The output signal  $\phi_m$  (in mW) is plotted against the scanning temperature,  $T$ . The resultant curve is called heat flow curve, and a schematic representation of it is shown in figure A.8.

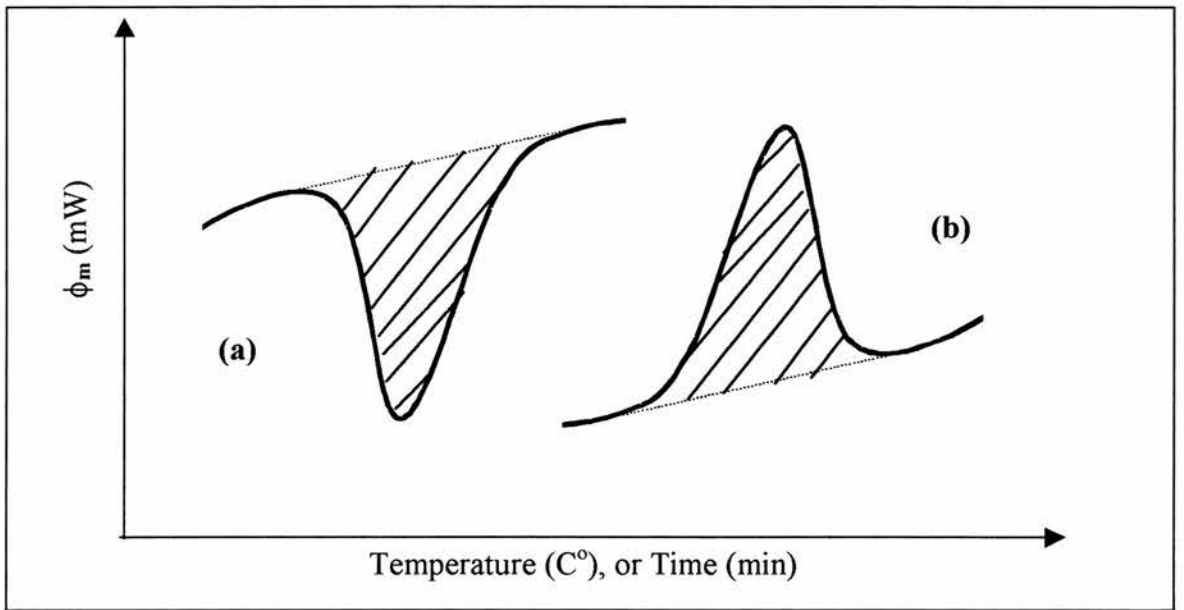


Figure A.8 Schematic representation of measured heat flow rate,  $\phi_m$ , of Perkin-Elmer DSC7. Curve(a) is an exothermic , where sample generates heat. Curve (b) is an endothermic where sample consumes heat.

## REFERENCES

- [1] D. Gignoux and D.Schmitt, *Journal of Magnetism and Magnetic Materials*, **100**, 99-125, (1991).
- [2] T. Egami, *Rep. Prog. Phys.*, **47**, 1601-1725, (1984).
- [3] *Engineering Materials 2: an introduction to microstructures, processing and design*, M. Ashby and D.R. Jones, Oxford : Pergamon, (1986).
- [4] S.H. Kilcoyne and P. Manuel: Novel routes to new metallic compounds, *ILL ANNUAL REPORT 98*, 42-43.
- [5] S.H. Kilcoyne and P. Manuel, (private communication).
- [6] S. Hull, R.I Smith, W.I.F David, A.C. Hannon, J. Mayers and R. Cywinski, *The POLARIS Powder Diffractometer at ISIS*, *Physica B* **180 & 181**, 1000-1002, (1992).
- [7] *ISIS 98*, The Rutherford Appleton Laboratory, *ISIS Facility Annual Report*, RAL-TR-1988-050,(1997-98).
- [8] *Profile Analysis of Neutron Powder Diffraction Data*, Rutherford Appleton Laboratory Report RAL-92-032, Version 2, (1993).
- [9] *Differential scanning calorimetry: an introduction for practitioners*; G.W.H. Höhne, W. Hemminger, H.-J. Flammersheim, Berlin New York : Springer-Verlag, (1996).
- [10] *Thermal characterization techniques*, Philip E. Slade, Jr., and Lloyd T. Jenkins, New York : M. Dekker, (1970).
- [11] *Differential thermal analysis, Vol.1 Fundamental aspects*, R.C. Mackenzie, London : Academic P, (1970).

- [12] Z. Altounian, Tu. Cuo-hua, and J. G. Strom-Olsen, *J. Appl. Physics* **54** (6), 3111-3116, (1983).
- [13] *Metals reference book*, 5th ed., Colin J. Smithells, and Eric A. Brandes, London : Butterworth, (1976).
- [14] G. Ghosh, *J. Mater. Res.*, **9**, (3), 598-616, (1994).
- [15] E.T. Hayes, A.H. Roberson, and O.G. Paassche, *Trans. ASM*, **45**, 893-900, (1953).
- [16] M.E. Kirkpatrick, D.M. Bailey and J.F. Smith, *Acta. Cryst.*, **15**, 252-255, (1962).
- [17] Z. Altounian and J.O. Ström-Olsen, *J. Appl. Phys.*, **55**, (6), 1566-1571, (1984).
- [18] Y.C. Feng, K.H. Kuo, Z.K. Hei and Y.K. Wu, *Philosophical magazine A*, **56**, (6), 757-766, (1987).
- [19] M. Sutton, X.S. Yang and J. Mainville, J.L. Jordan-Sweet, K.F. Ludwig, Jr., and G.B. Stephenson, *Physical Review Letters*, **62**, (3), 288-291, (1989).
- [20] S. Brauer, J.O. Ström-Olsen, M. Sutton, Y.S. Yang, A. Zaluska, G.B. Stephenson and U. Kösters, *Physical Review B*, **45**, (14), 7704-7715, (1992-II).
- [21] V. Erukhimovitch and J. Baram, *Physical Review B*, **50**, (9), 5854-5856, (1994-I).
- [22] K. Lu, X.D. Liu and F.H. Huan, *Physica B*, **217**, 153-159. (1996).
- [23] (*We wish to acknowledge the use of the EPSRC's Chemical Database Service at Daresbury*). The United Kingdom Chemical Database Service, D.A. Fletcher, R.F. McMeeking, and D. Parkin, *J.Chem. Inf. Coput. Sci.*, **36**, 746-749, (1996).
- [24] P. Manuel and S.H. Kilcoyne, A Small Angle Neutron Diffraction study of the crystallisation of amorphous Ye-Fe, ISIS Facility Annual Report, RB9002, (1998).
- [25] GENIE program (Version 2.5 (7-DECGKS), Neutron Division RAL).

- [26] Crystallographica program v1.5, (c) Oxford Cryosystems, 1995-98.
- [27] R. Visnov, F. Ducastelle and G. Tréglia, *J. Phys. F: Met. Phys.*, **12**, 441-447, (1982).
- [28] The High Resolution Neutron Powder Diffractometer (HRPD) at ISIS- an Introductory User Guide, W.I.F. David, D.E. Akporiaye, R.M. Ibberson, and C.C. Wilson, version 1.0, (1988).
- [29] R. Peschar, H. Schnek and P. Čápková, *J. Appl. Cryst.*, **28**, 127-140, (1995).
- [30] A. Altomare, M.C. Burla, G. Cascarano, C. Guagliardi, A.G.G. Moliterni and G. Polidori, *J. Appl. Cryst.*, **29**, 341-345, (1996).
- [31] M. Tenhover, *J. Phys. F: Metal Phys.*, **11**, 2697-706, (1981).
- [32] L. Karlsson, A. Wannberg, R. L. McGreevy, and D. A. Keen., *Phys. Rev. B.*, **61**, (1), 487-491, (2000-I).
- [33] D. A. Keen and R. L. McGreevy, *J. Phys.: Condens. Matter*, **3**, 7383-7394, (1991).
- [34] K. Nassau, L.V. Cherry and W.E. Wallace, *J. Phys. Chem. Solids*. **16**, 123, (1960).
- [35] P. Manuel, S.H. Kilcoyne, and R. I. Bewley, A neutron diffraction study of the re-crystallisation of  $\alpha$ -RE-Fe ribbons, ISIS Facility Annual Report, RB9003, (1997-98).
- [36] S.S. Deodhar and P.J. Ficalora, *Met. Trans. A*, **6A**, 647, (1975).
- [37] H. Eda, and Y. Yamamoto, *International Journal of The Japan Society For Precision Engineering*, , **31**, (2), 83-86, (1997).
- [38] Neutron beams: their use and potential in scientific research, S. Biggin, SERC, (1986).

- [39] PH4007, Structures and Dynamics of Solids, Prof. R. Cywinski, (lecture notes), (1999).
- [40] G.A. Batholomew and P.R. Tunicliffe, Report AECL-2600 Atomic Energy of Canada Limited, (1966).
- [41] User Guide for the Polaris Powder Diffractometer at ISIS, R.I. Smith and S. Hull Rutherford Appleton Laboratory Report, RAL-TR-97-038, (1997).
- [42] Solid State Physics I (JH), Prof. A. Miller, (lecture notes), (1999).
- [43] Neutrons and solid state physics, L. Dobrzynski and K. Blinowski, New York : Ellis Horwood, (1994).
- [44] International Tables of Crystallography.
- [45] H.M. Rietveld, Acta. Cryst. **20**, 508, (1966).
- [46] H.M. Rietveld, J. Appl. Cryst. **2**, 65-71, (1969).
- [47] GCANEW Operating Manual, J.M. Gómez-Ros and A. Delyadu.
- [48] Numerical methods with MATLAB : a resource for scientists and engineers, G.J. Borse, Boston : PWS Publishing, (1997).